Nonequilibrium ultrafast excited state dynamics in DNA

Dissertation zur Erlangung

des Doktorgrades

an der Fakultät für Mathematik,

Informatik und Naturwissenschaften

Fachbereich Physik

der Universität Hamburg

vorgelegt von Martina Pola

Hamburg, 2016

Tag der Disputation: 23.09.2016

Gutachter der Dissertation:

Prof. Dr. Michael Thorwart

Prof. Dr. Arwen Pearson

Mitglieder der Prüfungskommission:

Prof. Dr. Daniela Pfannkuche

Prof. Dr. Michael Thorwart

Prof. Dr. Arwen Pearson

Prof. Dr. Carmen Herrmann

Prof. Dr. Frank Lechermann

List of publications

Data presented in this work has been partially used for the following publications:

1. M. Pola, M. Kochman, A. Picchiotti, V. Prokhorenko, R. J. D. Miller, M. Thorwart *"Linear photoabsorption spectra and vertical excitation energies of microsolvated DNA nucleobases in aqueous solution"*, submitted to *The Journal of Chemical Physics.*

2. V. Prokhorenko, A. Picchiotti, M. Pola, A. Dijkstra, R. J. D. Miller, *"New Insights into the Photophysics of DNA Nucleobases"*, submitted to *The Journal of Physical Chemistry Letters.*

3. M. Kochman, M. Pola, R. J. D. Miller, *"Theoretical Study of the Photophysics of 8-Vinylguanine, an Isomorphic Fluorescent Analogue of Guanine"*, *The Journal of Physical Chemistry A*, 2016, 120 (31), 6200–6215.

4. M. Pola, J. Stockhofe, P. G. Kevrekidis, P. Schmelcher *"Vortex-Bright Soliton Dipoles: Bifurcations, Symmetry Breaking and Soliton Tunneling in a Vortex-Induced Double Well"*, *Physical Review A*, 2012, 86, 053601.

Contents

2

Abstract

The results of simulations for linear and two-dimensional electronic spectroscopy of DNA nucleobases have been presented in this work.

How nucleic acids respond to radiation is relevant to human health because UV radiation can be the starting point of damaging photochemical reactions leading to permanent damage of DNA. Moreover it is also important for our understanding of how life on earth developed.

According to the popular reductionist approach, the study of deexcitation processes of DNA double strands should start with the investigation of nucleobases, the main chromophores in DNA. The possible photochemical paths following UV excitation in DNA monomers are in general prevented by ultrafast decay processes, through which the deexcitation of photoreactive states is allowed to take place. Ultrafast internal conversion is responsible for this relaxation process, which can be investigated by identifying the conical intersections (CIs) between ground and excited states involved in the radiationless decay.

As a first step in the understanding of such nonradiative processes, excited state properties and linear absorption spectra have been simulated for the four DNA nucleobases in their microsolvated structures, by combining time-dependent density functional theory calculations and the semiclassical nuclear ensemble method. This approach includes explicitly vibrational broadening, which seems essential for a reliable comparison of simulated photoabsorption spectra with experimental data.

The second part of the project was devoted to the determination of optical properties of the DNA nucleobase isomer 9H-adenine in terms of the third-order response function, with a direct connection of the theoretical model-

ings to experimental results of 4-wave-mixing time-resolved optical spectro-scopies, in particular to 2D-UV Fourier and pump probe spectroscopy.

A minimal kinetic model derived from experimental results was proposed to underline the decay behaviour observed in adenine, where after excitation to the bright $\pi\pi^*$ state, the deexcitation can be direct to the ground state or via a dark $n\pi^*$ state. Two excited state absorptions from the $\pi\pi^*$ and $n\pi^*$ are also proposed to take place. Time Nonlocal, and Hierarchy Equations of Motion approachs have been used to simulate the Non-Markovian quantum dynamics of 9H-adenine. A good agreement between theoretical and experimental 2DES and pump probe spectra has been reached in terms of size and energy range characterizing the peaks forming the spectra.

The present study will serve as a basis for future simulations and experimental investigations, for instance further linear and 2D electronic spectrocopy simulations where different methods can be applied, or the extension of the model from single nucleobases to nucleotides (and nucleosides) polymers.

Zusammenfassung

In dieser Arbeit wurden die Ergebnisse von Simulationen der linearen und zweidimensionalen Elektronenspektroskopie von Nukleobasen der DNA vorgestellt.

Die Folgen der Bestrahlung von Nukleinsäuren ist wichtig für die menschliche Gesundheit, da UV-Strahlung die Schädigung photochemischer Reaktionen nach sich ziehen kann, was zur permanenten Beschädigung der DNA führt. Zudem ist es entscheidend für unser Verständnis der Entwicklung des Lebens auf der Erde.

Einem weit verbreiteten reduktionistischen Ansatz folgend sollte die Untersuchung der Abregung der DNA-Doppelstränge mit der Analyse der Nukleobasen beginnen, die die Hauptchromophore der DNA sind.

Das Auftreten möglicher photochemischer Pfade, die aus der Anregung von DNA-Monomeren mit UV-Strahlung resultieren, wird im Allgemeinen mithilfe ultraschneller Zerfallsprozesse verhindert, durch die die Abregung der photoreaktiven Zustände stattfinden kann. Die ultraschnelle interne Abregung ist für diesen Relaxationsprozess verantwortlich, welcher durch die Identifizierung der Kegelschnitte (conical intersections – CIs) zwischen den am strahlungslosen Zerfall beteiligten Grund- und angeregten Zuständen untersucht werden kann.

Als ersten Schritt für das Verständnis solcher strahlungsloser Prozesse wurden die Eigenschaften der angeregten Zustände und die linearen Absorptionsspektren der vier Nukleobasen der DNA in ihren mikrogelösten Strukturen simuliert, indem die Rechenmethoden der zeitabhängigen Dichtefunktionaltheorie mit der Nuclear-Ensemble-Methode kombiniert wurden. Dieser Ansatz beinhaltet explizit die durch Vibrationen verursachte Linienverbre-

iterung, welche essentiell für einen zuverlässigen Vergleich zwischen den simulierten Photoabsorptionsspektren und experimintellen Daten zu sein scheint.

Der zweite Teil des Projekts war der Bestimmung der optischen Eigenschaften des DNA-Nukleobasenisomers 9H-Adenin in Bezug auf die Response-Funktion dritter Ordnung gewidmet, mit einer direkten Verknüpfung zwischen den theoretischen Modellen und den experimentellen Ergebnissen der 4-wave mixing zeitaufgelösten optischen Spektroskopien, insbesondere der zweidimensionalen UV-Fourier- und der Pump-Probe-Spektroskopie.

Basierend auf den experimentellen Ergebnissen wurde ein minimales kinetisches Modell vorgeschlagen, welches das bei Adenin beobachtete Zerfallsverhalten unterstreicht, bei dem nach der Anregung auf den hellen $\pi\pi^*$-Zustand die Abregung direkt oder über den dunklen $\pi\pi^*$-Zustand auf den Grundzustand stattfinden kann. Weiterhin wird das Stattfinden zweier Absorptionen im Zusammenhang mit den angeregten $\pi\pi^*$- und $n\pi^*$-Zuständen untersucht. Die Ansätze der zeitlich nichtlokalen Gleichungen und der Hierarchiegleichungen wurden verwendet, um die Nicht-Markovsche Quantendynamik von 9H-Adenin zu simulieren. Es wurde eine gute Übereinstimmung zwischen den theoretischen und den experimentellen 2DES- und Pump-Probe-Spektren hinsichtlich der die Peaks des Spektrums charakterisierenden Größe und Energiebereichs erzielt.

Die vorliegende Untersuchung dient als Grundlage für zukünftige Simulationen and experimentelle Untersuchungen, zum Beispiel für weitere Simulationen der linearen und zweidimensionalen Elektronenspektroskopie, bei denen unterschiedliche Methoden angewandt werden können, oder für die Erweiterung des Modells von einzelnen Nukleobasen auf Nukleotid-(und Nukleosid-)Polymere.

Chapter 1

Introduction
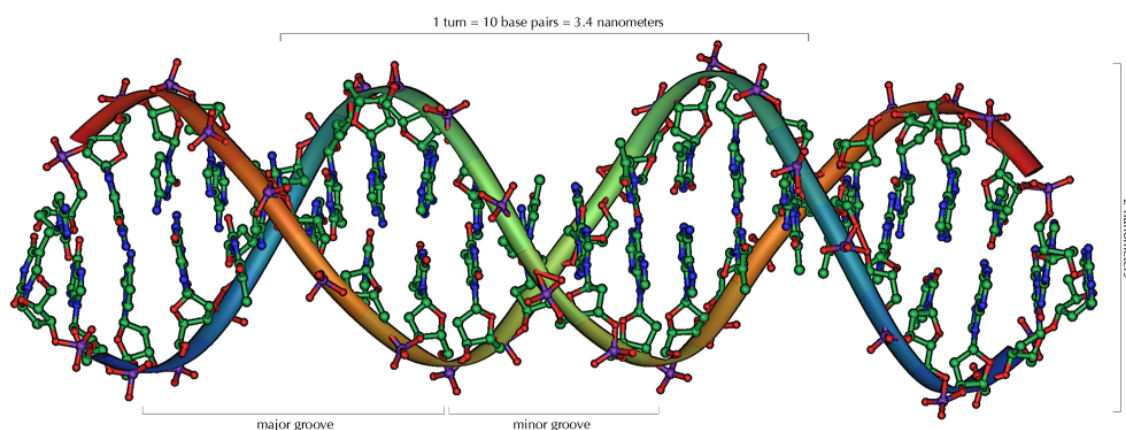
Figure 1.1: Double stranded DNA overview (picture taken from: Wikipedia, DNA, created by M. Ströck).

Solar light is well known to have a deep impact on the various physical and chemical reactions on the Earth, including biological processes, as, for instance, photosynthesis and vision. Moreover, UV irradiation can target biologically important molecules, such as proteins or enzymes, leading to dangerous photoreactions, which become particularly damaging in the case of nucleic acids, as these are the carriers of genetic information.

UV photochemistry of nucleic acids is thus of interest, as being the starting point of a sequence of events which produces at its end UV-induced dam-

age of DNA, with all its profound biological consequences (e.g. mutagenic and carcinogenic effects). Fortunately, DNA shows a high photostability, presumably due to some self-protection mechanisms that quickly convert dangerous electronic excitation into less dangerous vibrational energy that subsequently cools rapidly in solution.

To understand the details of this process, the most logical route, from the experimental and theoretical point of view, should start with the investigation of nucleobases, the principal chromophores in nucleic acids, and then continue by systematically considering the DNA sugar residues, pairing and stacking interactions, and so forth. Following this reductionist approach, the photophysical properties of nucleobases have been discussed in many contributions [1, 2, 3].

The five nucleobases occurring naturally in DNA and RNA strongly absorb UV radiation, although they are intrinsically very resistant to light-induced damage.

It is well established that ultrafast internal conversion is responsible for this relaxation process, occurring near the crossing of excited state and ground state potential energy surfaces (PESs) under conditions of strong nonadiabatic coupling [4, 5, 6]. Due to such a mechanism, nucleobases are photostable and protected by radiative damage.

The situation becomes much more complex when a nucleobase is interacting with other bases within the nucleic acid polymer [2, 7, 8]. The structure of nucleic acids allows for interactions between the same strands via stacking and, in case of double stranded DNA, also for interactions between two strands. In this case, even delocalized excitations can occur, leading to exciton and charge transfer phenomena during the relaxation pathway to the ground state of the polymer.

Linear absorption properties are a first step in the understanding of the UV photophysics of these systems, and the study of UV absorption of nucleobases plays a crucial role in clarifying how excited state relaxation is triggered depending on the excitation wavelength [9]. Nonlinear spectroscopy gives further information about electronic and vibronic couplings and the dynamics of chemical, semi-conductor, and biological samples, which are not accessible by applying linear spectroscopy studies [10]. Nucleobases exhibit

ultrafast radiationless decay and low emission quantum yields, which have been extensively investigated, but so far no definite agreement concerning the relaxation mechanism after excitation has been reached [11].

The present work deals with linear and 2D spectroscopy studies of single nucleobases. Linear absorption spectra have been calculated for the main tautomers of nucleobases in their microsolvated structures, by combining time-dependent density functional theory (TD DFT) calculations and the semiclassical nuclear ensemble method developed by Barbatti et al [9]. In addition, 2D and pump probe spectra have been calculated for 9H-adenine. For all the simulations, experimental data are available for a direct comparison with the calculated data.

1.1   Dynamics of UV-excited nucleobases

(a)   (b)
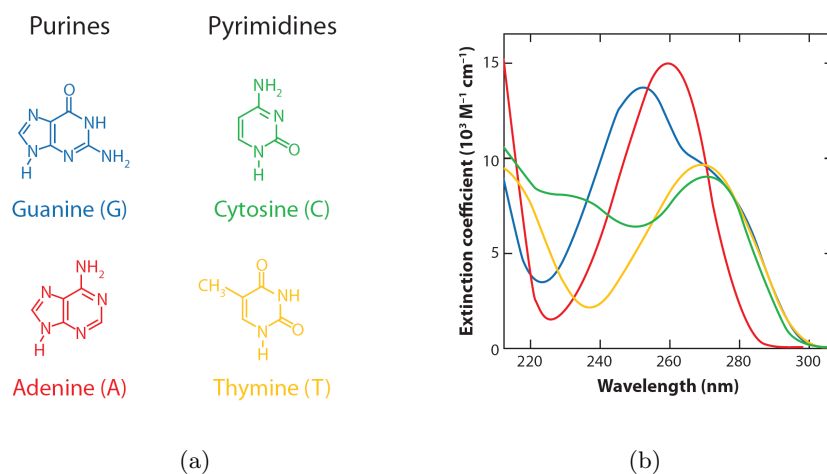
Figure 1.2: Chemical structures (a) and measured absorption spectra (b) of the four DNA nucleobases (picture taken from Ref.[2]).

Nucleobases are the main chromophores in DNA, strongly absorbing UV radiation, but showing at the same time a high degree of photostability. Photochemical events take place after a molecule absorbs a photon and reaches an excited electronic state, leading to inter- or intramolecular chemical reactions. The electronic energy can be radiated away by fluorescence, and this process usually occurs with a rate of the order of $\approx 10^9$ s^{-1}, which is

generally too slow to compete with an excited state reaction. Alternatively, the electronic energy is transferred into heat by internal conversion to the ground state, which is then dissipated to the environment. If the internal conversion is fast enough to prevent photochemical reactions from taking place, the molecule will have a short excited life time τ and will be stable against UV photodamage. This is why internal conversion provides a fundamental "self healing process" following the UV absorption of the molecule. The dissipation of the excess energy into internal energy of the ground state minimizes the probability of the occurrence of photochemical reactions.

The most relevant nucleobases show the shortest excited state lifetimes, while nucleobase derivatives, as isomers, have orders of magnitude longer lifetimes. These are related to a major propensity for photoreactions. A representative example is 5−methylcytosine, which shows a 10−fold longer lifetime than cytosine, and typically undergoes photodamage reactions.

Important information about the photostability of nucleobases has been obtained by ultrafast time-resolved spectroscopy, mostly concerning relaxation times, which are derived by fitting the measured deactivation curves in terms of the pump probe delay time [12, 13]. Within a few picoseconds these molecules return to the ground state, showing comparable deactivation times. This provides the possibility for the nucleobase to quickly transfer the harmful excess energy accumulated by photoabsorption of UV light into heat, which can then be dissipated to the environment. In spite of the similar time durations involved in the decay process, each of the five nucleobases follows different decay pathways, which can be investigated by performing theoretical calculations based on different approaches and approximations. A large amount of work has been carried out, reflecting the very rich and complex photophysics of nucleobases (NABs) [9, 11, 14].

Information about the relaxation processes has been provided by identifying the conical intersections (CIs) between ground and excited states where radiationless decay can take place, if optically created electronic energy is transferred to vibrational and/or rotational energies in S_0 through rapid internal conversion, which requires the crossing of potential energy surfaces.

Upon UV excitation, the four DNA nucleobases adenine, cytosine, guanine and thymine (A, C, G and T) show ultrafast relaxation from the lowest

bright $\pi\pi^*$ state to the ground state. However, the ultrafast relaxation is not due to a single deactivation mechanism for all nucleobases, although there are some general geometrical principles for the CIs connecting the excited states to the ground state, like strong puckering deformation of the six-membered rings [11, 15]. This six-sided structure is present in each DNA nucleobase, as is evident in Fig. 1.2(a).

Nevertheless, the details of the deactivation pathways are very sensitive to the form of the PESs, which can differ considerably, even between tautomers of the same molecule.

Generally, the dynamics of the purine bases A and G are less complex and faster than the dynamics encountered in the pyrimidine bases C and T. Purines and pyrimidines show substantially different decay pathways: the purine bases adenine and guanine mostly follow homogeneous pathways based on relaxation along the $\pi\pi^*$ states, while pyrimidines show possible bifurcations to $n\pi^*$ states and intersystem crossings to triplet states [2]. For these two molecules (single cytosine and thymine in solution), it was shown that the excited-state population bifurcates in the bright $^1\pi\pi^*$ state, with 60% returning to the ground state and 40% first passing through a $^1n\pi^*$ state. As we mentioned, even an intersystem crossing to a triplet state is proposed to take place on a picosecond timescale from the vibrationally excited $^1n\pi^*$ state [2].

We will focus in the following on the case of adenine, and the possible appearence of a $n\pi^*$ state playing a (minor) role in the relaxation will be discussed.

1.2 Photophysics of adenine: review

The four bases of DNA can exist in more than one tautomeric form, as we will analyze in detail in the following, and 9H-adenine, whose Lewis structure is shown in Fig.1.3, is one of the most studied nucleobase tautomers. Linear absorption spectroscopy has extensively investigated this molecule. The resulting spectra and the underlying transitions have been characterized, in order to model the possible decay pathways following the UV excitation.

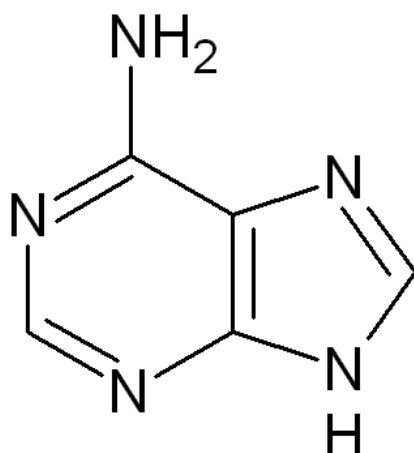The absorption maximum of 9H-adenine at 252 nm is assigned to the

Figure 1.3: Lewis structure of 9H-adenine

close-lying $^1\pi\pi^*$ states, which are labeled L_a and L_b [3, 16]. Another singlet state of $n\pi^*$ character, located at 0.073 eV below the $^1\pi \to \pi^*$ state, is involved in the photoexcitation as a dark state [17].

Pump probe experiments provide time scales for the deactivation dynamics of adenine in the gas phase. Different deactivation times have been found by several groups [11], typically spanning from femtoseconds to picoseconds, or even to nanoseconds. All experiments show a fast deactivation (τ_2) within the range $0.5 - 2$ ps [12, 13, 18, 19, 20]. Most studies reported another, shorter transient below 100 fs. In the group of Ulrich *et al.* [12], a larger time constant on the nanosecond time scale has been measured.

Many theoretical studies have been performed in order to get information about the deactivation dynamics of adenine in the gas phase. Fig. 1.4 depicts schematically each of the paths predicted by theoretical calculations. Colors indicate electronic state character, and are used consistently for all nucleobases. A color gradient indicates an adiabatic change of wavefunction character, as in Fig. 1.4.c.

Fig. 1.5 shows the CIs proposed to be involved in these relaxation decays. Atoms of characteristic geometrical features are given in gold.

Fabiano et al. [15], using Trajectory Surface Hopping (TSH) method, identified processes on two time scales, which they assigned as τ_1 and τ_2. The
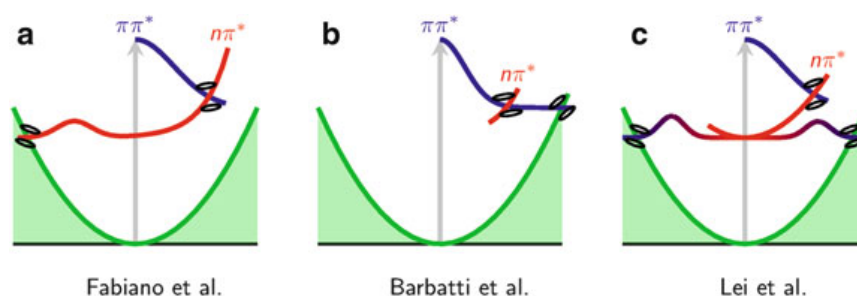
Figure 1.4: Schematic overview of the proposed relaxation mechanisms for adenine from [15, 21, 22] (picture taken from Ref. [11]).
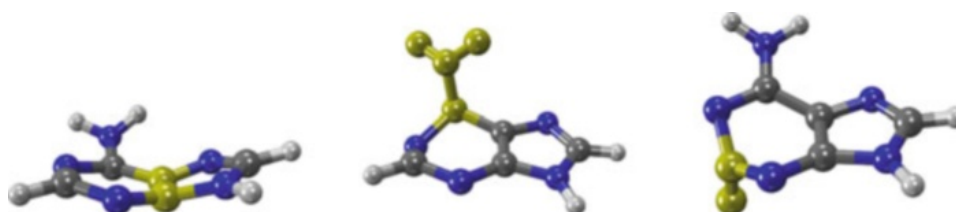

Figure 1.5: Conical intersections proposed for adenine. Left: $S_2 - S_1$ $\pi\pi^* - n\pi^*$ (ring torsion), middle: $S_1 - S_0$ $n\pi^* - gs$ (C_6 -puckered CI), right: $S_1 - S_0$ $\pi - \pi^*$ -gs (C_2 -puckered CI)(picture taken from Ref. [11]).

short time constant was related to the relaxation of the initially populated bright $\pi\pi^*$-state within 15 fs to a dark $n\pi^*$ state through a CI characterized by an angle of about 15° between the planes of the two rings, see Fig. 1.5 left. Once in the $n\pi^*$ state, the deactivation to the ground state takes 560 fs via the C_6-puckered ($n\pi^*$/gs) CI (Fig. 1.5 centre), geometrically characterized by an out-of plane distortion of the amino group (the functional group with the nitrogen atom connected by single bonds to the hydrogen atoms, denoted as NH_2 in Fig. 1.3).

A TSH study was conducted by Barbatti *et al.* [21], leading to time constants which are very similar to the ones obtained by Fabiano [15] but slightly different deactivation pathways were recorded. The first time constant is related to the $S_2 \rightarrow S_1$ decay and the second constant is connected to the $S_1 \rightarrow S_0$ decay (S_n stands for the n-th excited state). In contrast to the previous work the so-called C_2-puckered CI is the major deactivation channel, see Fig. 1.5 (right). Even though a $S_2 \rightarrow S_1$ transition is reported,

the system stays in the $\pi\pi^*$ state, see Fig. 1.4(b). Mean-field analysis by Lei *et al.* [22] employing a density functional-based tight binding (DFTB) approach observed a strong influence of the excitation energy on the relaxation path taken and hence on the relaxation times. Using an excitation energy of 5.0 eV, they observed that the C_6−puckered CI is employed for relaxation. The excited-state lifetime in this case was 1.050 fs. On the other hand, excitation at 4.8 eV activates the channel through the C_2−puckered CI, with an excited-state lifetime of 1.360 fs.

In all cases the initial $\pi\pi^*$ state is reported to change to an intermediate $n\pi^*$ state before reverting to the $\pi\pi^*$ state and accessing the respective CI. Accordingly, the authors state that the final transition back to the ground state happens always from the $\pi\pi^*$ state, even though previous studies report the C_6−puckered CI to be of $n\pi^*$/gs character.

We mention for reason of completeness that Sobolewski, Domcke and coworkers [23, 24], also located another type of CI involving $^1\sigma\pi^*$ states and hydrogen abstraction from the NH and NH_2 groups, but this proposed decay pathway will not be discussed further in the present work, where we focus on the deexcitation processes involving $^1\pi\pi^*$ and $^1n\pi^*$ states.

To sum up, despite the fact that the time constants predicted by several groups by using different methods are similar, the predominant relaxation pathways obtained are different. Depending on the level of theory, either the state character is preserved [21], leading to the C_2-puckered CI, or it changes to $n\pi^*$ [15], leading to a decay via the C_6-puckered CI. It remains unclear which puckering motion is of major importance until dynamical simulations at a more reliable level of theory become possible.

1.3   Base multimer excited states

In actual living cells, a nucleobase interacts with other bases within the same nucleic acid polymer. The structure of nucleic acids allows for interaction within the same strand via stacking and, in the case of double stranded DNA, also for interactions between two strands via hydrogen bonding (base coupling), see Fig. 1.6.

What is experimentally observed is that excess electronic energy relaxes

(a)   (b)

Figure 1.6: Basic assemblies of nucleobases: a)base stacking, b)base pairing (picture taken from Ref.[2]).

by one or two orders of magnitude more slowly in DNA oligo- and polynucleotides compared to the case of single nucleobases. Moreover, absorption spectra closely resemble those of the building block monomers, apart from the decrease of intensity, leading to the well known effect of hypochromism [25]. In the case of single-stranded adenine homopolymers, both ultrafast (≈ 1 ps) and more slowly decaying components are observed [7]. Middleton *et al.* suggest in Ref. [2] that the fast and slow signal components correspond to excitations in unstacked and stacked base regions, respectively. The different decay pathways proposed for both stacked and unstacked DNA single strands are summarized in Fig. 1.7.

The decay in unstacked base strands is hypothesized to occur via the same pathways illustrated in the previous section for the single monomers: relaxation along the $\pi\pi^*$ states, with possible bifurcations to $n\pi^*$ states and intersystem crossings to triplet states.

The analogous decay behaviour observed for isolated bases and unstacked single strands is reasonable and intuitive as, in the unstacked geometrical configuration, single bases are assumed not to be correlated in any way to each other.

On the other side, strands formed by stacks of two or more bases are excited to an exciton state. There is strong evidence [26], that regardless of the length of the sequence, initial excitons trap to a common state that is
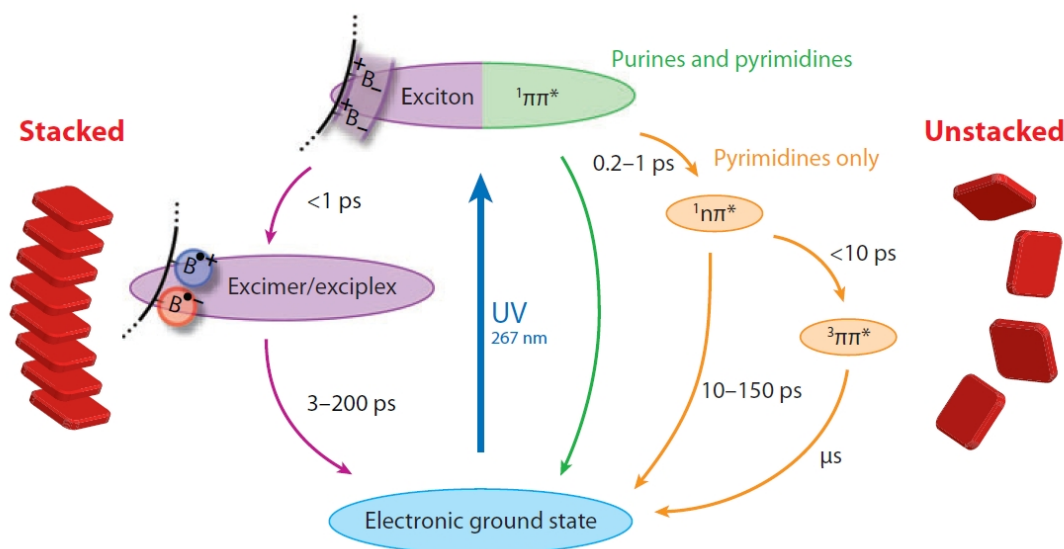
Figure 1.7: Decay pathways for stacked and unstacked DNA single strands (picture taken from Ref. [2]).

localized on just two bases. The exciton decays to an exciplex state in less than 1 ps. The term exciplex/excimer stands for an excited dimer, and it is generally understood to be formed by an electronically excited monomer and a second unexcited one. The energy of the two monomers when bound is lower than the energy of them separated. Here the terms indicate an excited electronic state with strong charge transfer character. The decay of excimer/exciplex states by charge recombination takes place in $3 - 200$ ps and may play a dominant role in the photostability of DNA by guaranteeing that most excited states do not lead to deleterious reactions but instead relax back to the electronic ground state.

Fig. 1.8 describes the simplest situation of the electronic interactions of two identical chromophores (A and B) in terms of locally and charge transfer excited states, depending on the relative position of the excited electron and the corresponding hole. If they are both located on the same monomer, it is the case of a locally excited state, while if the electron moves to a different site, the system gets excited to a charge transfer state.

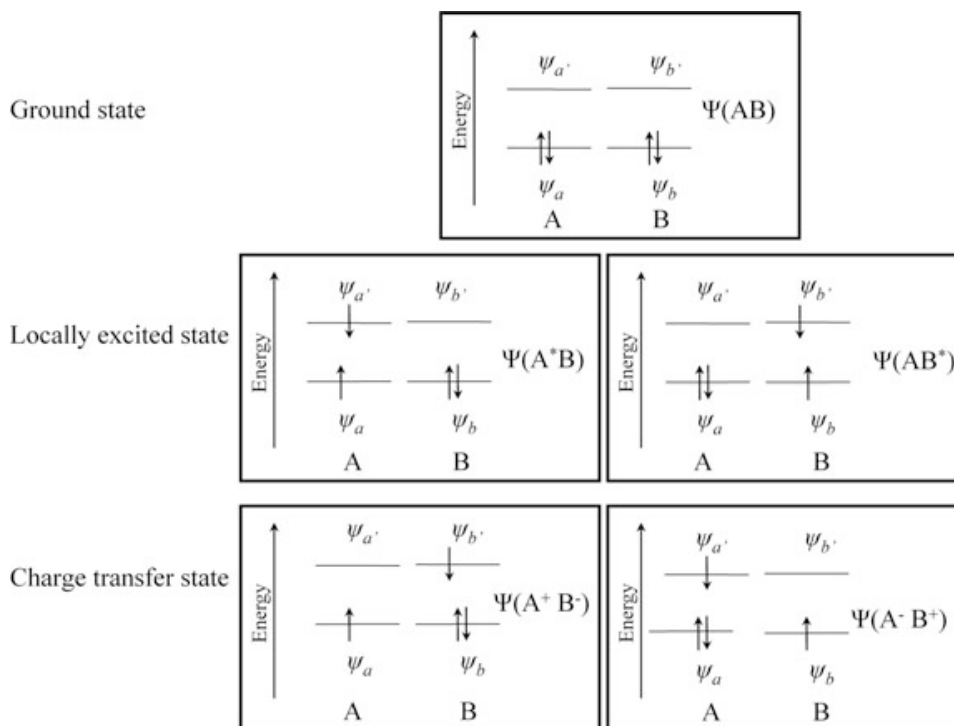The wavefunction of the excited state has the general form

Figure 1.8: Schematic illustration of the electronic interactions of identical chromophores A and B in terms of localized and charge transfer excited states (picture taken from Ref.[27]).

$$\phi(\text{exciplex}) = c_1\Phi(A^*B) + c_2\Phi(AB^*) + c_3\Phi(A^-B^+) + c_4\Phi(A^+B^-) \quad (1.1)$$

where $A = B$, $c_1 = c_2$, and $c_3 = c_4$ for excimers. Excimers and exciplexes are, respectively, excited state complexes formed by two identical or two different molecules. The first two terms correspond to locally excited states and their interaction results in exciton states. At intermolecular separations below $5-6$ $\mathring{A}$, orbital interactions come into play, mediating a mixing of the locally excited states with the charge transfer states, described by the third and fourth terms. It is thus important to distinguish whether the exciton can be described as a linear combination of locally excited states, forming a Frenkel exciton, or whether CT configurations also play a role. The first case can be understood in terms of Frenkel exciton theory. In this framework a model Hamiltonian H is written as the sum of N_{mon} isolated chromophore

Hamiltonians H_m and a coupling term V_{ml}:

$$H = \sum_{m}^{N_{mon}} H_m + \sum_{m} \sum_{l>m} V_{ml}.$$ (1.2)

The singly excited states are described by:

$$\Phi_a = \phi_a^{ex} \prod_{b \neq a} \phi_b$$ (1.3)

where the chromophore a is in the excited state, while the others are in the ground state. The wavefunction of the excitonic state is then written as a linear combination of the wavefunctions of locally excited states:

$$\Psi_k(\text{exciton}) = \sum_{a} c_{ka} \Phi_a.$$ (1.4)

When there are strong orbital interactions between the different fragments, Frenkel exciton theory is no longer sufficient and it is necessary to explicitly include charge transfer configuration in the modeling.

Many models have been developed to investigate the exciton and charge transfer features in the decay paths of DNA single strands. These models perform very well in relation to experiments (see Ref. [8] for a relevant example), but will not be discussed in the following as the current work is focused on studies of single nucleobases.

Chapter 2

Theoretical background

2.1 Basic notions regarding photophysics in biological systems

A multitude of processes may occur when sunlight, filtered through the Earth's atmosphere, interacts with matter. The spectrum of solar radiation striking the Earth spans from 100 nm to 10^6 nm, and can be divided into the ultraviolet (UV) range (100 nm to 400 nm), visible range (400 nm to 700 nm) and infrared (IR) range (700 to 10^6 nm).

Molecular photophysical processes relevant for photobiology include absorption and emission of UV, visible or near-IR light, by molecules. The basic principles of molecular photophysics can be clarified with the help of the Jablonski diagram, named after the polish physicist Aleksander Jablonski. It illustrates the electronic states of a molecule and the transitions between them, see Fig. 2.1.
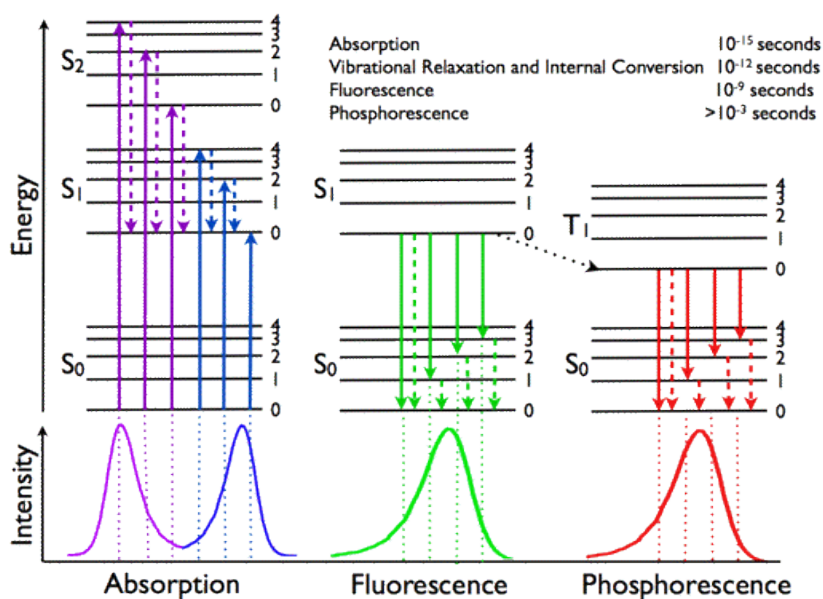
Figure 2.1: Jablonski diagram representing energy levels and related mechanisms underlying absorption, fluorescence and phosphorescence spectra. The singlet states S_1 and S_2 states, the triplet state T_1 and the ground state S_0 involved in the transitions are depicted, including their vibrational structure (picture taken from Ref. [28]).

The elctronic states are arranged vertically by energy and horizontally by spin multiplicity. In the left part of the diagram three singlet states with anti-parallel spin are shown: the singlet ground state (S_0) and two higher singlet excited states (S_1 and S_2). Singlet states are diamagnetic, as they do not interact with an external magnetic field. The triplet state (T_1) is the elctronic state with parallel spins. Transistions between electronic states of the same spin multiplicity are allowed. Transitions between states with different multiplicity are formally forbidden, but may occur due to spin orbit coupling. Processes of this kind are called intersystem crossings. Superimposed on this electronic states are the vibrational states, which are of much smaller energy.
In Fig. 2.1, solid arrows indicate radiative transitions occurring by absorption (violet, blue) or emission (green for fluorescence, red for phospho-

rescence) of a photon. Dashed arrows represent non-radiative transitions. Internal conversion is a non-radiative transition, which occurs when a vibrational state of higher electronic state is coupled to a vibrational state of a lower electronic state. In the notation of, for example, $S_{1,0}$, the first subscript refers to the electronic state (first excited) and the second one to the vibrational sublevel ($v = 0$). In the diagram the following internal conversions are indicated: $S_{2,4} \rightarrow S_{1,0}$, $S_{2,2} \rightarrow S_{1,0}$, $S_{2,0} \rightarrow S_{1,0}$, $S_{2,0} \rightarrow S_{0,0}$. The dotted arrow from $S_{1,0} \rightarrow T_{1,0}$ is a nonradiative transition called intersystem crossing, because it is a transition between states of different multiplicity. Below the diagram sketches of absorption-, fluorescence- and phosphorescence spectra are shown.

When a molecule absorbs a photon of appropriate energy, a valence electron is promoted from the ground state to some vibrational level in the excited singlet manifold. The process is extremely rapid (≈ 1 fs $= 10^{-15}$ s), and this implies that the nuclei of the molecule may be considered as fixed during the transition, because of their much larger mass, and that the Born-Oppenheimer approximation (which will be introduced in the following) is valid. After light absorption, the excited molecule ends up at the lowest vibrational level of S_1 ($S_{1,0}$) via vibrational relaxation and internal conversion, and this radiationless process takes place in about 1 ps (1 ps $= 10^{-12}$ s).

In Fig. 2.1, a sketch of an absorption spectrum consisting of two bands is shown: in the condensed phase, broad absorption bands are observed, rather than the sharp transitions seen for atoms or molecules in the gas phase. This is due to the phenomena known as homogeneous and inhomogeneous broadening. Homogeneous broadening arises from the many vibrational and rotational states, which are all superimposed on the electronic transitions preventing the observation of sharp transitions, while inhomogeneous broadening arises from solvent effects.

The strength of the lowest optical transition is very often expressed in terms of the dimensionless oscillator strenghth f:

$$f = 1.44 \cdot 10^{-19} \int_0^\infty \varepsilon(\sigma)d\sigma \qquad (2.1)$$

where ε is the molar extinction coefficient connected with the lowest electronic transition, σ is the wavenumber and the integral is over the whole range of wavenumbers of the absorption band. For strongly allowed transitions $f \approx 1$. The oscillator strength has a direct relationship with the electronic transition dipole moment $\vec{\mu}_{eg}$, which couples the wavefunctions of the ground (Ψ_g) and excited (Ψ_e) electronic states. It reads

$$\vec{\mu}_{eg} = \int \Psi_e^*(\mathbf{r}) \cdot \vec{\mu} \cdot \Psi_g(\mathbf{r}) \mathrm{d}^3\mathbf{r}, \qquad (2.2)$$

with $\vec{\mu} = -e\mathbf{r}$, and the integration takes place over the spatial coordinate $\mathbf{r}$. This quantity is a measure of the dipole moment associated with the shift of a charge that occurs when electrons are redistributed in the molecule upon excitation. The oscillator strength is proportional to the magnitude of the transition dipole moment, i.e.

$$f \propto |\vec{\mu}_{eg}|^2. \qquad (2.3)$$

Moving to the central inset of Fig. 2.1, the process of fluorescence is depicted. The lowest vibrational level of S_1 is the starting point for fluorescence emission to the ground state S_0, non-radiative decay to S_0 (internal conversion), and transition to the lowest triplet state (intersystem crossing). Fluorescence takes place on the nanosecond timescale (1 ns = 10^{-9} s), and, depending on the molecular species, its duration amounts to $1 - 100$ nanoseconds. It is clear from the Jablonski diagram that fluorescence always originates from the same level, irrespective of which electronic energy level is excited. The emitting state is the zeroth vibrational level of the first excited electronic state $S_{1,0}$. It is for this reason that the fluorescence spectrum is shifted to lower energy than the corresponding absorption spectrum (Stokes shift). The Stokes shift can be enhanced by solvent interactions. We can also conclude from the sketched spectra in Fig. 2.1 that the vibrational fine structure in a fluorescence spectrum reports on vibrations in the ground state, and vibronic bands in an absorption spectrum provide information on vibrations in higher electronic excited states.
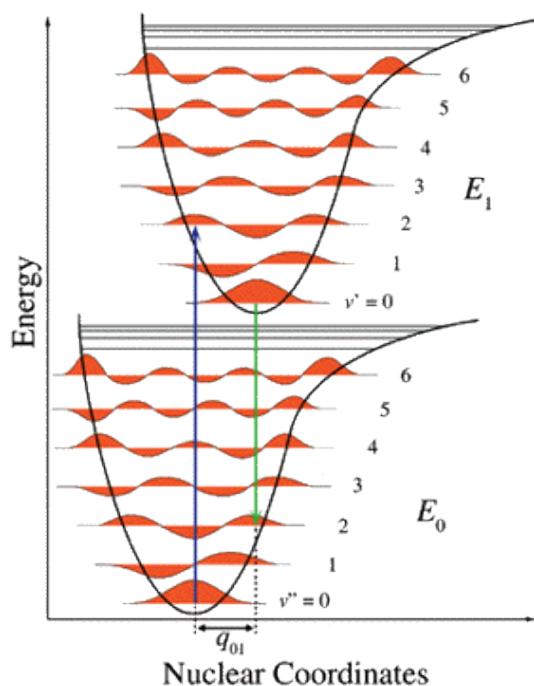
Figure 2.2: Franck Condon principle applied to a two-dimensional potential energy diagram. The potential wells show favored transitions between vibrational sublevels $\nu = 0$ and $\nu = 2$ both for absorption (blue arrow) and emission (green arrow) (picture taken from Wikipedia: Franck Condon Principle, created by Mark M. Somoza).

Another factor that has to be considered in fluorescence spectroscopy is the Franck-Condon factor. If we look at the Jablonski scheme in Fig. 2.1, it can be seen that the fluorescence transition $S_{1,0} \to S_{0,0}$ is not the most intense one. The Franck-Condon principle states that the most intense vibronic transition is from the vibrational state in the ground state to that vibrational state in the excited state vertically above it (Fig. 2.2, blue arrow). The schemes (for absorption and emission) in Fig. 2.2 are simplified two-dimensional potential energy diagrams. Since the excited state is different from the ground state, a displaced minimum nuclear normal coordinate can be expected. It should be noted further that the time to reach the excited state is so short (femtoseconds) that the nuclei positions are virtually unchanged during the electronic transition. In the vibronic wavefunctions,

the nuclear coordinates can then be uncoupled from the electronic coordinates (Born-Oppenheimer principle). The transition dipole can then be factorized into an electronic and a nuclear part according to

$$\vec{\mu}_{eg} = \int \Psi_e^*(\mathbf{r}) \cdot \vec{\mu} \cdot \Psi_g(\mathbf{r}) \mathrm{d}^3 \mathbf{r}_{elect} \int \Psi_v(\mathbf{R}) \cdot \Psi_v(\mathbf{R}) \mathrm{d}^3 \mathbf{R}_{nuc}. \qquad (2.4)$$

The second integral is the so-called Franck-Condon vibrational overlap, which also determines the strength of the electronic transition (or oscillator strength). In the fluorescent part of the scheme in Fig. 2.1, the second and third vibrational transitions ($S_{1,0} \rightarrow S_{0,1}$ and $S_{1,0} \rightarrow S_{0,2}$) have larger Franck-Condon factors than the one between fundamental vibrational wavefunctions $S_{1,0} \rightarrow S_{0,0}$.

In Fig. 2.1, the triplet state is also drawn, from which the process of phosphorescence arises. Once in a different spin state, electrons cannot relax into the ground state quickly: they will reside for a very long time there (from microseconds to seconds) before decaying to the ground state. This is due to the spin-forbidden transitions involved in the (excited) singlet-triplet and triplet-singlet (ground state) transitions. As these transitions occur very slowly in certain materials, absorbed radiation may be re-emitted at a lower intensity and long-lived phosphorescence from this state can be observed.

Because of its long lifetime, the triplet state of an aromatic molecule is the starting point for photochemical reactions.

2.2 Born-Oppenheimer approximation and conical intersections

The theoretical treatment of a molecular system is always based on the selection of an appropriate computational method, with the final goal of solving the Schrödinger equation for the whole system. Because of its complexity, the exact solution of the Schrödinger equation is not possible for most of the molecules of interest. However, the problem can be simplified by applying procedures leading to satisfying approximate solutions. A basic approximation on which all quantum chemistry methods are founded is the Born-Oppenheimer approximation, which will be briefly introduced in the

following.

A system of N atoms located at $\vec{R} = (R_1, R_2, ..., R_l, ..., R_N)$, with n electrons located at $\vec{r} = (r_1, r_2, ..., r_i, ...r_n)$ is described by the time-dependent Schrödinger equation

$$\hat{H}\phi(\vec{r}, \vec{R}; t) = i\hbar\frac{\partial}{\partial t}\phi(\vec{r}, \vec{R}; t) \tag{2.5}$$

with the total Hamiltonian

$$\hat{H}(\vec{r}, \vec{R}) = \hat{T}_n(\vec{R}) + \hat{T}_e(\vec{r}) + \hat{V}_{nn}(\vec{R}) + \hat{V}_{ne}(\vec{r}, \vec{R}) + \hat{V}_{ee}(\vec{r}), \tag{2.6}$$

with

$$\hat{T}(\vec{R}) = -\frac{1}{2}\sum_{I=1}^{N}\frac{\nabla_I^2}{M_I} \tag{2.7}$$

being the sum of the kinetic energy of the nuclei,

$$\hat{T}_e(\vec{r}) = -\frac{1}{2}\sum_{I=1}^{N}\nabla^2 \tag{2.8}$$

being the sum of kinetic energy of the electrons,

$$\hat{V}_{nn}(\vec{R}) = \sum_{I=1}^{N}\sum_{J>1}^{N}\frac{Z_i Z_j}{|\vec{R}_i - \vec{R}_j|} \tag{2.9}$$

being the internuclear repulsion,

$$\hat{V}_{ne}(\vec{r}, \vec{R}) = -\sum_{I=1}^{N}\sum_{i=1}^{n}\frac{Z_I}{|\vec{R}_i - \vec{R}_I|} \tag{2.10}$$

being the electron-nuclear attraction,

$$\hat{V}_{ee}(\vec{r}) = \sum_{i=1}^{n-1}\sum_{J>1}^{n}\frac{1}{|\vec{r}_i - \vec{r}_j|} \tag{2.11}$$

being the interelectronic repulsion.

M_I and Z_I denote the mass and atomic number of the I-th nucleus. The nabla operators ∇_I and ∇_i act on the coordinates of I-th nucleus and i-th electron, respectively. Defining the partial electronic Hamiltonian for fixed nuclei (i.e. the clamped-nuclei part of $\hat{H}$) as

$$\hat{H}_{el} = \hat{T}_e(\vec{r}) + \hat{V}_{nn}(\vec{R}) + \hat{V}_{ne}(\vec{r}, \vec{R}) + \hat{V}_{ee}(\vec{r}) \tag{2.12}$$

we rewrite the total Hamiltonian as

$$\hat{H}(\vec{r}, \vec{R}) = \hat{T}_n(\vec{R}) + \hat{H}_{el}(\vec{r}, \vec{R}). \tag{2.13}$$

We assume that the solutions of the time-independent (electronic) Schrödinger equation,

$$\hat{H}_{el}(\vec{r}, \vec{R})\Phi_k(\vec{r}, \vec{R}) = E_k(\vec{R})\Phi_k(\vec{r}, \vec{R}), \tag{2.14}$$

are known for the clamped nuclei, with a discrete spectrum of $\hat{H}_{el}(\vec{r}, \vec{R})$ and orthonormalized eigenfunctions

$$\int_{-\infty}^{+\infty} \Phi_k^*(\vec{r}, \vec{R})\Phi_l(\vec{r}, \vec{R}) \equiv \langle \Phi_k | \Phi_l \rangle = \sigma_{kl}. \tag{2.15}$$

The total wavefunction ϕ can be expanded in terms of the eigenfunctions of H_{el} since these form a complete set, i.e.,

$$\phi(\vec{r}, \vec{R}; t) = \sum \Phi_l(\vec{r}, \vec{R})\chi_l(\vec{R}, t) \tag{2.16}$$

Insertion of this so-called Born-Oppenheimer ansatz into the time-dependent Schrödinger equation (2.13), followed by multiplication from the left by $\Phi_k^*(\vec{r}, \vec{R})$ and integration over the electronic coordinates, leads to a set of coupled differential equations

$$[\hat{T}_n(\vec{R}) + E_k(\vec{R})]\chi_k + \sum_l \hat{C}_{kl}\chi_l = i\hbar \frac{\partial}{\partial t}\chi_k, \tag{2.17}$$

where the coupling operator $\hat{C}_{kl}$ is defined as

$$\hat{C}_{kl} \equiv <\Psi_k | \hat{T}_n(\vec{R}) | \Psi_l > - \sum_l \frac{\hbar^2}{M_l} < \Psi_k | \nabla_I | \Psi_l > \nabla_I. \tag{2.18}$$

The diagonal term C_{kk} represents a correction to the adiabatic eigenvalue E_k of the electronic Schrödinger equation, Eq. (2.14).

The adiabatic approximation is obtained by taking into account only the diagonal terms, $C_{kk} \equiv <\Psi_k | T_n(\vec{R}) | \Psi_k >$, which results in a complete decoupling

$$[\hat{T}_n(\vec{R}) + E_k(\vec{R}) + \hat{C}_{kk}(\vec{R})]\chi_k = i\hbar \frac{\partial}{\partial t}\chi_k \tag{2.19}$$

of the exact set of differential Eqs. (2.17), (2.18). This implies that the nuclear motion proceeds without changing the quantum state of the electronic

subsystem during time evolution and, correspondingly, the wavefunction (2.16) is reduced to a single term

$$\phi(\vec{r}, \vec{R}; t) \approx \Psi_k(\vec{r}, \vec{R})\chi_k(\vec{r}, \vec{R}), \qquad (2.20)$$

being the direct product of an electronic and a nuclear wavefunction. The last simplification consists in also neglecting the diagonal coupling terms

$$[\hat{T}_n(\vec{R}) + E_k(\vec{R})]\chi_k = i\hbar\frac{\partial}{\partial t}\chi_k \qquad (2.21)$$

which defines the Born-Oppenheimer approximation. The Born-Oppenheimer approximation can be applied to a considerable number of physical situations. However, many theoretical and experimental studies have revealed cases where the Born-Oppenheimer approximation fails, meaning that the total wavefunction is not well approximated by a simple product of an electronic eigenfunction with a vibrational wavefunction (the eigenfunction of the nuclear part of the Schrödinger equation). A particularly relevant failure is encountered in the vicinity of PES crossings (for degenerate or nearly degenerate electronic states). There, molecular motion is determined not only by the PES of the given state but depends also on the topology of the (almost) degenerate PES.

A potential energy surface is the result of solving equation (2.14) for many nuclear configurations, leading to the electronic potential energy as a function of the nuclear coordinates.
In a diatomic molecule there is only one nuclear coordinate, the interatomic distance R_{AB}. In this case, the potential energy 'surface' is more accurately termed a potential energy curve. It describes the potential energy of the system, $U(R_{AB})$, as the two atoms are brought closer to, or moved away from each another.

The concept can be expanded to a tri-atomic molecule such as water where we have two O-H bonds and H-O-H bond angle as variables on which the potential energy of a water molecule will depend. The two O-H bonds can be safely assumed to be equal. Thus, a PES can be drawn mapping the potential energy E of a water molecule as a function of two geometrical parameters, q_1 = O-H bond length and q_2 = H-O-H bond angle. The lowest

point on such a PES will define the equilibrium structure of a water molecule. In Fig. 2.3 a water molecule PES is depicted, including the energy minimum corresponding to the optimized molecular structure for water- O-H bond length of 0.0958 nm and H-O-H bond angle of 104.5°.
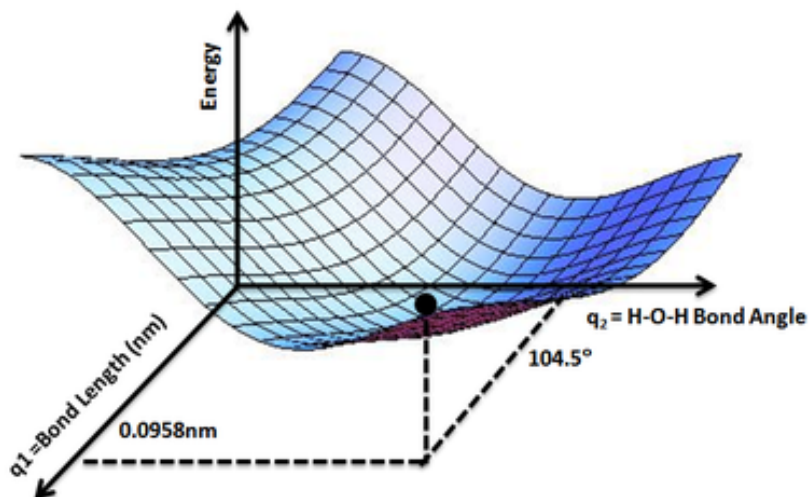

Figure 2.3: PES for a water molecule. The figure shows the energy minimum corresponding to the optimized molecular structure for water: O-H bond length of 0.0958 nm and H-O-H bond angle of 104.5° (picture taken from Wikipedia: Energy profile (chemistry), created by AimNature)).

When computing multiple potential energy surfaces for a system, for instance, the ground state and electronic excited states, the possibility of the surfaces having the same value of potential energy, U(R), occurs. This might be the case, for example, in which a minimum on the upper surface comes into the region of a maximum on the lower surface. What happens at this point is not of straightforward interpretation, a simplified mathematical treatment is given in the following.

The non-crossing rule was quantitatively formulated in 1929 by von Neumann and Wigner [29], proving the theorem put forward earlier by Hund [30], and stating that potential energy curves corresponding to electronic states with the same symmetry properties cannot cross.
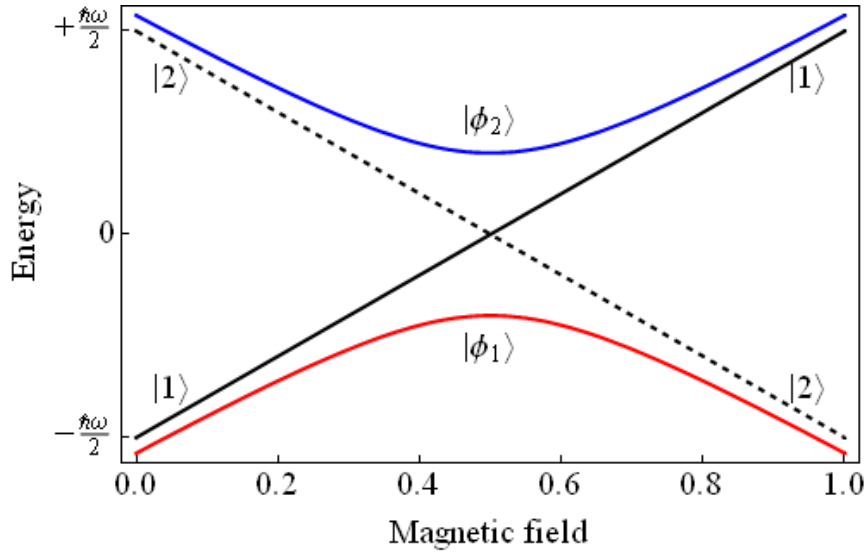
Figure 2.4: An avoided energy-level crossing in a two-level system subjected to an external magnetic field (picture taken from Wikipedia: Adiabatic theorem).

Von Neumann and Wigner gave the mathematical proof for Hund's argument, given here in a contracted form.

Whenever two energy levels E_1 and E_2 come close to each other, the coupling V between the corresponding states is not negligible. The 2×2 matrix Hamiltonian describing the system is given by

$$H = \begin{vmatrix} E_1 & V \\ V & E_2 \end{vmatrix}. \tag{2.22}$$

If the two energies depend on some parameter, e.g. in an approximately linear way, there may be a point where they are degenerate. The eigenvalue equation

$$\begin{vmatrix} E_1 - E & V \\ V & E_2 - E \end{vmatrix} \begin{vmatrix} c_1 \\ c_2 \end{vmatrix} = 0 \tag{2.23}$$

leads to eigenvalues of the Hamiltonian which will not become degenerate, but will have a hyperbolic shape where the minimal energetic distance is $2V$. This is called an avoided crossing. In the (avoided) crossing region, the

two states (e.g. one photonic and the other electronic excitation) become strongly mixed.

Thus far, we have been concerned with potential energy surfaces derived within the Born-Oppenheimer approximation, also known as the adiabatic approximation. Hence, such surfaces are referred to as adiabatic potential energy surfaces. A surface where actual intersections are substituted for the avoided crossings is termed a diabatic surface. If the nuclei are assumed to move slowly, then they are likely to follow a single, adiabatic energy surface, even in the region of an avoided crossing. If the nuclei have sufficient velocity, then the Born-Oppenheimer approximation breaks down and the nuclei may effectively "ignore" the gap in the avoided crossing and simply cross over to the other adiabatic surface, adopting that configuration. This is termed non-adiabatic or "diabatic".

Conical intersections are interesting as they exist between adiabatic surfaces, where we would usually expect an avoided crossing. The distortion observed at a conical intersection is a consequence of the breakdown of the Born-Oppenheimer approximation. At a conical intersection, one can distinguish two directions, X_1 and X_2, such that if the energy in the subspace (the branching space) of these two geometric variables changes (combinations of the bond lengths, angles, etc.), the potential energy would have the form of a double cone in the region of the degeneracy. The remaining $n–2$ directions define the crossing surface (the intersection space) in which the energies of ground and excited states are equal. A movement in the plane (X_1, X_2) from a point on the intersection will result in the degeneracy being lifted. The two vectors X_1 and X_2, defined as

$$X_1 = \frac{\partial(E_1 - E_2)}{\partial q} \tag{2.24}$$

$$X_2 = \langle c_1^t | \frac{\partial H}{\partial q} | c_2 \rangle, \tag{2.25}$$

correspond to the gradient difference vector and non-adiabatic coupling vector, respectively, see Fig. 2.5.
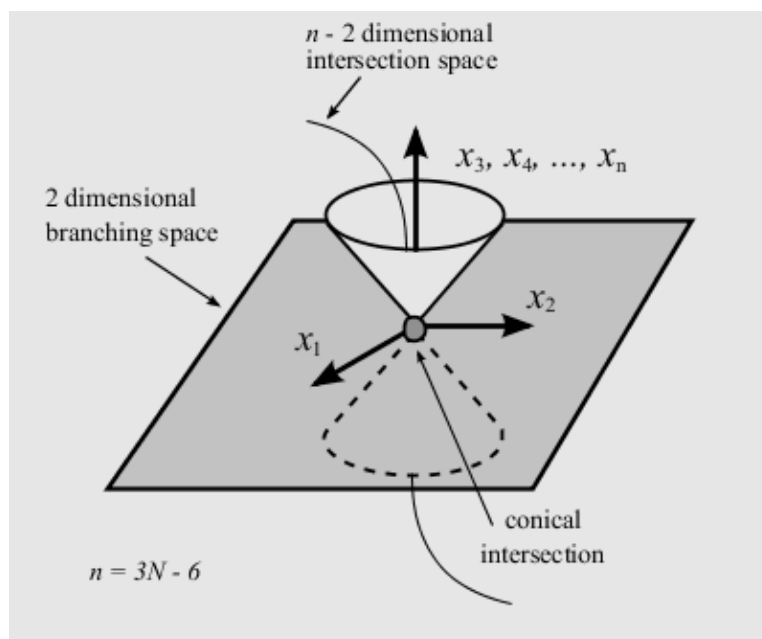
Figure 2.5: A conical intersection as described by a double cone geometry using two variables, X_1 and X_2 (picture taken from: iupac.org, Conical intersections).

The main feature of a conical intersection is its non-adiabatic nature: it is the breakdown of the Born-Oppenheimer approximation that allows non-adiabatic electronic transitions to take place. Clearly, conical intersections facilitate easier transitions compared to avoided crossing, allowing radiationless decay.

2.3   Theory of 2D electronic spectroscopy

Linear spectroscopy measures the first-order polarization induced in a sample by a single interaction with the incident electric field. The most basic method of linear absorption spectroscopy involves a weak light-matter interaction with one primary incident radiation field, and gives a picture of the first excited state manifold of the sample, projected onto a single frequency axis. Transition dipole strengths and excitation energies can be probed, but there is no explicit information about coupling between different excitons or excited state absorption.

In complex systems, where many interacting degrees of freedom are present, the interpretation of linear spectra has to deal with a number of ambiguities. Two representative examples are given in the following.

When an absorption spectrum shows two peaks (see Fig. 2.6), a reasonable question is if these arise from different, non-interacting molecules, or are coupled quantum states of the same molecule. No answer can be obtained from linear absorption spectroscopy, since it cannot resolve couplings or spectral correlations directly, see Fig. 2.7.
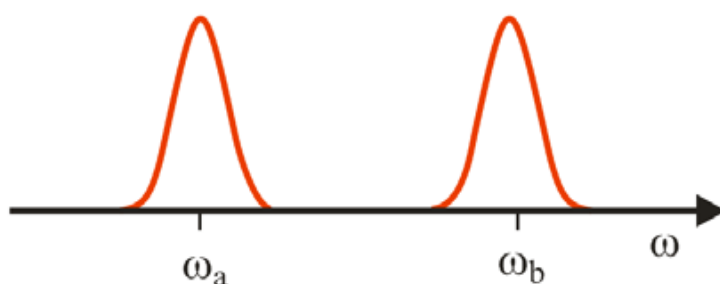

Figure 2.6: Absorption spectrum with two peaks (picture taken from: Tomakoff Group, Nonlinear and Two dimensional Spectroscopy Notes).
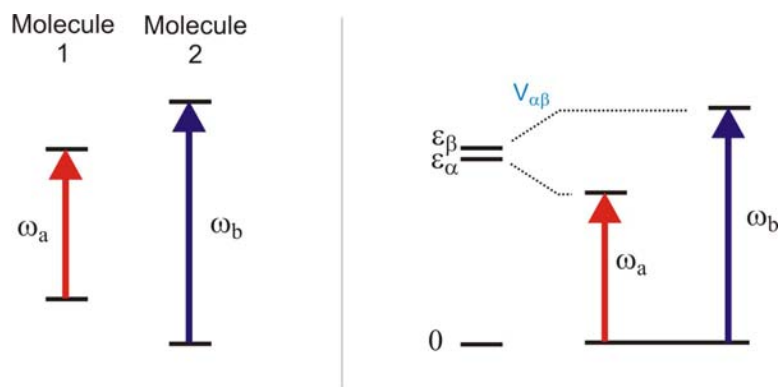

Figure 2.7: Left: excitation of different, noninteracting molecules. Right: coupled quantum states of the same molecule (picture taken from: Tomakoff Group, Nonlinear and Two dimensional Spectroscopy Notes).

Another ambiguous situation one could have to face is the interpretation of broad lineshapes. Distinguishing whether a broadened spectrum comes

from a homogeneous lineshape broadened by fast irreversible relaxation or an inhomogeneous lineshape arising from a static distribution of different frequencies (see Fig. 2.8) is not an easy task, because linear spectra cannot uniquely interpret line-broadening mechanism, or decompose heterogeneous behavior in the sample.
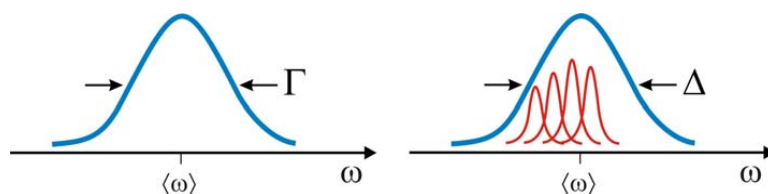

Figure 2.8: Homogeneous (left) and inhomogeneous broadening (right) (picture taken from: Tomakoff Group, Nonlinear and Two dimensional Spectroscopy Notes).

Spectroscopy is the primary tool for describing the molecular structure, interactions and relaxation, the kinetics and the dynamics of such systems. Nonlinear spectroscopy can be used to correlate different spectral features. This technique presents spectroscopic data as a map of spectral interactions between two frequencies, ω_1 and ω_2. They can be thought of as excitation and detection frequencies, respectively.

Two dimensional electronic spectroscopy (2DES) probes the third order polarization generated by the interaction of three carefully timed laser pulses with the sample of interest. First, a broadband pump pulse interacts with the sample, exciting a quantum mechanical coherence between the ground and first excited states. After a time t_1, frequently called the coherence time, a second pump pulse interacts with the sample, creating a population in the ground or excited electronic state. The time t_2 before the third pulse arrives is often referred to as the population time, and it is here that many of the interesting dynamics such as energy and charge transfer occur.

The probe pulse creates a second coherence in the sample, which leads to signal emission at a time t_3 after the probe pulse, based on one of two major processes. The first of these, in which the phase progression reverses in comparison to the first coherence, is called the "rephasing" signal or "photon echo". The other follows a free-induction decay along the original

phase progression and is called a "non-rephasing" signal or sometimes a "virtual echo". To reconstruct a true absorptive 2D spectrum, both of these signals must be obtained and properly combined [31, 32, 33]. The real part of the complex 2DES spectrum will give the absorptive part and the imaginary part produces a dispersive component.

2.3.1 Polarization and density matrix

The theory applied to 2D spectroscopy is generally a mixed quantum-classical framework, in which the incident fields are treated classically, but the material system is described quantum mechanically. The treatment of the bath and the system-bath coupling usually involves averaging over bath degrees of freedom and the system is described by a density matrix ρ. The diagonal elements ρ_{ii} represent populations, while the off-diagonal elements ρ_{ij} give the coherences.

In situations of weak excitation, the time dependence of the density matrix may be expanded perturbatively in powers of the incident electric field:

$$\rho(t) \equiv \rho^{(0)}(t) + \rho^{(1)}(t) + \rho^{(2)}(t) + ... \qquad (2.26)$$

where $\rho^{(n)}(t)$ represents the $n-$th order contribution of the electric field. The $n-$th order density matrix cannot be measured directly. However, it can be probed by measuring the $n-$th order macroscopic polarization, which is related to the expectation value of the dipole operator μ:

$$P^{(n)}(\mathbf{r}, t) = \text{Tr}[\mu\rho^{(n)}(\mathbf{r}, t)] \qquad (2.27)$$

The first order polarization is responsible for linear optical effects. The second order polarization $P^{(2)}$ is involved with nonlinear properties in bire-fringent media, such as sum and difference frequency generation. It can be shown that the signal contribution from $P^{(2)}$ vanishes in isotropic media. Therefore, the next term of interest after the linear optics is $P^{(3)}$, the third order polarization. It is this order that is probed in 2D electronic spectroscopy and other four-wave mixing spectroscopies, such as transient absorption spectroscopy. In the following $P^{(3)}(\mathbf{r}, t)$ will be the quantity of interest.

In the time domain, the third order polarization is a time convolution of the incident electric fields with the third order material response function $R^{(3)}(t_3, t_2, t_1)$ [34]:

$$P^{(3)}(\mathbf{r}, t) = N \int_0^\infty dt_3 \int_0^\infty dt_2 \int_0^\infty dt_1 R^{(3)}(t_3, t_2, t_1) E_3(\mathbf{r}, t - t_3) \quad (2.28)$$

$$E_2(\mathbf{r}, t - t_3 - t_2) E_1(\mathbf{r}, t - t_3 - t_2 - t_1)$$

where $R^{(3)}$ is the third order response function given by

$$R^{(3)}(t_3, t_2, t_1) = \left(\frac{i}{\hbar}\right)^3 \langle V_{\nu 4} | G(t_3) V_{\nu 3} G(t_2) V_{\nu 2} G(t_1) V_{\nu 1} | \rho_0 \rangle. \quad (2.29)$$

The response function describes the full time-dependent, microscopic state of the system for any set of three input pulses arriving at times t_i. The system is initially in the equilibrium state described by the density matrix ρ_0. The dipole operator $V_{\nu i}$ modifies the density matrix following interaction with the i-th pulse, and the field-free molecular time evolution for an interval t_i is given by the Green's function $G(t_i)$. The final interaction $V_{\nu 4}$ is the signal mode giving the final response.

We assume delta function pulses, such that the time intervals are well defined and well-ordered, and the pulses are much shorter than the investigated molecular dynamics. Then, the incoming electric field can be expanded in modes according to

$$E(\mathbf{r}, t) = \sum_j \varepsilon_j(t) \exp(i\mathbf{k}_j \cdot \mathbf{r} - i\omega_j t) + \exp(-i\mathbf{k}_j \cdot \mathbf{r} + i\omega_j t), \quad (2.30)$$

where $\varepsilon(t)$ is the temporal pulse envelope and the summation index j is over the pulse number (input pulses 1-3 and signal s). For the visible and near-IR wavelengths used in 2DES experiments, the pulse wavelengths (400-800 nm) are much lower than the sample size and the approximation $\mathbf{k}_j \mathbf{r} \gg 1$ holds. Therefore, in 2DES experiments, the signals are highly directional, and the signals related to specific energy pathways are chosen through a phase-matching condition. The response function can then be expanded as

$$R^{(3)}(t_3, t_2, t_1) = \left(\frac{i}{\hbar}\right)^3 \sum_l R_l^3(t_3, t_2, t_1) \exp(i\mathbf{k}_l \cdot \mathbf{r} - i\omega_l t) \quad (2.31)$$

The R_l are the response function components associated with each pathway in the signal. Because there are three input pulses, and each pulse can interact with either the ket or the bra (positive or negative frequency), there are $2^3 = 8$ different signals over which the index l iterates. The phase and frequency matching conditions for these are

$$\mathbf{k}_l = \pm\mathbf{k}_1 \pm \mathbf{k}_2 \pm \mathbf{k}_3, \tag{2.32}$$

$$\omega_l = \pm\omega_1 \pm \omega_2 \pm \omega_3 \tag{2.33}$$

The cases in which all the frequency components have the same sign are highly oscillatory and do not contribute largely to the signal and can be neglected by employing the rotating wave approximation. The dominant signals of interest in 2DES are usually referred to as the photon echo, or rephasing, signal ($\mathbf{k}_s = -\mathbf{k}_1 + \mathbf{k}_2 + \mathbf{k}_3$) and the non-rephasing ($\mathbf{k}_s = +\mathbf{k}_1 - \mathbf{k}_2 - \mathbf{k}_3$). The terminology comes from the fact that the phase evolves at conjugate frequencies during the two coherence periods in the rephasing signal but not in the non-rephasing. Thus the former is able to reform into an "echo", while phase evolution in the latter can only continue in the same direction. Contributions to the signal in directions that do not match the phase-matching condition will vanish due to a randomness in the phase [35].

The mathematical notation necessary to describe the various signal pathways associated with the field-matter interactions and density matrix field-free evolution periods can get very complicated. In double sided Feynman diagrams we find a simple tool for graphically representing the various pathways of the time evolution of the density matrix [35, 36].

The Feynman diagrams for the rephasing and non-rephasing pathways are shown in Fig. 2.9 along with the corresponding energy level diagrams. These include contributions from ground state bleach (GSB), excited state emission (ESE) and excited state absorption (ESA), as well as diagrams related to features with common ground states (CGS) or energy transfer (ET).

For a detailed explanation of the formalism underlying double sided Feynman diagrams, see Ref. [34].

In the general case of pathways involved in 2DES, the first pulse will interact with either the ket or the bra. A single pulse interaction places
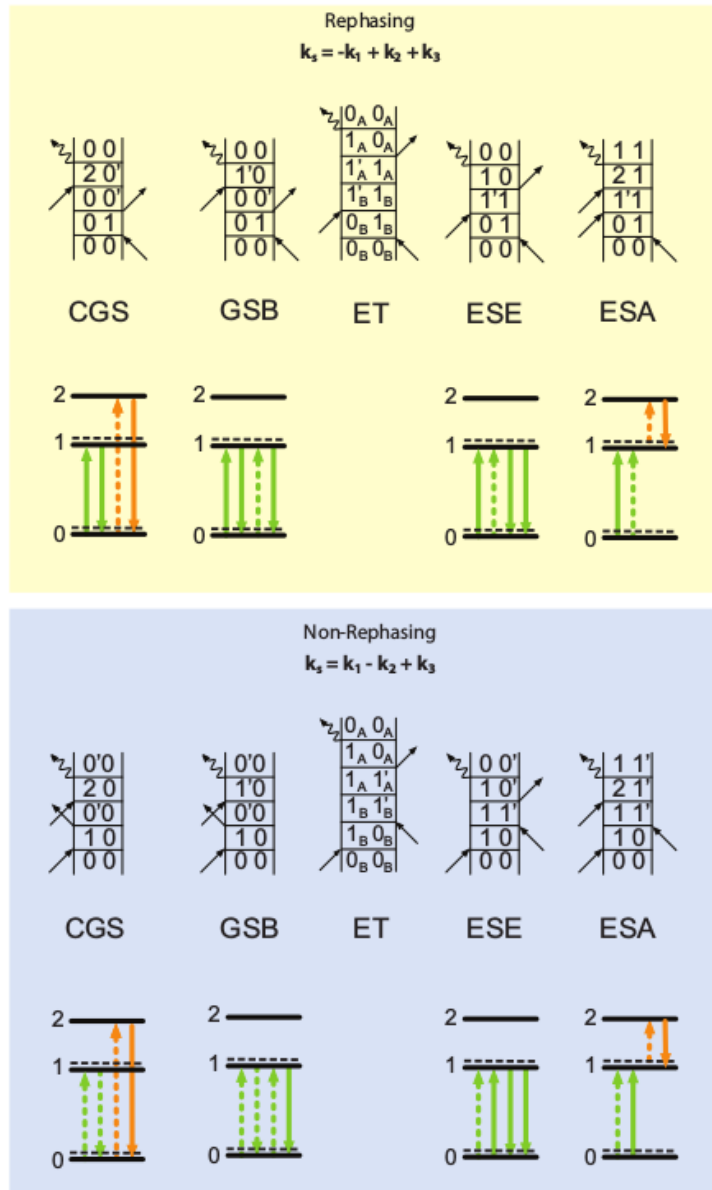
Figure 2.9: Double-sided Feynman diagrams for the rephasing and non-rephasing pathways. The energy levels below show the pulse interactions corresponding to each Feynman diagram. Dotted (solid) lines denote interactions with the ket (bra) (picture taken from Ref. [37]).

the sample in a coherent superposition state, represented by an off-diagonal element in the density matrix ρ_{ij} , which oscillates at the frequency of absorption during the coherence time t_1 as illustrated in Fig. 2.10.
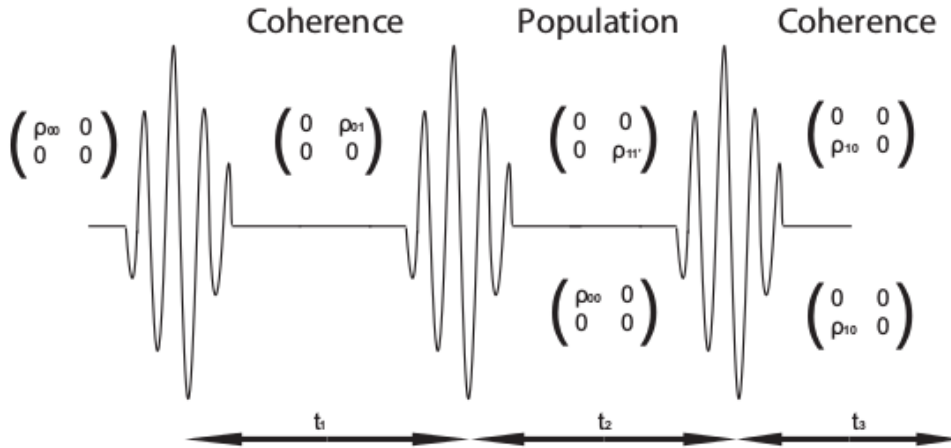

Figure 2.10: A diagram of the density matrix elements involved during coherence and population times for a rephasing signal (picture taken from Ref. [37]).

This coherence decays rapidly due to dephasing processes. After the free evolution with the Green function $G(t_1)$, the second pulse interaction creates a population in either the ground or excited state, corresponding to a diagonal element in the density matrix ρ_{ii}. The time between the second and third pulses (t_2) is often called the "population time". It is during this long-lived period that most of the interesting system dynamics occurs, including for instance energy transfer and charge separation. The third pulse again creates a coherence in the sample. Depending on the frequency of the interaction and available manifold of states, this coherence can be between the ground and first excited state or between the first and second excited state, in the case of excited state absorption. The signal field radiates at a time t_3 after the third pulse in a phase matched direction determined by the pathway involved.

2.3.2   2D spectra

The 2D spectrum contains information about both coherence periods, t_1 and t_3. Generally, t_1 is scanned in small steps and Fourier transformed to a frequency axis ω_1. This axis contains information about the transition to the first excited state and can be considered as a label of the initial excitation frequency. In most cases, the delay t_3 is measured directly in the frequency domain ω_3 to facilitate easier data collection. ω_3 contains frequency information about the second coherence, which is related to the frequency of the third pulse, which probes the state of the sample following the dynamics during the t_2 period. Therefore, the 2D spectrum acts as a correlation map, wherein the ω_1 axis can be thought of as the "excitation axis" and ω_3 is considered the "detection axis". The t_2 delay is fixed for a given spectrum. So, each 2D spectrum is like a snapshot of the sample state at a specific value of t_2. To analyze the kinetics, several spectra must be taken for different values of t_2. A complete scan over t_2 will give a 3D spectrum $S(\omega_1, t_2, \omega_3)$.

To illustrate the types of information available in 2DES data, a cartoon of a simple 2D spectrum is shown in Figure 2.11 along with energy level diagrams indicating the transitions involved in the case of a pair of coupled three-level systems. For cases in which the sample absorbs and emits at the same frequency, a peak shows up along the diagonal, while energy transfer and electronic coupling show up as a cross-peak below the diagonal. Cross-peaks above the diagonal also occur but have generally lower amplitude due to the low probability of uphill energy transfer in most coupling schemes. Excited state absorption is shown as a negative amplitude peak shifted from the diagonal by the anharmonicity. The spectrum also gives a direct measure of the homogeneous and inhomogeneous linewidths as the antidiagonal and diagonal peak widths, which can be used to obtain the frequency-frequency correlation function for a given value of t_2 [38].
To analyze the sample kinetics or any other population dynamics, a series of 2D spectra are acquired, each for a different value of t_2: in this way a complex 3D array of data $S(\omega_1, t_2, \omega_3)$ is obtained. Each 2D spectrum is a frequency-frequency correlation map: given that a chromophore is excited
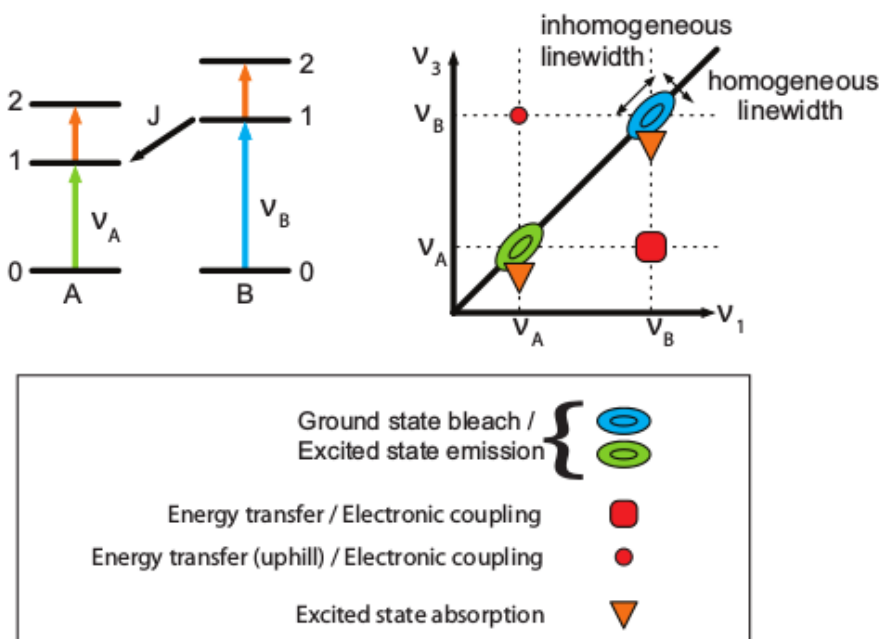
Figure 2.11: Representation of a 2DES spectrum and associated energy level diagrams for a pair of coupled three-level systems (picture taken from Ref. [37]).

at a frequency ω_1, the 2D spectrum shows directly the distribution of frequencies ω_3 at which the sample emits or absorbs after a time t_2.

The information content of a transient absorption (TA) experiment is the same as that of a 2D spectrum integrated over the excitation (ω_1) axis. Analysis of transient absorption (or pump probe) spectra is one of the main points we are going to discuss, among the results presented in this work, see Chapter 5. 2DES is an ideal method for the study of condensed phase systems, including biological complexes in solution, in which the local solvent or protein environment introduces a large degree of inhomogeneous broadening. The technique can reveal homogeneous lineshapes beneath inhomogeneously broadened spectra to provide insight into the physical nature of the broadening. It can also capture couplings, energy and charge transfer, and other rapid spectral dynamics with high time resolution [39].

Chapter 3

Computational methods

3.1 Quantum chemistry calculations

The past few decades have witnessed the development of a hierarchy of quantum chemical methods that can be used to investigate the structures and properties of molecules and solids [40, 41].

Several methods exist with completely different approaches to the solution of the main problem in quantum chemistry, which is the integration of the Schrödinger equation for the considered system. Since an exact solution of the problem is impossible for almost any kind of system, approximation methods are required, which allow to determine electronic structure, to optimize the geometry of molecules and to calculate excitation energies/frequencies and charge distributions.

Properties and reactions in the electronic ground state can be studied routinely by computation: high-level ab initio methods, such as the coupled cluster theory and the Møller–Plesset perturbation theory [42, 43], give accurate predictions for ground-state properties, while fast semiempirical approaches are used for treating large systems [44, 45].

Because of its favorable cost-performance ratio, density functional theory (DFT) is used widely and successfully in studies of chemical reactions [46], and this is the case of the current investigation on nucleobases as well.

3.1.1 Time-Dependent Density Functional Theory (TDDFT)

Generally, two categories of quantum chemical approaches exist for the calculation of excited states. The first kind is the wave-function-based approach, such as the Configuration Interaction (CI), the Multi-Configurational Self-Consistent Field (MCSCF) and the Complete Active Space Perturbation Theory of second order (CASPT2) method [47].

When the number of electrons increases, the wavefunctions become much more complicated and will cost more computing time. Electron-density-based methods become then more convenient, such as time-dependent density functional theory (TDDFT), where the calculation makes use of functionals of the electronic density, and the approximation is due to the proper estimation of the functionals.

TDDFT methods can be very accurate for little computational cost. In recent years, they have been widely used to deal with photochemical properties from small to medium molecules and even large biological systems. In this subsection, we will focus on this popular class of computational methods for excited states.

In density functional theory, the electron density of a molecule is used to determine the energy and derivative properties of molecules. The electron density only depends on three spatial coordinates. It is a function with three variables: x-position, y-position, and z-position of the electrons, $\rho(x, y, z)$. The energy of the molecule is then a functional of the electron density:

$$E = F[\rho(x, y, z)] \tag{3.1}$$

So there is a one-to-one mapping between the electron density of a system and the energy. We can get considerable information about a molecule if we can determine its electron density, which is the fundamental quantity on which density functional theory is based. Compared to ab initio methods, the electron density function is only dependent on three coordinates, independent of the system size. This approach is much faster than ab initio methods.

However, despite its widespread popularity and success, TDDFT still has

limitations in its present form. For instance, the approach fails for strongly correlated systems and underestimates the barriers of chemical reactions and charge transfer excitation energies [48].

The density functional theory is based on the Thomas–Fermi model [49] (developed by Thomas and Fermi in 1927) and the Hohenberg-Kohn theorem [50, 51], set up in 1964 by Hohenberg and Kohn. The first Hohenberg-Kohn theorem states that the ground state electron density uniquely determines the potential and thus all properties of the system, including the many-body wave function. The second Hohenberg-Kohn theorem guarantees the existence of a variational principle for electron densities. Kohn and Sham introduced the Kohn-Sham orbitals and developed the Kohn-Sham theory, bringing the density functional theory into a more practical version. In the Kohn-Sham theorem, the total energy $E[\rho]$ is expressed as

$$E[\rho] = T_s[\rho] + J[\rho] + E_{ne}[\rho] + E_{XC}[\rho], \tag{3.2}$$

where $T_s[\rho]$ is the kinetic energy of a non-interacting system, $J[\rho]$ is the classical electron-electron repulsive (Coulombic) energy, $E_{ne}[\rho]$ is the nuclear-electron attraction energy. The exchange-correlation term $E_{XC}[\rho]$ contains the exchange and correlation effects. In density functional theory, all the approximations lie in the exchange-correlation term. The Kohn-Sham equation is given by

$$\hat{H}_{KS}\Phi_i^{KS} = \epsilon_i \Phi_i^{KS} \tag{3.3}$$

where the Hamiltonian $\hat{H}_{KS}$ can be expressed as:

$$\hat{H}_{KS}(\mathbf{r}) = -\frac{1}{2}\nabla^2 + V_{KS}(\mathbf{r}) \tag{3.4}$$

where

$$V_{KS}(\mathbf{r}) = V_{ne}(\mathbf{r}) + \int \frac{\rho(\mathbf{r}')}{\mathbf{r} - \mathbf{r}'} d\mathbf{r}' + V_{XC}(\mathbf{r}) \tag{3.5}$$

and $V_{XC}[\mathbf{r}]$ is the exchange-correlation term. Equation (3.3) is limited to time-independent systems. The Runge-Gross Theorem [52] is an analogous time-dependent version of the first Hohenberg-Kohn theorem. It states that two external potentials $v(\mathbf{r_1}, t)$ and $v(\mathbf{r_2}, t)$, which differ by more than a

time-dependent constant $C(t)$, result in two different electron densities, that is:

$$v(\mathbf{r_1}, t) \neq v(\mathbf{r_2}, t) + C(t) \rightarrow \rho(\mathbf{r_1}, t) \neq \rho(\mathbf{r_2}, t). \tag{3.6}$$

So there still exists a unique relationship between time-dependent potentials $V(\mathbf{r}, t)$ and time-dependent densities $\rho(\mathbf{r}, t)$. Therefore the property of a system can be written as a functional of the time-dependent density. The Runge-Gross theorem is the rigorous mathematical basis of TDDFT. This is the first step for the extension to the time domain. The next step is the existence of a time-dependent variational principle that is analogous to the second Hohenberg-Kohn theorem [53, 54].

If the wave function $\Psi(\mathbf{r}, t)$ is the solution of the time-dependent Schrödinger equation,

$$i\frac{\partial}{\partial t}\Psi(\mathbf{r}, t) = \hat{H}(\mathbf{r}, t)\Psi(\mathbf{r}, t), \tag{3.7}$$

it is the stationary point of the action integral

$$A = \int_{t_0}^{t_1} dt \langle \Psi(t)| i\frac{\partial}{\partial t} - \hat{H}(t)|\Psi(t)\rangle. \tag{3.8}$$

According to the Runge-Gross theorem, the action integral can be written as a functional of the time-dependent density:

$$A[\rho] = \int_{t_0}^{t_1} dt \langle \Psi[\rho](\mathbf{r}, t)| i\frac{\partial}{\partial t} - \hat{H}(\mathbf{r}, t)|\Psi[\rho](\mathbf{r}, t)\rangle. \tag{3.9}$$

To derive the time-dependent Kohn-Sham equation, a time-dependent non-interacting reference system exists according to van Leeuwen [54]. The time-dependent Kohn-Sham equation is written as

$$i\frac{\partial \Psi_i(\mathbf{r}, t)}{\partial t} = \left(-\frac{1}{2}\nabla_i^2 + v(\mathbf{r}, t) + \int d^3\mathbf{r}' \frac{\rho(\mathbf{r}', t)}{|\mathbf{r} - \mathbf{r}'|} + \frac{\delta A_{XC}[\rho]}{\delta\rho(\mathbf{r}, t)} \right) \Psi_i(\mathbf{r}, t) \tag{3.10}$$

In this case, the A_{XC} part contains all the exchange and correlation effects. There are different approximations for this functional. The DFT theory is extended to the time-dependent domain and developed to time-dependent

density functional theory (TDDFT). Using TDDFT in linear response (deriving the linear response of the time-dependent Kohn-Sham equation) allows us to obtain useful information, such as excitation energies and oscillator strengths of excited states.

TDDFT has become one of the most popular quantum chemical tools to calculate excited-state properties of medium-sized or even large biological molecules from first principles. While accurate high-level calculations such as CASPT2 and CASSCF employing large active spaces are tedious and time consuming, the TDDFT calculation can reach the accuracy of sophisticated quantum chemical methods with moderate computational cost. However, as we already mentioned, there are shortcomings in TDDFT. For instance, the choice of the right exchange-correlation functional for the given excited state property is crucial. As an example, the hybrid functional B3LYP is unsuccessful in some applications: for instance, the lack of long range correlation causes the failure of the approach for treating charge transfer (CT) problems.

In the present studies the TDDFT implementation in the GAUSSIAN quantum chemistry program package has been applied. The functional M062X has been used for the TDDFT calculations.

The M06-2X and CAMB3LYP functionals have been chosen for the purposes of the present study because they perform reasonably well in linear response TDDFT calculations for molecular clusters. In particular, they avoid underestimation of the energies of the states involved in charge-transfer transitions, and do not predict spurious charge- transfer transitions to occur at low energies [55].

3.1.2 Basis sets

Given the calculation method, a basis set has to be chosen to optimally approximate the wavefunction. It is composed of a set of functions, which are linearly combined to approximate molecular orbitals.

A good description is given by Slater-type orbitals (STOs):

$$R(r) = Nr^{n-1}e^{-\zeta r} \tag{3.11}$$

where n is the quantum number, N is the normalizing constant, r is the distance of the electron from the atomic nucleus, and ζ is the constant related to the effective charge of the nucleus.

As they decay exponentially with the distance from the nuclei, STOs accurately describe the long-range overlap between atoms, and reach a maximum at zero, well describing the charge and spin at the nucleus. Due to computational difficulties in realizing them, approximations as linear combination of Gaussian orbitals (GTOs) are more convenient and are mostly chosen for the actual calculations. Hence, in fact, we have

$$R(r) = Br^l e^{-\alpha r^2} \tag{3.12}$$

where l is the angular momentum, and α is the orbital exponent. Since it is easier to calculate overlap and other integrals with Gaussian basis functions, this leads to a huge computational advantage.

There are hundreds of basis sets composed of GTOs, the smallest are called minimal basis sets, and they are typically composed of the minimum number of basis functions required to represent all the electrons on each atom. The most common ones are called STO-nG, where n is the number of Gaussian primitive functions comprising a single basis function. Correlation consistent basis sets (CCBSs) are also used, since they are designed to converge to the complete basis set (CBS) limit. Basis sets of this kind are cc-pVNZ, where N=D,T,Q,5,6,... (D=double, T=triples, etc.). The "cc-p" stands for "correlation-consistent polarized" and the "V" indicates that they are valence-only basis sets. The most common extension to basis sets is the addition of polarization functions, denoted by a *. An improvement of the accuracy also could be reached by making use of "augmented" basis sets, i.e., by using very shallow Gaussian basis functions, which more accurately represent the tail portion of the atomic orbitals, which are distant from the atomic nuclei. This is important for large "soft" molecular systems.

As already mentioned, the functionals M062X and CAMB3LYP have been used for the TDDFT calculations of the current studies, with the aug-cc-pVDZ and aug-cc-pVTZ basis sets.

3.2 Semiclassical nuclear ensemble method

In the current work, linear absorption spectra have been simulated for the main tautomers of nucleobases in their hydrosolvated molecular geometry. The UV-VIS absorption spectra in aqueous solution were modelled using the semiclassical nuclear ensemble method of Crespo-Otero and Barbatti [56]. This method allows the performance sophisticated simulations on molecular systems with a high degree of chemical complexity, taking into account several effects, such as vibrational broadening and solvent effects. It is based on the approximation that the forms of spectral bands are predominantly controlled by the nuclear geometry distribution of the electronic ground state [56]. This approach requires as input a set of N_{pts} ground-state geometries of the molecule of interest $\{R_i\}$, which are usually sampled either from a statistical distribution or from thermostatted molecular dynamics trajectories. The vertical excitation energies $\Delta E_{0n}(R_i)$ for the excitation to the n-th excited state and the associated oscillator strengths $f_{0n}(R_i)$ are computed at each of these geometries. Then, the molecular absorption cross-section σ is calculated as

$$\sigma(E) = \frac{\pi e^2 \hbar}{2 m_e c \varepsilon_0 n_r E} \sum_{n=1}^{N_{\text{fs}}} \frac{1}{N_{\text{pts}}} \sum_{i=1}^{N_{\text{pts}}} \Delta E_{0n}(R_i) f_{0n}(R_i) g(E - \Delta E_{0n}(R_i), \delta).$$

(3.13)

Here, $g(E - \Delta E_{0n}(R_i), \delta)$ is a normalized line-shape function whose purpose is to account for other sources of broadening, such as collisions and finite excited-state lifetime. In practice, the simulated spectra are found to be relatively insensitive to the choice of the line-shape function [57]. n_r denotes the index of refraction of the medium, and m_e is the electron rest mass. N_{fs} is the number of vertical excitation energies calculated for each configuration. In turn, the molecular absorption cross-section σ (expressed in cm^2) is related to the molar extinction coefficient ε (in M^{-1} cm^{-1}) through

$$\varepsilon = \frac{N_{\text{A}} \times 10^{-3}}{\ln(10)} \sigma.$$

(3.14)

The nuclear ensemble method simulates only the envelopes of spectral bands, and cannot predict fine spectral features such as vibrational progressions. For the purposes of the present work, however, this does not represent a

serious drawback, as such features are also unresolved in experimentally de-
termined spectra of nucleobases in solution.

For each molecule under study, $N_{\text{pts}} = 500$ geometries were sampled from
the Wigner quantum harmonic oscillator distribution for the vibrational
ground state, which was generated using the program initcond.pl from the
simulation package Newton-X [59, 60]. $N_{\text{fs}} = 15$ vertical excitation energies
were calculated for each such geometry. A Gaussian line-shape function

$$g(E - \Delta E_{0n}(R_i), \delta) = \sqrt{\frac{2}{\delta^2 \pi}} \exp\left(\frac{-2(E - \Delta E_{0n}(R_i))^2}{\delta^2}\right) \qquad (3.15)$$

was used, with the broadening parameter set to $\delta = 0.2$ eV. The index of
refraction of the aqueous solution was taken to be independent of the wave-
length, with a value of $n_r = 1.36$. In the present studies, the implementation
in the GAUSSIAN quantum chemistry program packages has been applied
[61]. The functionals M062X and CAMB3LYP with the aug-cc-pVDZ basis
set have been used for the TDDFT calculations.
The results obtained for linear absorption spectra of nucleobases by applying
the semiclassical nuclear ensemble method are described in Chapter 4.

3.3   TNL and HEOM methods for the solution of Non-markovian Master Equation

Molecules in solution are under the influence of the environment, which
leads, among other effects, to strong damping of vibrational motion. There-
fore, it is necessary to employ simulation methods that include the effect
of environmental damping. While damping can be included in the wave
function formalism of quantum mechanics at a phenomenological level, only
the density matrix formalism allows a proper treatment of decoherence and
dissipation.
The employed methods for the treatment of adenine in aqueous solution as
an open quantum system will be presented in the following. This sets the
framework for the calculations of 2D spectra discussed in Chapter 5.

3.3.1 Open quantum systems

In the experimental reality, any system is in contact with a solution (hereafter called environment or bath) and therefore must be treated as an open quantum system. The whole system (system+environment) can be well described by the following model Hamiltonian [58, 64]

$$H_{total} = H_s + H_b + H_{sb}, \tag{3.16}$$

where H_s is the system Hamiltonian, H_{sb} is the system-environment coupling, and H_b is the Hamiltonian model for the bath. Additionally, we can consider a factorized initial state $W(t = t_0) = \rho(t_0) \otimes R_0$ at an initial time t_0 when the interaction is turned on. There, $\rho(t_0)$ and R_0 are the initial state of the system and the environment, respectively. The latter can be assumed to be formed by a collection of harmonic oscillators, which generate Gaussian fluctuations for the system of interest [58, 64].

In the simplest case, one can assume the weak coupling regime and invoke the Markov approximation, neglecting any memory effects on the dynamics of the reduced density matrix $\rho(t)$. The latter is obtained after the harmonic bath has been traced out. In the regime of weak coupling, the Born approximation is performed as well, leading to the Born-Markov master equation for the reduced density operator. The bath is only of indirect interest, and its properties need only to be specified in general terms, e.g., by the temperature and its spectral density function. The simplest case is the one of frequency independent damping, which is realized by an Ohmic spectral density $J(\omega) = m\gamma\omega e^{-\omega/\omega_c}$. Therein, γ and ω_c are the damping constant and a cut-off frequency, which is taken to be the largest frequency in the model. The reduced density matrix $\rho(t)$ then evolves according to the equation of motion

$$\dot{\rho}(t) = D[\rho(t)], \tag{3.17}$$

where D is the Liouvillian superoperator, which is composed of a coherent part $\mathcal{L}_0$ describing the dynamics of the uncoupled system, and a dissipative part $\mathcal{L}$ encompassing the dissipative effects and yielding to the transition rates for the relaxation processes, i.e.

$$D = \mathcal{L}_0 + \mathcal{L} . \tag{3.18}$$

The most convenient way to integrate Eq. (3.17) is to solve the eigenvalue problem for D [65]. The latter is not a hermitian operator, i.e., in general we cannot find a set of eigenoperators where D is diagonal. However, it is possible to find its right and left eigenoperators,

$$Dv^k = \lambda_k v^k, \tag{3.19}$$

$$v_k D = \lambda_k v_k, \tag{3.20}$$

where λ_k are complex numbers. Solving the above eigenvalues problem, the reduced density operators can be written as:

$$\rho(t) = \sum_k c_k e^{\lambda_k t} \rho^k + \rho^\infty \tag{3.21}$$

where $c_k = \text{Tr}\left\{\rho(0)v_k^\dagger\right\}$, and ρ^∞ corresponds to the right eigenvector with zero eigenvalue. For a more detailed treatment of theory and calculations, see Ref. [65].

Many attempts have been made to go beyond the Markov approximation. One of the available approaches is a time nonlocal method based on a numerical decomposition of the spectral density [66]. We will describe this Time Nonlocal (TNL) method in the following.

3.3.2 Time Nonlocal method

The total Hamiltonian of the system-plus-bath complex can be written as the sum of four terms,

$$H = H_s + H_b + H_{sb} + H_{ren}, \tag{3.22}$$

where H_s is the system Hamiltonian, H_{sb} is the system-environment coupling, H_b is the Hamiltonian model for the bath and H_{ren} is the renormalization term. In

$$H_s = \frac{p^2}{2M} + V(q) + W(q,t), \tag{3.23}$$

the potential is split into a time-independent part $V(q)$ and an explicitly time-dependent part $W(q,t)$ which, for example, may represent a laser field. The bath Hamiltonian is taken as the sum of harmonic oscillators with mass m_i and frequency ω_i:

$$H_b = \frac{1}{2} \sum_{i=1} N \left(\frac{p_i^2}{m_i} + m_i \omega_i^2 x_i^2 \right). \tag{3.24}$$

The other two terms are the interaction Hamiltonian, which is assumed to be separable,

$$H_{sb} = -K(q) \sum_{i=1}^{N} c_i x_i, \tag{3.25}$$

and the renormalization

$$H_{ren} = K(q)^2 \sum_{i=1} N \frac{c_i^2}{2m_i \omega_i^2} = K(q)^2 \frac{\mu}{2}, \tag{3.26}$$

introduced to avoid artificial shifts in the system potential due to the coupling to the bath. If the coupling is assumed to be bilinear (i.e. $F(q) = q$) the previous equations lead to the so-called Caldeira-Leggett Hamiltonian

$$H = \frac{p^2}{2M} + V(q) + W(q,t) + \frac{1}{2} \sum_{i=1}^{N} \left[\frac{p_i^2}{m_i} + m_i \omega_i^2 \left(x_i - \frac{c_i}{m_i \omega_i^2} q \right)^2 \right]. \tag{3.27}$$

The coupling between the system and the bath is linear in the bath coordinate. Introducing a spectral density of the bath oscillators by

$$J(\omega) = \pi \sum_{i=1}^{N} \frac{c_i^2}{2m_i \omega_i} \delta(\omega - \omega_i), \tag{3.28}$$

a correlation function can be defined by

$$c(t) = \int_0^\infty \frac{d\omega}{2\pi} J(\omega) \cos(\omega t) \coth\left(\frac{\hbar \beta \omega}{2} \right) \tag{3.29}$$

$$-i \int_0^\infty \frac{d\omega}{2\pi} J(\omega) \sin(\omega t) = a(t) - ib(t). \tag{3.30}$$

In terms of the spectral density, the potential renormalization is then given by $\mu = \int_0^\infty (d\omega/2\pi)(J(\omega)/\omega)$. Hence, the bath is fully characterized by its spectral density and by temperature $T = 1/(k_b \beta)$.

Non-Markovian master equation

Starting from the Liouville equation

$$\dot{\rho}_T = -\frac{i}{\hbar}[H_T, \rho_T] \tag{3.31}$$

where ρ_T is the density matrix of the total system formed by system and bath, one can perform a projection onto the system subspace. The projector formalism of Nakajima–Zwanzig [67, 68] allows to separate the dynamics of the bath from the one of the system under consideration. A suitable projector onto the system subspace is defined by $P = \rho_b^{eq} \text{tr}_b$, with $\text{tr}_b \rho_b^{eq} = 1$ and and $Q = (1 - P)$. Applying this projector to Eq. (3.31) and integrating out the degrees of freedom of the bath, we get a master equation for the time evolution of the reduced system density operator, this time without invoking the Markov equation. This implies taking into account the memory of the system induced by the bath fluctuations.

It is shown rigorously in Ref. [69], how the master equation can be recast into a set of coupled, time-local first-order differential equations for the system density matrix and N auxiliary density matrices that account for memory and all initial correlations. The key of this is a parametrization of the spectral density in the form

$$J(\omega) = \frac{\pi}{2} \sum_{k=1}^{N} p_k \frac{\omega}{[(\omega + \Omega_k)^2 + \Gamma_k^2][(\omega - \Omega_k)^2 + \Gamma_k^2]} \tag{3.32}$$

with arbitrary parameters p_k, Ω_k and Γ_k. This set of parameters approximates a given expression for the spectral density very accurately. This is the case of Ohmic environment with peaks.

The procedure is described in Ref. [69] and can be viewed as a replacement of an infinite collection of bath oscillators by a small numbers of special systems, evolving in time under non-Hermitian dynamics, but having the same effect to the system as a bath with a continuous spectral distribution.

Linear absorption spectra

We have used the first-order transition dipole moment correlation function to calculate the absorption spectra defined by

$$I(\omega) \propto \omega \int_{-\infty}^{+\infty} dt e^{i\omega t} \langle \boldsymbol{\mu}(t)\boldsymbol{\mu}(0)\rangle_g, \tag{3.33}$$

The correlation functions can be calculated as $\langle \boldsymbol{\mu}(t)\boldsymbol{\mu}(0)\rangle_g = tr_S\{\boldsymbol{\mu} tr_B[e^{-iHt}\boldsymbol{\mu}\rho_g e^{iHt}]\}$, where

$$\mu = \sum_{m=1}^{N} \mu_m(a_m + a_m^\dagger) \tag{3.34}$$

μ_m is the transition dipole moment of the m-th molecule, a_m and $a_m^\dagger$ are respectively the creation and annihilation operators of the electronic excitation on the m-th molecule.

2D spectra

For the calculation of two-dimensional spectra, we have applied the equation of motion-phase matching approach (EOM-PMA) established in Ref. [70]. In the EOM-PMA, the induced polarization in the direction of the photon-echo signal is calculated by the simultaneous propagation of three auxiliary density matrices ($\rho_1(t)$, $\rho_2(t)$, and $\rho_3(t)$), each of which obeys a modified effective equation of motion according to

$$\dot{\rho}_1(t) = -i[H_s - V_1(t,t_1) - V_2^\dagger(t,t_2) - V_3^\dagger(t,t_3), \rho_1(t)] - \Re(t)\rho_1(t),$$
$$\dot{\rho}_2(t) = -i[H_s - V_1(t,t_1) - V_2^\dagger(t,t_2), \rho_2(t)] - \Re(t)\rho_2(t), \tag{3.35}$$
$$\dot{\rho}_3(t) = -i[H_s - V_1(t,t_1) - V_3^\dagger(t,t_3), \rho_3(t)] - \Re(t)\rho_3(t),$$

where $V_\alpha(t,t_\alpha) = XAe^{-(t-t_\alpha)^2/2\Gamma^2}e^{i\omega t}$, X is the transition dipole operator, Γ is the pulse duration, and $\Re$ is a relaxation superoperator. All three above master equations were calculated by adopting the TNL method [69] to the auxiliary density operators with the corresponding different time-dependent Hamiltonians, see Eq. (3.36).

$$\dot{\rho}_s(t) = \mathrm{L}_s^{eff}(t)\rho_s(t) + \lambda \left[\sum_{k=1}^{n_r} \alpha_k^r \mathrm{L}^- \rho_k^r(t) + \sum_{k=1}^{n_i} \alpha_k^i \mathrm{L}^- \rho_k^i(t) \right],$$

$$\dot{\rho}_k^r(t) = (\mathrm{L}_s(t) + \gamma_k^r)\rho_k^r(t) + \lambda \mathrm{L}^- \rho_s(t), \quad k = 1, \ldots, n_r,$$

$$\dot{\rho}_k^i(t) = (\mathrm{L}_s(t) + \gamma_k^i)\rho_k^i(t) + \lambda \mathrm{L}^+ \rho_s(t), \quad k = 1, \ldots, n_i.$$

(3.36)

Then, the third-order induced polarization is obtained as

$$P_{PE}(t_1, t_2, t_3, t) = e^{i\mathbf{k_s} \cdot \mathbf{r}} \langle X(\rho_1(t) - \rho_2(t) - \rho_3(t)) \rangle + c.c., \qquad (3.37)$$

where the brackets $\langle \ldots \rangle$ indicate the evaluation of the trace.

The total 2D Fourier-transformed spectrum is then given by the double Fourier transform of the photon-echo polarization signal with respect to the delay time $\tau = t_2 - t_1$ and t according to

$$S_{PE}(\omega_\tau, T, \omega_t) \sim \int_{-\infty}^{+\infty} d\tau \int_{-\infty}^{+\infty} dt e^{-i\omega_\tau \tau} e^{i\omega_t t} P_{PE}(\tau, T, t). \qquad (3.38)$$

Here, ω_τ is the "coherence" frequency, ω_t is the detection frequency, and T is "waiting" time given by the difference between t_3 and t_2.

3.3.3 HEOM method

The hierarchy of equations of motion (HEOM) approach is a popular method for simulating non-Markovian quantum dynamics in open quantum systems. Initially proposed by Tanimura and Kubo in 1989 [71], it was developed over the following 20 years. In recent years, the method has been applied to study various problems such as two-dimensional optical spectroscopy of light harvesting complexes [72], DNA [73], electron transfer systems [74], quantum impurity systems [75] and fermionic systems [76].

In this work, we propose an extension of the hierarchy of equations of motion method to describe conical intersections. We focus in particular on a conical intersection between an excited state and the ground state and between two excited states. We use our model to calculate two-dimensional optical spectra of a model for the nucleobase adenine. In this way, we include relaxation mechanisms to the ground state in spectroscopic calculations in a detailed way. We calculate two-dimensional optical spectra to connect with experiment.

In order to describe damping, we couple the system Hamiltonian to a bath consisting of infinitely many harmonic oscillators. We then propagate the damped dynamics using a generalization of the hierarchy of equations of motion method. Two-dimensional optical spectra can be calculated with the standard perturbative method, see Ref. [34].

The Hamiltonian is given as the sum of a Hamiltonian for the two potential energy surfaces and a Hamiltonian for their coupling to the harmonic oscillator bath. In order to derive it, we generalize the treatment by Tanaka and Tanimura [77]. The first part of the Hamiltonian for a three-state model is given by

$$H_P = \epsilon_e |e\rangle\langle e| + \epsilon_d |d\rangle\langle d| + M_2\Omega_2^2 Q_2 d_e D_2 |e\rangle\langle e| + M_2\Omega_2^2 Q_2 d_d D_2 |d\rangle\langle d| + \quad (3.39)$$

$$+ M_1\Omega_1^2 Q_1 D_1 (d_{V1}|d\rangle\langle e| + d_{V2}|g\rangle\langle d| + \text{h.c.}).$$

Q_1 and Q_2 are respectively the coupling and the tuning coordinates, involved in Eq. (3.39). The diabatic state energies vary along Q_2, while along Q_1 variations of the coupling between diabatic states are observed.

The harmonic potentials for the tuning and coupling coordinates and the conjugate momenta are described by

$$H_H = \frac{P_1^2}{2M_1} + \frac{P_2^2}{2M_2} + \frac{1}{2}M_1\Omega_1^2 Q_1^2 + \frac{1}{2}M_2\Omega_2^2 Q_2^2. \quad (3.40)$$

The interaction of the coupling and tuning modes with the bath is given by the Hamiltonian

$$H_{SB} = \sum_\alpha \left\{ \frac{p_\alpha^2}{2m_\alpha} + \frac{1}{2}m_\alpha\omega_\alpha^2 (x_\alpha - \frac{g_{1\alpha}}{m_\alpha\omega_\alpha^2}Q_1)^2 + \frac{1}{2}m_\alpha\omega_\alpha^2 (x_\alpha - \frac{g_{2\alpha}}{m_\alpha\omega_\alpha^2}Q_2)^2 \right\}$$
$$(3.41)$$

The spectral densities are defined as

$$J_i(\omega) = \sum_\alpha \frac{g_{i\alpha}^2}{2m_\alpha\omega_\alpha}\delta(\omega - \omega_\alpha), \quad (3.42)$$

and are chosen to be Ohmic,

$$J_i(\omega) = M_i\gamma_i\omega \exp -\omega/\Lambda. \quad (3.43)$$

g is the strength of the coupling to a single bath mode, γ describes the strength of the coupling to the heat bath, and Λ is a cut-off frequency,

which we assume to be larger than all other frequencies in the system, so that it can be set to infinity.

Through a canonical transformation, see Ref. [78], the Hamiltonian is rewritten as

$$H = \epsilon |e\rangle\langle e| - (d_g |g\rangle\langle g| + d_e |e\rangle\langle e|) \sum_\alpha g'_{2\alpha} x'_\alpha - d_V (|g\rangle\langle e| + \text{h.c.}) \sum_\alpha g'_{1\alpha} x'_\alpha. \tag{3.44}$$

The transformed spectral density is

$$J'_i = 2\hbar\lambda_i \frac{\gamma_i \Omega_i^2 \omega}{(\Omega_i^2 - \omega^2)^2 + \gamma_i^2 \omega^2}, \tag{3.45}$$

where $i = 1, 2$ and $\lambda_i = M_i D_i^2 \Omega_i^2 / 2\pi\hbar$.

In the overdamped limit, we choose $\omega_{c,i} \ll \Omega_i$ and derive the spectral density

$$J_{i\text{OD}}(\omega) = 2\lambda_i \omega_{c,i} \frac{\omega}{\omega^2 + \omega_{c,i}^2}, \tag{3.46}$$

where $\omega_{c,i} = \Omega_i^2 / \gamma_i$.

The model is thus characterized by the excitation energies ϵ_e and ϵ_d, the displacements $d_d^2 \lambda_2$, $d_e^2 \lambda_2$, $d_{V1}^2 \lambda_1$ and $d_{V2}^2 \lambda_1$ and the cut-off frequencies of the overdamped bath $\omega_{c,1}$ and $\omega_{c,2}$. The fact that only the combination $d^2\lambda$ appears (and not the two parameters d and λ, independently from each other) can be seen from Eq. (3.44) and the definition of the spectral density. A hierarchy of equations of motion can be derived by generalizing the treatment in Refs.[77, 79] to two coordinates and overdamped baths.

Chapter 4

Linear absorption spectra of DNA nucleobases

We have performed quantum chemistry calculations by using the density functional theory (DFT) and time-dependent density functional theory (TDDFT) methods and applying the semiclassical nuclear ensemble method of Crespo-Otero and Barbatti [56] to model the UV-VIS absorption spectra of the main tautomers of DNA nucleobases in aqueous solution. Electron Density Difference Maps (EDDMs) have been derived in order to visualize the electronic distribution in the excited states, and define the kind of orbitals involved in the excitations. The obtained results are presented in this chapter and compared with the available experimental data. The results from the present chapter are systematically collected in the submitted manuscript [80].

The photophysics and photochemistry of DNA/RNA bases and their components has been the focus of considerable research effort due to its fundamental importance in several scientific disciplines [1]. A major issue is the absorption spectrum of DNA of solar UV radiation in the so-called UV-B spectral region in the range of wavelengths of 280-315 nm. The photochemical products after UV-B absorption include cyclobutane pyrimidine dimers. They generate cojoined lesions of neighboring thymidine bases within the DNA strand which are cytotoxic and can lead to carcinogenic mutations

[81, 82]. On the other hand, the prevalence of UV-B irradiation on the early Earth is hypothesized to have exerted an increased selective pressure in prebiotic chemistry, such that the five canonical DNA and RNA nucleobases were favored. In particular, their evolutionary success could be explained by their rather high photostability owing to their ability to dump solar photon energy efficiently via non-radiative decay processes [83]. Interestingly enough, this pronounced feature does not occur in potential alternative nucleobases which lack this advantageous property [84, 85]. In addition, it should be noted that once the bases are incorporated into either DNA or RNA strands, the excited state lifetimes change enormously and it is now clear that the most relevant excited states within biologically relevant DNA/RNA involve potentially long lived, high reactive, excited states - in contrast to what is observed for the isolated bases. The conventional view correlating excited state lifetimes of nucleobases to evolutionary selection needs to be challenged. It is certainly important to try to understand the effect of the environment on the excited state properties of the core chromophore in DNA/RNA as well as the effect of structural changes to the nucleobase moeity in the process of DNA/RNA formation. This is the starting motivation of the present work, with the focus on the nucleobases and the role of the surrounding water on their electronic structure.

Reflecting the biological importance of nucleobases, which are the chromophores of DNA and RNA, their photoabsorption spectra and their relaxation processes and pathways following photoexcitation have been the subject of numerous studies. In particular, various levels of electronic structure theory have been applied. A recent perspective article provides a detailed review of the current state of the art [83]. With some notable exceptions [86, 87, 88, 89, 90, 91, 92, 93, 94, 95, 96], most the studies existing to date have concentrated on nucleobases as isolated molecules in the gas phase, neglecting a careful description of their interactions with their environmental degrees of freedom. A recent overview of the current state of the art of advanced computational studies of the excited states of nucleobases in solution is given in Ref. [86]. The lowest few electronic excitations of a π-stacked adenine dimer in its DNA geometry were determined, in the gas phase and in a water cluster, using a long-range-corrected version of time-dependent density

functional theory that asymptotically incorporates Hartree-Fock exchange [87]. A major finding was that the implemented parametrized effective long-range correction can eliminate the underestimation of charge-transfer excitation energies that plagues conventional TDDFT in calculations for molecular clusters. However, this is at the expense of introducing an additional adjustable parameter that determines the length scale on which the Hartree-Fock exchange is turned on. By applying [88] a mixed quantum mechanical/molecular mechanical (QM/MM) approach, the photoinduced nonadiabatic decay dynamics of 9H-adenine in aqueous solution was investigated by surface-hopping simulations. In particular, molecular dynamics simulations in terms of an effective force field model were used to describe the continuous solvent classically. On a similar footing at the semiempirical level, notable solvent-induced shifts in the computed vertical excitation energies (up to about 0.4 eV) were produced [89]. The importance of a nonadiabatic proton transfer for the photostability of the molecular building blocks of RNA and DNA has been revealed by ab initio investigations on a syn and an anti conformer of adenosine exhibiting an intramolecular hydrogen bond [90]. Using a correlated ab initio methodology within a QM/MM framework to calculate the excited states and potential surfaces of the adenine dinucleotide in gas phase and in solution, the formation of exciplexes with remarkably short intermolecular separation has been reported [91]. The complicated interplay of collective electronic effects, excitonic coupling, hydrogen-bonding interactions, local steric hindrance, charge transfer, and environmental and solvent effects and its impact on DNA oligomers and polymers is surveyed in Ref. [92]. In particular, the role of localized vs delocalized excitations and the extent to which they determine the nature and the temporal evolution of the initial photoexcitation in DNA strands was revealed. Using excited-state nonadiabatic dynamics simulations based on second-order algebraic diagrammatic construction (ADC(2)), it is shown in Ref. [93] that 7H-adenine in water cluster relaxes via a state intersection induced by electron transfer from water to the chromophore, indicating the decisive role of the hydration shell for the photorelaxation. By adding 2-aminopurine (2AP) as a fluorescent replacement for purine in DNA bases and exploiting the fact that the luminescence of this molecule is strongly de-

pendent on the environment, computational simulations of isolated 2AP and a series of 2AP–water clusters have been performed. This revealed that the excited-state lifetime of 2AP strongly depends on the number and location of water molecules [94]. Also nonadiabatic dynamics simulations, performed using the ADC(2) electronic structure method [95, 96] show that binding of a single water molecule has a dramatic effect on the excited state lifetime of adenine. In fact, electron-driven proton transfer from water to the nitrogen atom N3 of the adenine ring may be the process responsible for the observed ultrafast decay. Moreover, in Ref. [96], high-level quantum chemical calculations were performed together with experiments to show that prolonged UV-irradiation of cytidine may lead to H-C1' hydrogen atom abstraction by the carbonyl oxygen atom of cytosine. A comprehensive overview of the photophysics of the nucleobases in the gas phase and in solution is given in Ref. [97], where the effects of the solvent in modulating the followed photochemical paths have been analyzed.

Despite these illuminating works on the role of the solvent for the photorelaxation of DNA nucleobases, several questions remain open, and how aqueous solvation controls the shape of UV-VIS absorption spectra remains partially unclear. Understanding the shape of the photoabsorption spectrum and the energy ordering of the various underlying excited states is also key to the interpretation of data obtained in pump-probe experimental studies of nucleobase photorelaxation dynamics.

In order to address these questions, in the present work we report quantum chemistry calculations of the four nucleobases of DNA (adenine, thymine, cytosine and guanine) immersed in a water hydration shell and placed in aqueous solution. The nucleobase tautomers considered in this study are 7H-adenine, 9H-adenine, amino-keto cytosine, 7H-guanine, 9H-guanine, and 2,4-diketo thymine, see Fig. 4.1. We use static and time-dependent density functional theory (DFT and TDDFT) in connection with M06-2X and CAM-B3LYP functionals with the aug-cc-pVDZ basis set. By this, we calculate vertical excitation spectra and electronic density difference maps. Equipped with these, we furthermore calculate linear absorption spectra for all DNA nucleobases and compare them with the experimentally measured absorption spectra. On the basis of reasonable parameters for the contin-

uous solvent (water), no further fitting parameter enters the calculations. Apart from a systematic constant energy shift, we find a good agreement between theoretical and experimental results. A high level of realism in the calculations is ensured by including several phenomena which affect the shapes of the absorption spectra (interaction with explicit solvent molecules through hydrogen bonding, the presence of bulk solvent, tautomeric equilibria, and vibrational broadening) in the simulations. This study is the first to attempt to systematically reproduce the observed photoabsorption spectra of all four nucleobases of DNA in aqueous solution.
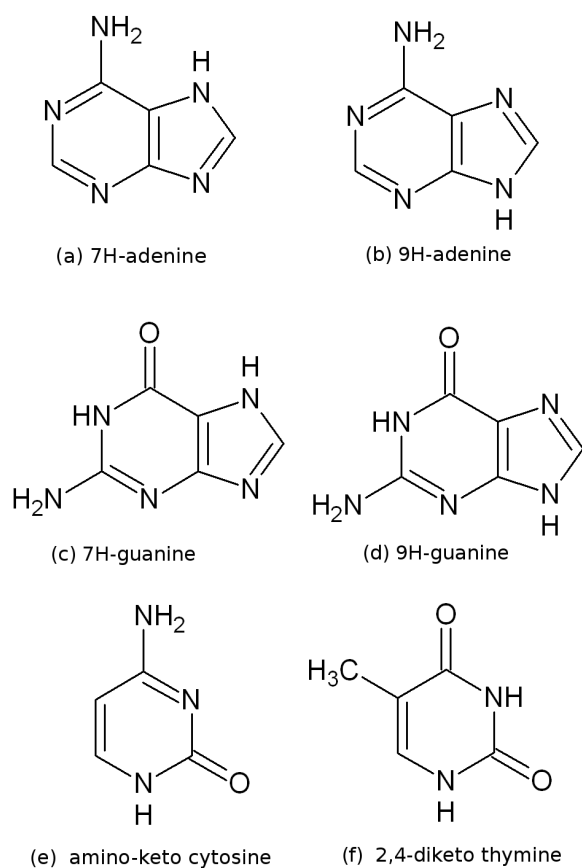

Figure 4.1: Lewis structures of the tautomers considered in this work.

4.1 Electronic structure methods

The quantum chemistry simulations were performed using the static and time-dependent density functional theory (DFT and TDDFT) methods as implemented in the computational chemistry software package Gaussian 09, Revision A.02 [61]. In particular, we have used the M06-2X and CAM-B3LYP functionals for the TDDFT calculations with the aug-cc-pVDZ basis set. These functionals have been chosen for the present study because they are known to perform reasonably well in the context of linear response TDDFT calculations for molecular clusters. In particular, they do not tend to underestimate the energies of the states involved in charge-transfer transitions, and neither do they predict spurious charge-transfer transitions to occur at low energies [62, 98, 99].

The key new ingredient in this work is the explicit inclusion of a hydration shell of water molecule around the bases. Simulations of the photoabsorption spectra in the UV-VIS range were performed for these microsolvated base molecules. For this, clusters of bases and several solvating water molecules were constructed. The solvation shell around each nucleobase molecule was constructed in such a way as to saturate all, or most, hydrogen bonding sites of the nucleobase, while using as few water molecules as possible in order to reduce the cost of the computation. For 7H- and 9H-adenine, the structure of the solvation shell was adapted from Ref. [93]. Typically, from five to eight water molecules were included in the investigated geometrical structures.

The interaction of the base molecule and the surrounding explicit water molecules with the bulk water solvent was modeled by the continuous surface charge implementation of the polarizable continuum model (CSC-PCM) [100, 101]. It was imposed both at the stage of the optimization of the molecular geometry and in the subsequent simulations of the photoabsorption spectra. Linear response solvation was applied in all TDDFT calculations of vertical excitation energies. A dielectric constant of $\varepsilon = 78.3553$ was used for the aqueous solvent. As per default, the solute cavity was constructed as a set of overlapping spheres centered at the solute atoms, using the universal force field atomic radii scaled by a factor of 1.100.

Concerning the tautomeric equilibrium state, the population of the 7H-tautomer of adenine in aqueous solution was assumed to be 22%, as determined experimentally by Cohen *et al.* [102]. In turn, the population of the 7H-tautomer of guanine in aqueous solution was taken to be 18%, as estimated by Yu *et al.* [103] on the basis of density functional theory (DFT) calculations. In the cases of cytosine and thymine, only the predominant tautomers were taken into account (which is to say, amino-keto cytosine and 2,4-diketo thymine).

The semiclassical nuclear ensemble method of Crespo-Otero and Barbatti [56] has been already described in details in Section 3.2 and has been applied to model the UV-VIS absorption spectra.

4.2 Results and discussion

4.2.1 Equilibrium geometries

Figure 4.2: Equilibrium geometry of the six investigated nucleobase tautomers optimized at the M06-2X/aug-cc-pVDZ level of theory. The lengths of hydrogen bonds are marked in units of Å.
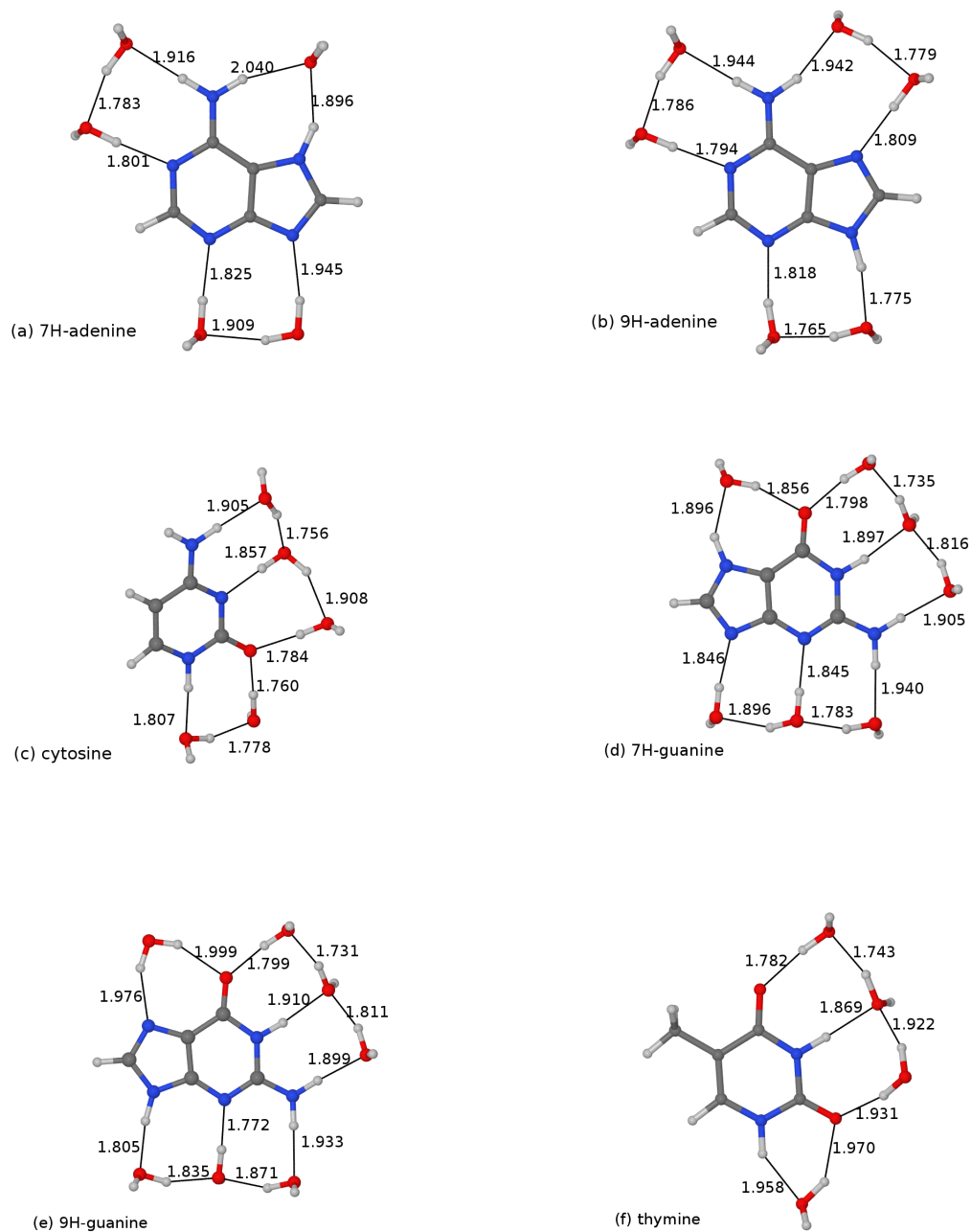

(a) 7H-adenine

(b) 9H-adenine

(c) cytosine

(d) 7H-guanine

(e) 9H-guanine

(f) thymine

Fig. 4.2 shows the optimized geometries and hydrogen bond lengths (in
Å) of the six tautomers of microsolvated bases: 7H- and 9H-adenine, cyto-
sine, 7H-keto and 9H-keto tautomers of guanine and thymine.
The O-H bonds have in general a length of approximately 1.9 Å.

4.2.2 Calculated vertical excitation spectra

Table 4.1: Vertical excitation spectra (M06-2X/aug-cc-pVDZ) for 7H-
adenine, 9H-adenine and cytosine

Tautomer	Electronic state	Gas phase		PCM solvent model		Explicit waters	
		ΔE, eV	f	ΔE, eV	f	ΔE, eV	f
7H-adenine	L_a $^1\pi\pi^*$	5.259	0.138	5.182	0.244	5.132	0.315
	L_b $^1\pi\pi^*$	5.810	0.029	5.661	0.048	5.540	0.070
	1 $^1n\pi^*$	5.057	0.008	5.415	0.004	5.805	0.001
	2 $^1n\pi^*$	5.650	0.001	5.864	0.001	6.191	0.001
	1 $^1\pi\sigma^*$	5.146	0.016	5.650	0.008	5.710	0.004
	2 $^1\pi\sigma^*$	6.053	0.002	6.304	0.013	6.231	0.001
9H-adenine	L_a $^1\pi\pi^*$	5.347	0.287	5.271	0.361	5.190	0.410
	L_b $^1\pi\pi^*$	5.523	0.014	5.476	0.027	5.395	0.040
	1 $^1n\pi^*$	5.315	0.001	5.447	0.001	5.804	$< 10^{-3}$
	2 $^1n\pi^*$	5.878	0.002	5.984	0.002	6.303	0.001
	1 $^1\pi\sigma^*$	5.452	0.007	5.594	0.007	5.658	0.004
	2 $^1\pi\sigma^*$	5.731	0.001	6.136	0.001	6.199	0.001
cytosine	1 $^1\pi\pi^*$	4.974	0.068	5.106	0.125	5.201	0.192
	2 $^1\pi\pi^*$	5.904	0.125	5.906	0.193	5.948	0.098
	1 $^1n\pi^*$	5.264	0.002	5.660	0.003	6.028	0.049
	2 $^1n\pi^*$	6.334	$< 10^{-3}$	6.137	$< 10^{-3}$	6.588	0.004
	1 $^1\pi\sigma^*$	5.495	0.004	5.926	0.005	6.130	0.004
	2 $^1\pi\sigma^*$	6.100	0.010	6.403	0.002	6.604	0.004

[a] A valence-to-valence excited state with an admixture of Rydberg character.

Vertical excitation spectra of nucleobase molecules, calculated by using
the TDDFT method at the M06-2X/aug-cc-pVDZ and CAM-B3LYP/aug-

Table 4.2: Vertical excitation spectra (M06-2X/aug-cc-pVDZ) for 7H-guanine, 9H-guanine and thymine

Tautomer	Electronic state	Gas phase		PCM solvent model		Explicit waters	
		ΔE, eV	f	ΔE, eV	f	ΔE, eV	f
7H-guanine	L_a $^1\pi\pi^*$	4.958	0.132	4.870	0.183	4.684	0.203
	L_b $^1\pi\pi^*$	5.793	0.181	5.373	0.001	5.675	0.297
	1 $^1n\pi^*$	5.362	$< 10^{-3}$	5.511	$< 10^{-3}$	5.870	$< 10^{-3}$
	2 $^1n\pi^*$	6.137	0.001	6.363	0.001	6.510	0.004
	1 $^1\pi\sigma^*$	5.180	0.006	5.738	0.255	5.364	0.002
	2 $^1\pi\sigma^*$	5.454	0.009	5.825	0.037	5.941	0.005
9H-guanine	L_a $^1\pi\pi^*$	5.162	0.136	5.076	0.174	4.921	0.200
	L_b $^1\pi\pi^*$	5.588	0.318	5.490	0.457	5.487	5.486
	1 $^1n\pi^*$	5.376	0.002	5.595	$< 10^{-3}$	5.836	$< 10^{-3}$
	2 $^1n\pi^*$	6.276	0.005	6.412	0.001	6.488	0.002
	1 $^1\pi\sigma^*$	4.987	0.016	5.287	$< 10^{-3}$	5.289	0.004
	2 $^1\pi\sigma^*$	5.339	0.010	5.812	0.011	5.889	0.001
thymine	1 $^1\pi\pi^*$	5.246	0.179	5.156	0.232	5.124	0.239
	2 $^1\pi\pi^*$	6.610	0.108	6.450	0.250	6.310	0.267
	1 $^1n\pi^*$	4.971	$< 10^{-3}$	5.178	$< 10^{-3}$	5.371	$< 10^{-3}$
	2 $^1n\pi^*$	6.251	$< 10^{-3}$	6.402	$< 10^{-3}$	6.605	0.001
	1 $^1\pi\sigma^*$	5.633	0.001	5.948	0.001	6.076	0.002
	2 $^1\pi\sigma^*$	6.373	0.001	6.497	0.001	6.631	0.002

[a] A valence-to-valence excited state with an admixture of Rydberg character.

cc-pVDZ levels of theory, are characterized in Tables 4.1, 4.2, 4.3 and 4.4. Vertical excitation energies (ΔE) and associated oscillator strengths (f) into the low-lying singlet excited states of the six investigated nucleobase tautomers at their ground-state equilibrium (S_0-min) geometries are listed. Different microenvironments were imposed in the calculations of the vertical excitation spectra: the gas phase, aqueous solvation represented using both explicit water molecules and the PCM solvation model, and aqueous solvation represented by only the PCM solvation model. The $\pi\pi^*$ states are labeled as L_a and L_b according to the formalism described in Ref. [16], and

Table 4.3: Vertical excitation spectra (CAM-B3LYP/aug-cc-pVDZ) for 7H-adenine, 9H-adenine and cytosine

Tautomer	Electronic state	Gas phase		PCM solvent model		Explicit waters	
		ΔE, eV	f	ΔE, eV	f	ΔE, eV	f
7H-adenine	L_a $^1\pi\pi^*$	5.191	0.077	5.133	0.227	5.103	0.292
	L_b $^1\pi\pi^*$	5.734	0.031	5.598	0.053	5.497	0.077
	1 $^1n\pi^*$	5.129	0.046	5.504	0.003	5.872	0.001
	2 $^1n\pi^*$	5.658	0.002	5.913	0.001	6.241	$< 10^{-3}$
	1 $^1\pi\sigma^*$	5.236	0.033	5.771	0.009	5.904	0.006
	2 $^1\pi\sigma^*$	6.166	0.002	6.473	0.002	6.429	0.001
9H-adenine	L_a $^1\pi\pi^*$	5.316	0.278	5.246	0.349	5.182	0.402
	L_b $^1\pi\pi^*$	5.459	0.012	5.416	0.025	5.341	0.037
	1 $^1n\pi^*$	5.339	0.001	5.491	0.001	5.867	$< 10^{-3}$
	2 $^1n\pi^*$	5.916	0.001	6.044	0.002	6.372	0.001
	1 $^1\pi\sigma^*$	5.629	0.010	5.764	0.010	5.879	0.005
	2 $^1\pi\sigma^*$	5.945	0.003	6.330	0.001	6.427	0.039
cytosine	1 $^1\pi\pi^*$	4.936	0.064	5.085	0.117	5.196	0.183
	2 $^1\pi\pi^*$	5.870	0.122	5.89	0.190	5.960	0.130
	1 $^1n\pi^*$	5.281	0.002	5.695	0.003	6.062	0.025
	2 $^1n\pi^*$	5.862	$< 10^{-3}$	6.255	$< 10^{-3}$	6.713	0.030
	1 $^1\pi\sigma^*$	5.621	0.005	6.058	0.006	6.296	0.006
	2 $^1\pi\sigma^*$	6.130	0.003	6.506	0.003	6.752	0.019

[a] A valence-to-valence excited state with an admixture of Rydberg character.

in agreement with the results presented in Refs. [104], [105].

As the simulated photoabsorption spectra of nucleobases in aqueous solution will be dominated by excitations into the bright excited states of the majority tautomers, it is of interest to assess the accuracy of the TDDFT method in combination with the M06-2X and CAM-B3LYP functionals for the vertical excitations of these states. In order to take advantage of the most accurate theoretical benchmarks available, the subject of this assessment must be the vertical excitation spectra of the isolated molecules. The study of Szalay and coworkers [106], which employed coupled cluster meth-

Table 4.4: Vertical excitation spectra (CAM-B3LYP/aug-cc-pVDZ) for 7H-guanine, 9H-guanine and thymine

Tautomer	Electronic state	Gas phase		PCM solvent model		Explicit waters	
		ΔE, eV	f	ΔE, eV	f	ΔE, eV	f
7H-guanine	L_a $^1\pi\pi^*$	4.887	0.132	4.802	0.182	4.646	0.201
	L_b $^1\pi\pi^*$	5.759 [a]	0.150	5.720	0.248	6.271	0.382
	1 $^1n\pi^*$	5.440	$< 10^{-3}$	5.608	$< 10^{-3}$	5.970	$< 10^{-3}$
	2 $^1n\pi^*$	6.039	$< 10^{-3}$	6.278	0.001	6.455	0.002
	1 $^1\pi\sigma^*$	5.292	0.006	5.523	0.001	5.607	0.010
	2 $^1\pi\sigma^*$	5.601	0.016	5.960	0.010	5.690	0.254
9H-guanine	L_a $^1\pi\pi^*$	5.072	0.117	5.015	0.173	4.880	0.197
	L_b $^1\pi\pi^*$	5.559	0.273	5.464	0.440	5.484	0.373
	1 $^1n\pi^*$	5.526	0.012	5.741	$< 10^{-3}$	5.976	$< 10^{-3}$
	2 $^1n\pi^*$	6.324	0.002	6.422	0.002	6.485	0.003
	1 $^1\pi\sigma^*$	5.164	0.037	5.452	0.007	5.542	0.055
	2 $^1\pi\sigma^*$	5.508	0.044	5.974	0.011	6.140	0.001
thymine	1 $^1\pi\pi^*$	5.208	0.174	5.122	0.227	5.088	0.234
	2 $^1\pi\pi^*$	6.581	0.046	6.432	0.261	6.293	0.272
	1 $^1n\pi^*$	5.082	$< 10^{-3}$	5.301	$< 10^{-3}$	5.501	$< 10^{-3}$
	2 $^1n\pi^*$	6.366	$< 10^{-3}$	6.517	$< 10^{-3}$	6.724	0.002
	1 $^1\pi\sigma^*$	5.775	0.001	6.110	0.001	6.271	0.002
	2 $^1\pi\sigma^*$	6.541	$< 10^{-3}$	6.661	0.001	6.834	0.003

[a] A valence-to-valence excited state with an admixture of Rydberg character.

ods, is the theoretically most advanced calculation of the vertical excitation spectra performed to date, and so we use it as a benchmark against which to compare the results of the TDDFT calculations. In Table 4.5, we compare the vertical excitation energies oscillator strengths of the bright excited states of nucleobases obtained from the TDDFT calculations with the values reported in the work just cited. (For our purposes, excited states characterized by values of the oscillator strength greater than 0.05 were considered to be bright.)

It can be seen from Table 4.5 that the TDDFT calculations in combi-

	M06-2X/aug-cc-pVDZ		
Nucleobase	Excited state	ΔE, eV	f
9H-adenine	L_a $\pi\pi^*$	5.348	0.2867
cytosine	$\pi\pi^*$	4.974	0.0687
9H-guanine	L_a $\pi\pi^*$	5.163	0.1356
	L_b $\pi\pi^*$	5.589	0.3174
Thymine	$\pi\pi^*$	5.246	0.1793
	CAM-B3LYP/aug-cc-pVDZ		
Nucleobase	Excited state	ΔE, eV	f
9H-adenine	L_a $\pi\pi^*$	5.316	0.2783
cytosine	$\pi\pi^*$	4.936	0.0635
9H-guanine	L_a $\pi\pi^*$	5.072	0.1164
	L_b $\pi\pi^*$	5.559	0.2729
Thymine	$\pi\pi^*$	5.207	0.1744
	EOMEE-CCSD(T)/aug-cc-pVTZ		
Nucleobase	Excited state	ΔE, eV	f^a
9H-adenine	L_a $\pi\pi^*$	5.23	0.275
cytosine	$\pi\pi^*$	4.69	0.066
9H-guanine	L_a $\pi\pi^*$	4.86	0.160
	L_b $\pi\pi^*$	5.37	0.366
Thymine	$\pi\pi^*$	5.15	0.213

[a] The values of the oscillator strength are taken from calculations at the EOMEE-CCSD/aug-cc-pVTZ level of theory.

Table 4.5: Comparison of vertical excitation spectra of the isolated nucleobase molecules calculated using the TDDFT method with the use of the M06-2X and CAM-B3LYP functionals with the benchmark provided by the EOMEE-CCSD(T) method [106].

nation with either functional systematically overestimate the vertical excitation energies into the bright excited states of nucleobases by up to around 0.3 eV, in comparison to the benchmark provided by the method

of the equation of motion excitation energy coupled-cluster with perturbative triple excitations (EOMEE-CCSD(T)). The exception is thymine, for which the excitation energies calculated with TDDFT coincide closely with those obtained at the EOMEE-CCSD(T) level. Therefore, insofar as the EOMEE-CCSD(T) level of theory can be considered a realistic benchmark for vertical excitation energies, and assuming this systematic blue shift is not compensated for by another source of error, we may expect that the photoabsorption spectra of nucleobases in aqueous solution simulated with the use of TDDFT, with the M06-2X or the CAM-B3LYP functional, will exhibit a blue shift of a few tenths of an electronvolt relative to experiment.

Inspection of the data in Tables 4.1-4.4 reveals that aqueous solvation has a strong influence on the vertical excitation spectra. Across all nucleobase molecules considered presently, the participation of the lone electron pairs in hydrogen bonding with explicit solvating water molecules increases the vertical excitation energies into the $n\pi^*$-type excited states by a few tenths of an electronvolt. Meanwhile, the excitation energies into the lowest $\pi\pi^*$-type states are shifted downwards by up to around 0.3 eV. The exception is cytosine, in which the inclusion of explicit solvent molecules and continuum bulk solvent has the effect of increasing the excitation energy of the lowest $\pi\pi^*$ state by roughly 0.2 eV, according to both the M06-2X and CAM-B3LYP functionals. As a consequence, for each of the microsolvated nucleobase molecules in continuum aqueous solvent (including cytosine), the lowest vertical excitation is into a $\pi\pi^*$-type state, which is energetically separated from the lowest $n\pi^*$- and Rydberg-type excited states.

This is in contrast to the cases of nucleobases in the gas phase, and with continuum solvation without the use of explicit solvent molecules, where the energies of the lowest $n\pi^*$- and $\pi\pi^*$-type states are comparable.

Moreover, for all six nucleobase tautomers, aqueous solvation also has the effect of shifting upwards by a few tenths of an electronovolt the excitation energies into the lowest Rydberg-type ($\pi\sigma^*$) excited states. This is true whether the solvent is modeled using only the CSC-PCM model, or the CSC-PCM model in combination with explicit water molecules.
The phenomenon whereby the excitation energies into the Rydberg-type states of a chromophore are increased by the presence of explicit solvent

molecules, or substituents bonded to the chromophore, was apparently first considered by Szalay and coworkers [107], who attributed it to the spatial overlap between the Rydberg-type orbitals of the chromophore and the orbitals of the nearby chemical moieties. As seen in Tables 4.1-4.4, the Rydberg-type excited states are also destabilized by interaction with an implicitly included environment alone, although due to their abstracted nature, the CSC-PCM model provides only a very simplistic description of the interaction of the Rydberg-type states with the surroundings of the chromophore. The treatment of the Rydberg-type states could in principle be improved through the further build-up of the explicit solvation shell, but this approach is unattractive because the simulation cost increases rapidly with system size.

We note that for the purposes of the present study, however, a highly realistic description of the Rydberg-type excited states is not essential. This is because, in the absence of mixing with valence-to-valence excited states, the oscillator strengths of the Rydberg-type excited states are typically of the order of 0.005, much lower than the oscillator strengths of the low-lying bright $\pi\pi^*$-type states, which are in the range of roughly 0.2 to 0.4. It follows that, according to Eq. 3.13, as long as the number of Rydberg-type excited states found near the low-lying $\pi\pi^*$-type states is low, the magnitude of the relative error in the calculated photoabsorption coefficient due to the simplified treatment of the Rydberg-type excited states is therefore unlikely to exceed $0.005/0.2 = 2.5\%$.

Electron density difference maps (EDDMs)

(a) S_1 (L_a $\pi\pi^*$)

(b) S_2 (L_b $\pi\pi^*$)

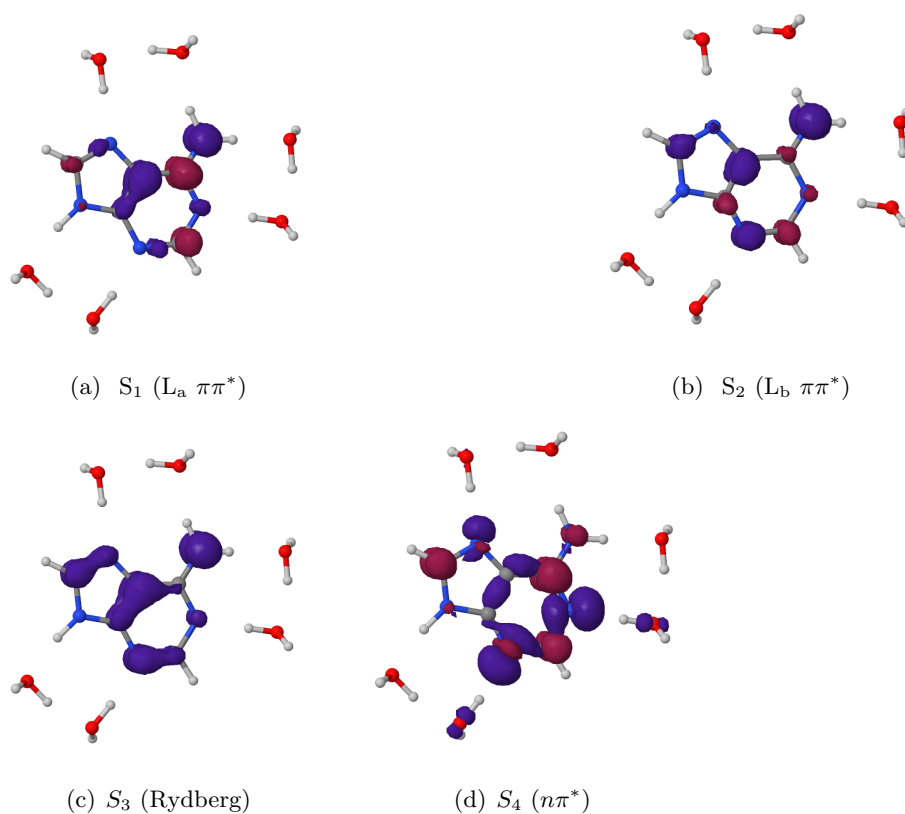(c) S_3 (Rydberg)

(d) S_4 ($n\pi^*$)
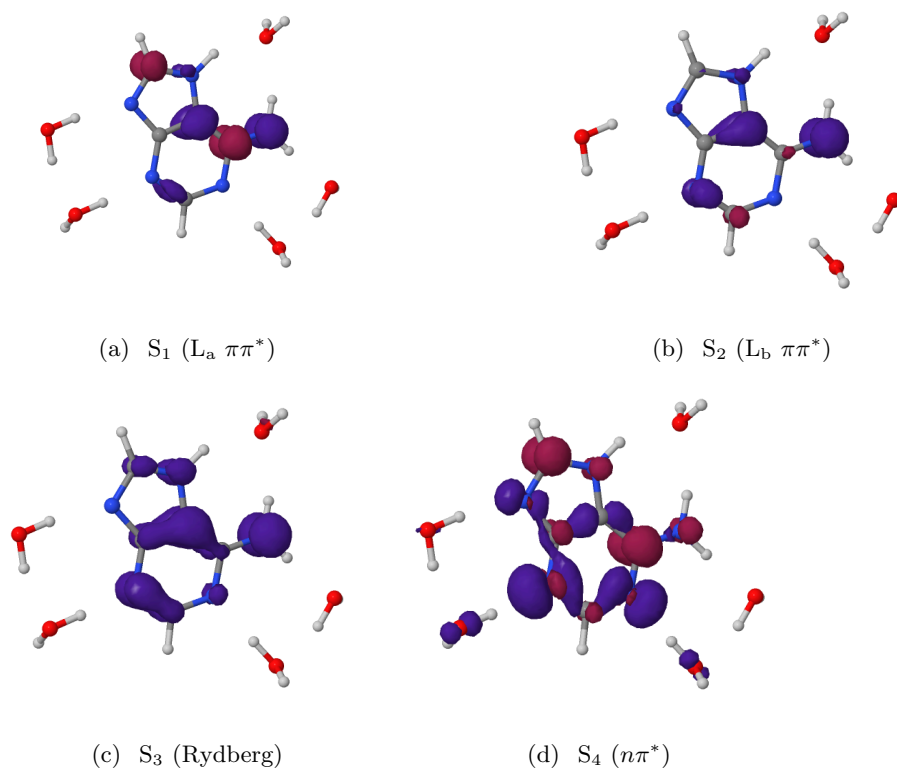
Figure 4.3: EDDMs calculated for the lowest excited states of microsolvated 7H-adenine, calculated at the M06-2X/aug-cc-pVDZ level of theory, and plotted in 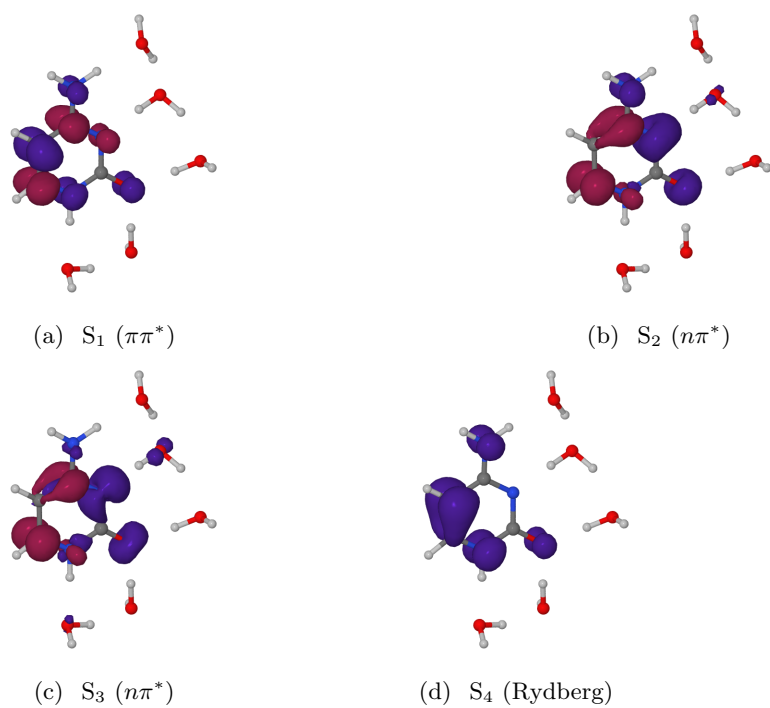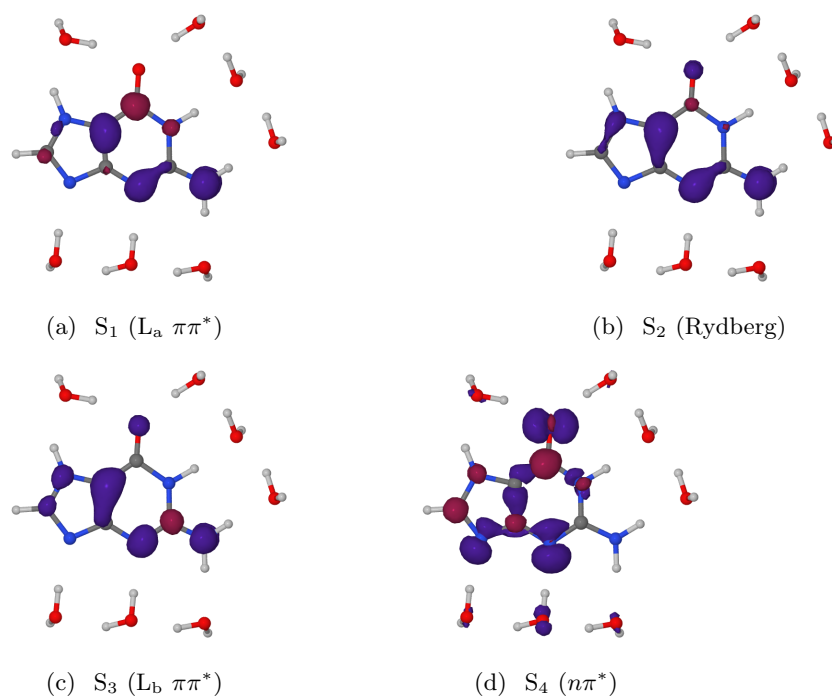the fo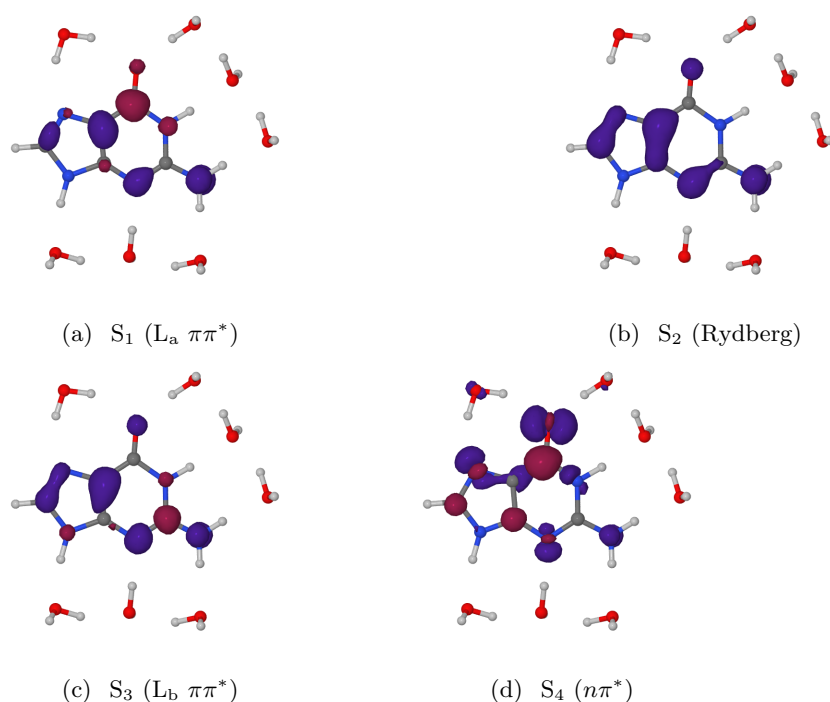rm of isosurfaces with isovalues of ± 0.005 $e/a_0{}^3$. For each excited state, the red and blue isosurfaces delimit regions in which the electron density is increased and decreased, respectively, relative to the singlet ground state.

Electron density difference maps (EDDMs) have been derived for the six investigated nucleobase tautomers: 7H- and 9H-adenine, cytosine, 7H- and 9H-keto guanine and thymine. They represent the difference of the electron density of the excited state and the one of the ground state for a given molecular geometry, and they are useful to visualize the nature of an excited electronic state and the orbitals involved in the observed transitions. In

Figs. 4.3-4.8, EDDMs are shown for all the investigated molecules. EDDMs are plotted in the form of isosurfaces with isovalues of ± 0.005 $e/a_0{}^3$. For each excited state, the red and blue isosurfaces delimit regions in which the electron density is increased and decreased, respectively, relative to the singlet ground state.

(a) S_1 (L_a $\pi\pi^*$)

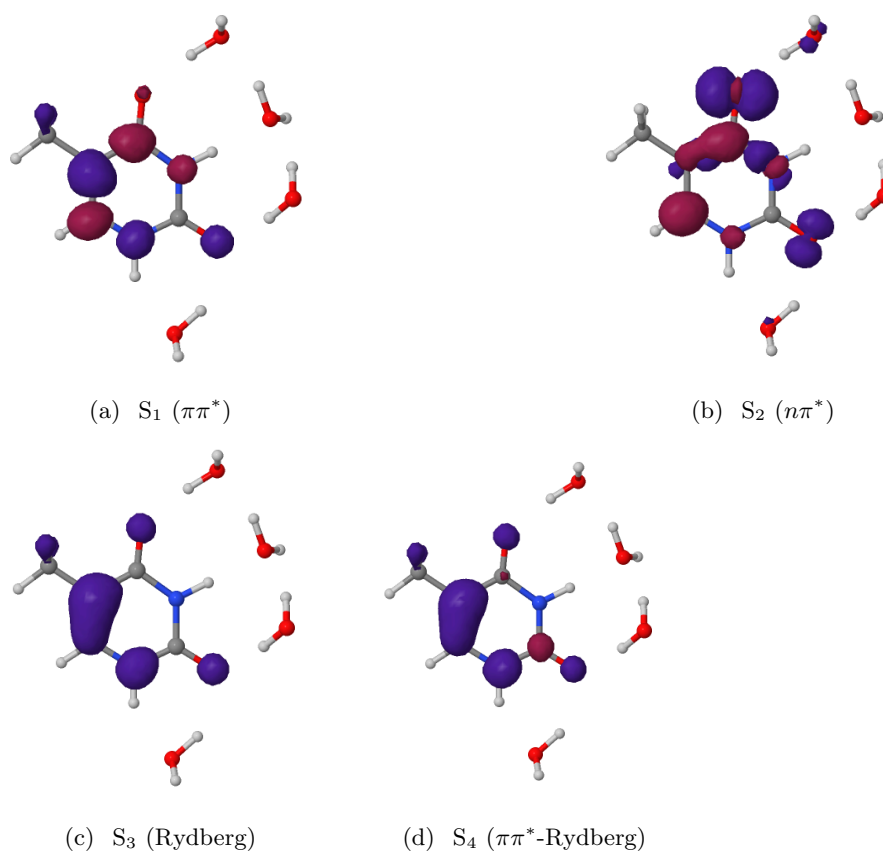(b) S_2 (L_b $\pi\pi^*$)

(c) S_3 (Rydberg)

(d) S_4 ($n\pi^*$)

Figure 4.4: EDDMs calculated for the lowest excited states of microsolvated 9H-adenine, calculated at the M06-2X/aug-cc-pVDZ level of theory, and plotted in the form of isosurfaces with isovalues of ± 0.005 $e/a_0{}^3$.

(a) S_1 $(\pi\pi^*)$

(b) S_2 $(n\pi^*)$

(c) S_3 $(n\pi^*)$

(d) S_4 (Rydberg)

Figure 4.5: EDDMs calculated for the lowest excited states of microsolvated cytosine, calculated at the M06-2X/aug-cc-pVDZ level of theory, and plotted in the form of isosurfaces with isovalues of ± 0.005 $e/a_0{}^3$.

(a) S$_1$ (L$_a$ $\pi\pi^*$)

(b) S$_2$ (Rydberg)

(c) S$_3$ (L$_b$ $\pi\pi^*$)

(d) S$_4$ ($n\pi^*$)

Figure 4.6: EDDMs calculated for the lowest excited states of microsolvated $7H-$keto guanine, calculated at the M06-2X/aug-cc-pVDZ level of theory, and plotted in the form of isosurfaces with isovalues of ±0.005 $e/a_0{}^3$.

(a) S$_1$ (L$_a$ $\pi\pi^*$)

(b) S$_2$ (Rydberg)

(c) S$_3$ (L$_b$ $\pi\pi^*$)

(d) S$_4$ ($n\pi^*$)

Figure 4.7: EDDMs calculated for the lowest excited states of microsolvated 9H-keto guanine, calculated at the M06-2X/aug-cc-pVDZ level of theory, and plotted in the form of isosurfaces with isovalues of ±0.005 $e/a_0{}^3$.

4.2.3 Linear photoabsorption spectra

On the basis of the calculated vertical excitation spectra, we have calculated the linear photoabsorption spectra and compared them to the experimentally measured data. The results are shown in Figs. 4.9-4.11 with the spectra simulated at the M06-2X/aug-cc-pVDZ and CAM-B3LYP/aug-cc-pVDZ levels of theory.

The experimental spectra were obtained at the Max Planck Institute for the Structure and Dynamics of Matter (Hamburg) in the Coherent Control and Multidimensional Spectroscopy group by Alessandra Picchiotti and Dr. Valentyn Prokhorenko (the text of the following paragraph was provided by Alessandra Picchiotti, Max Planck Institute for the Structure and Dynamics

(a) S_1 ($\pi\pi^*$)

(b) S_2 ($n\pi^*$)

(c) S_3 (Rydberg)

(d) S_4 ($\pi\pi^*$-Rydberg)

Figure 4.8: EDDMs calculated for the lowest excited states of microsolvated thymine, calculated at the M06-2X/aug-cc-pVDZ level of theory, and plotted in the form of isosurfaces with isovalues of ± 0.005 $e/a_0{}^3$.

of Matter Hamburg). The data were obtained using a Shimadzu UV 2600 spectrometer [80]. Each scan was performed with a sensitivity of 0.5 nm and a time-per-point accumulation equal to 2 s. Moreover, Hellma quartz cuvettes with a path length of 0.1 cm were used. All the samples were purchased from Sigma Aldrich and Santa Cruz in powder and used without further purification. They were dissolved in desalted and doubly distilled water, then filtered with 0.2 μm syringe filters. The solute concentrations were adjusted to give a maximal absorbance between 0.5 and 1 at the peak near 260 nm. The solution pH was monitored and was always close to 7. The spectra were recorded in the range of 400 to 220 nm.

Looking at Figs. 4.9-4.11, it can be seen that the vibrational broadening

shifts the simulated spectra to the red relative to the vertical excitation spectrum calculated for the ground-state equilibrium geometry. We note that both for 7H-adenine and 9H-adenine, and for 7H-guanine and 9H-guanine, a weighted sum of the spectra is shown in order to obtain a more realistic absorption spectrum containing both tautomers.

In general, the form of the experimental spectra in the low-energy regime is well reproduced by the simulations. All calculated spectra are blue-shifted relative to the experimental data by approximately 0.3 eV. The systematic shifts of the peaks of the two lowest bands between the experimental and simulated spectra are collected in Tables 4.6 and 4.7, together with the relative error of the photoabsorption cross section. This quantity has been determined according to the relation (see Fig. 4.12 for a graphical explanation)

$$\frac{\Delta\sigma}{\sigma} = \frac{\sigma_{max}^{calc} - \sigma_{max}^{obs}}{\sigma_{max}^{obs}} \,. \tag{4.1}$$

In the case of cytosine, the second peak in the experimental spectrum is outside the range of 3.50 to 6.20 eV in which the data were collected. For this reason, we could not analyze the corresponding error in the position and intensity of the second peak in this case.

The chosen basis set aug-cc-pVDZ is moderately large, but from a computational point of view, an even larger basis could be chosen. Therefore, to investigate the effect of using a larger one, we have also used the basis set aug-cc-pVTZ. The importance of this effect is estimated by re-optimizing the geometries of the six nucleobase-water clusters at the M06-2X/aug-cc-pVTZ and CAM-B3LYP/aug-cc-pVTZ levels of theory, and then re-calculating their vertical excitation spectra for the resulting geometries. The comparison between the stick spectra calculated by using aug-cc-pVDZ and aug-cc-pVTZ is presented in Figs. 4.13 and 4.14, where the stick spectra of the two levels of theory are superposed.

Somewhat counter-intuitively, the vertical excitation energies for the low-lying bright states generally increase slightly when the calculation is repeated with the larger aug-cc-pVTZ basis set at the re-optimized energy. In fact, it would be normally expected that the blue shift is reduced and the excitation
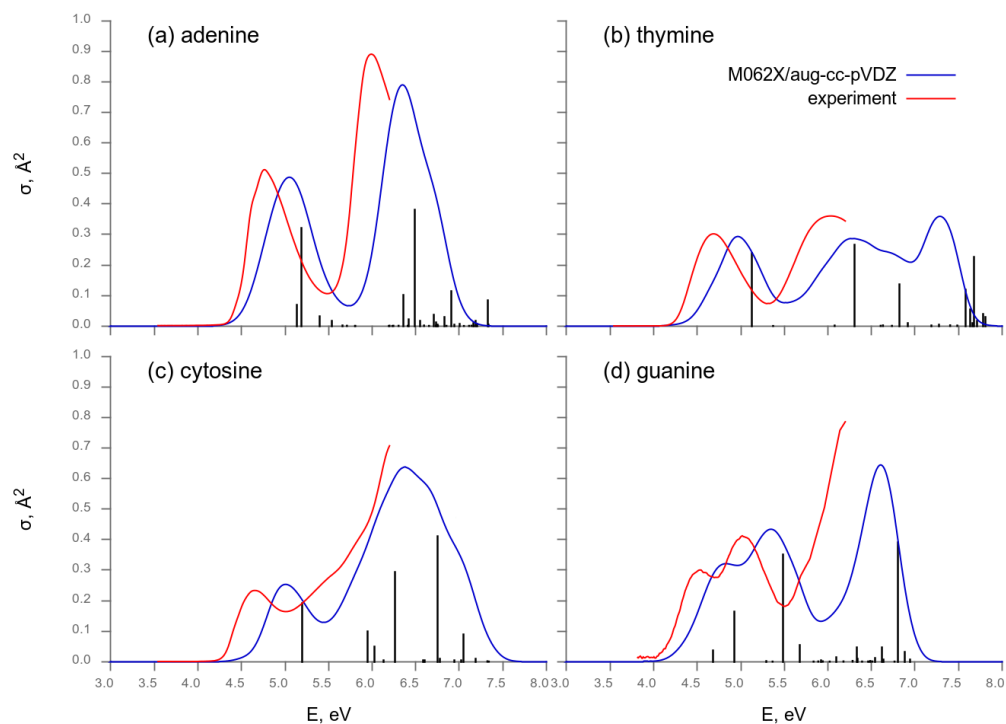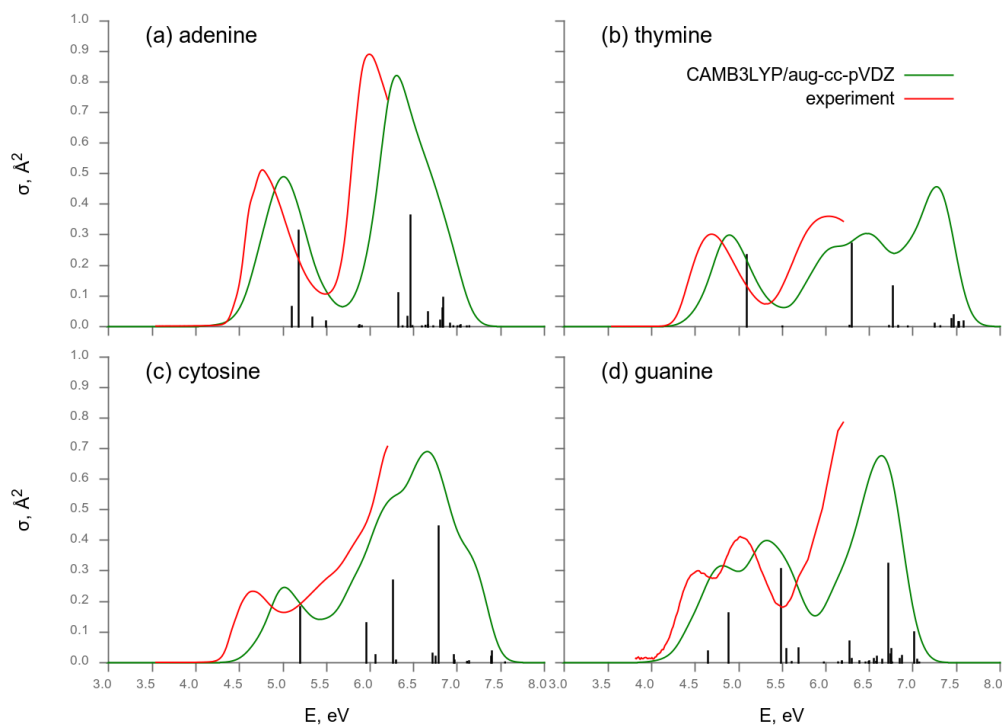
Figure 4.9: Simulated absorption spectra of nucleobases in aqueous solution, computed at the M06-2X/aug-cc-pVDZ level of theory, compared to the experimentally observed (experimental data by courtesy of Alessandra Picchiotti, Max Planck Institute for the Structure and Dynamics of Matter Hamburg) spectra. The black columns indicate the vertical excitation energies evaluated at the ground-state equilibrium geometry, and their relative heights are proportional to the corresponding oscillator strengths. In the case of adenine and guanine, the spectra are averaged over the 7H- and 9H- tautomers of both bases according to their populations, and the column heights are also scaled proportionally to the respective populations.

Figure 4.10: Simulated absorption spectra of nucleobases in aqueous solution, computed at the CAMB3LYP/aug-cc-pVDZ level of theory, compared to the experimentally observed (experimental data by courtesy of Alessandra Picchiotti, Max Planck Institute for the Structure and Dynamics of Matter Hamburg) spectra. The black columns indicate the vertical excitation energies evaluated at the ground-state equilibrium geometry, and their relative heights are proportional to the corresponding oscillator strengths. In the case of adenine and guanine, the spectra are averaged over the 7H- and 9H- tautomers of both bases according to their populations, and the column heights are also scaled proportionally to the respective populations.
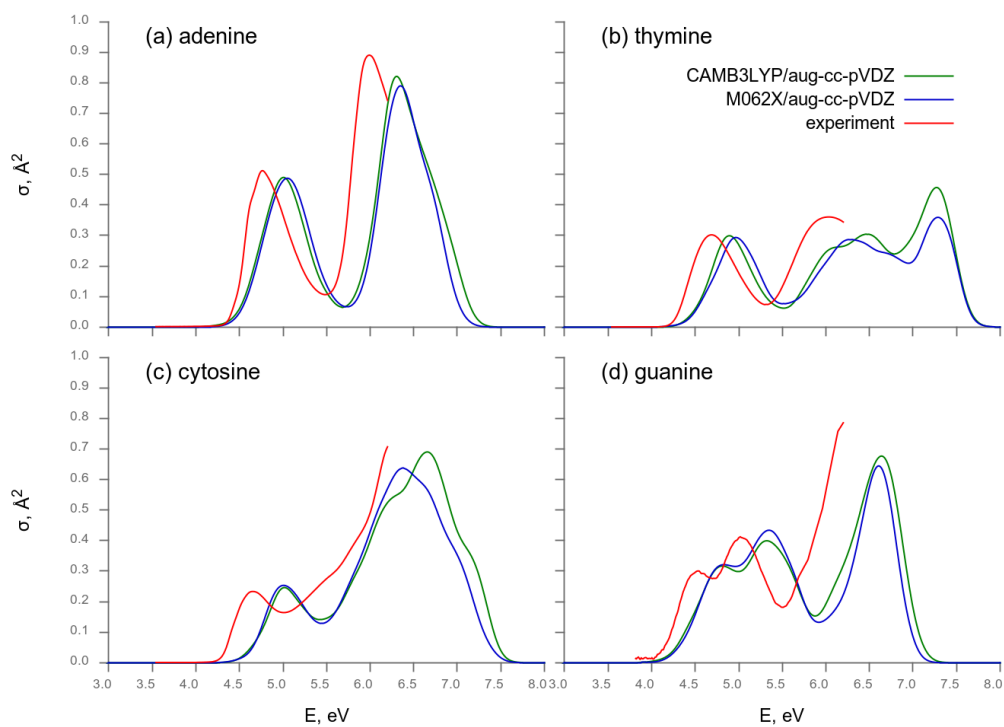
Figure 4.11: Comparison of photoabsorption spectra for the four DNA nucle-obases simulated using the M06-2X and the CAM-B3LYP functionals with the experimentally observed (experimental data by courtesy of Alessandra Picchiotti, Max Planck Institute for the Structure and Dynamics of Matter Hamburg) spectra.
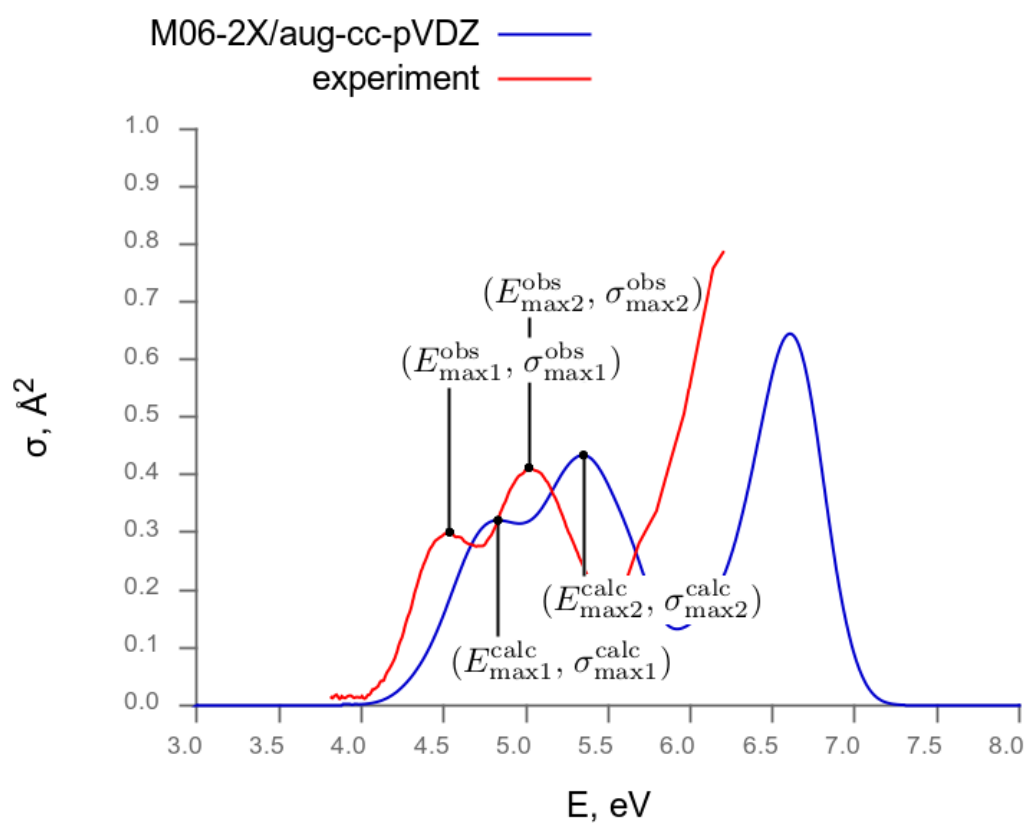
Figure 4.12: Graphical explanation of calculation of values in Tabs. 4.6 and 4.7.

Nucleobase	$E_{\max1}^{\mathrm{calc}}$, eV	shift in $E_{\max1}^{\mathrm{calc}}$, eV	$\Delta\sigma/\sigma$ at max1
adenine	5.050	0.291	−0.0481
cytosine	5.010	0.358	0.0855
guanine	4.830	0.304	0.0678
thymine	4.970	0.283	−0.0286
Nucleobase	$E_{\max2}^{\mathrm{calc}}$, eV	shift in $E_{\max2}^{\mathrm{calc}}$, eV	$\Delta\sigma/\sigma$ at max2
adenine	6.350	0.360	−0.113
cytosine			
guanine	5.350	0.332	0.052
thymine	6.280	0.247	−0.204

Table 4.6: Systematic shifts of the peaks and relative errors of the photoabsorption cross section of the lowest (max1) and the second lowest (max2) band between experimental and simulated spectra for the four DNA nucleobases, from calculations performed using the M06-2X functional.

Nucleobase	$E_{\max1}^{\mathrm{calc}}$, eV	shift in $E_{\max1}^{\mathrm{calc}}$, eV	$\Delta\sigma/\sigma$ at max1
adenine	5.010	0.251	−0.043
cytosine	5.020	0.368	0.0549
guanine	4.810	0.274	0.054
thymine	4.890	0.203	−0.009
Nucleobase	$E_{\max2}^{\mathrm{calc}}$, eV	shift in $E_{\max2}^{\mathrm{calc}}$, eV	$\Delta\sigma/\sigma$ at max2
adenine	6.300	0.310	−0.071
cytosine			
guanine	5.320	0.302	−0.032
thymine	6.470	0.438	−0.156

Table 4.7: Same as Table 4.4, but using the CAM-B3LYP functional.
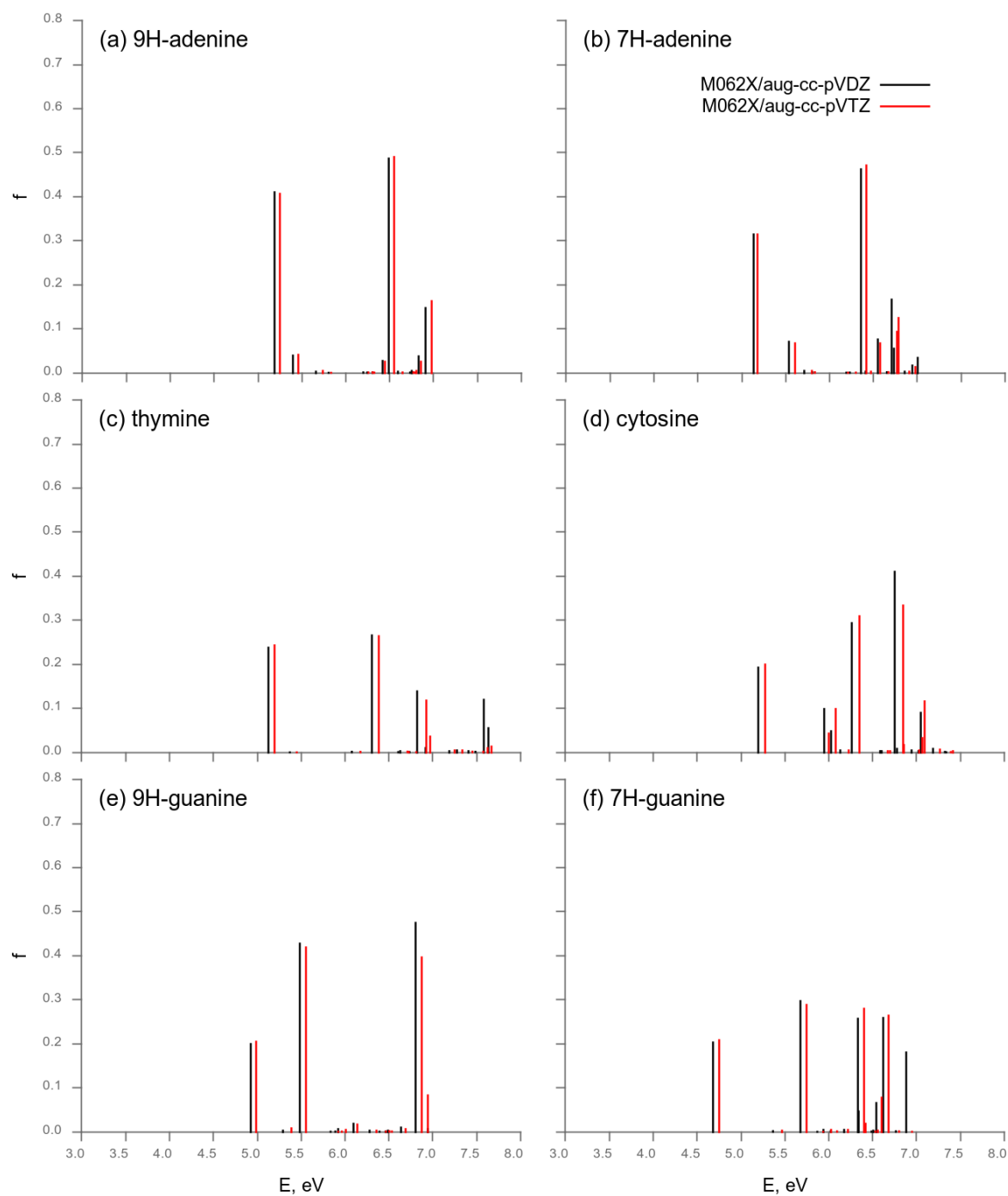
Figure 4.13: Simulated stick spectra for the six DNA nucleobases tautomers derived from the M06-2X calculation: comparison between results obtained by using the aug-cc-pVDZ (black) and aug-cc-pVTZ (red) basis sets.
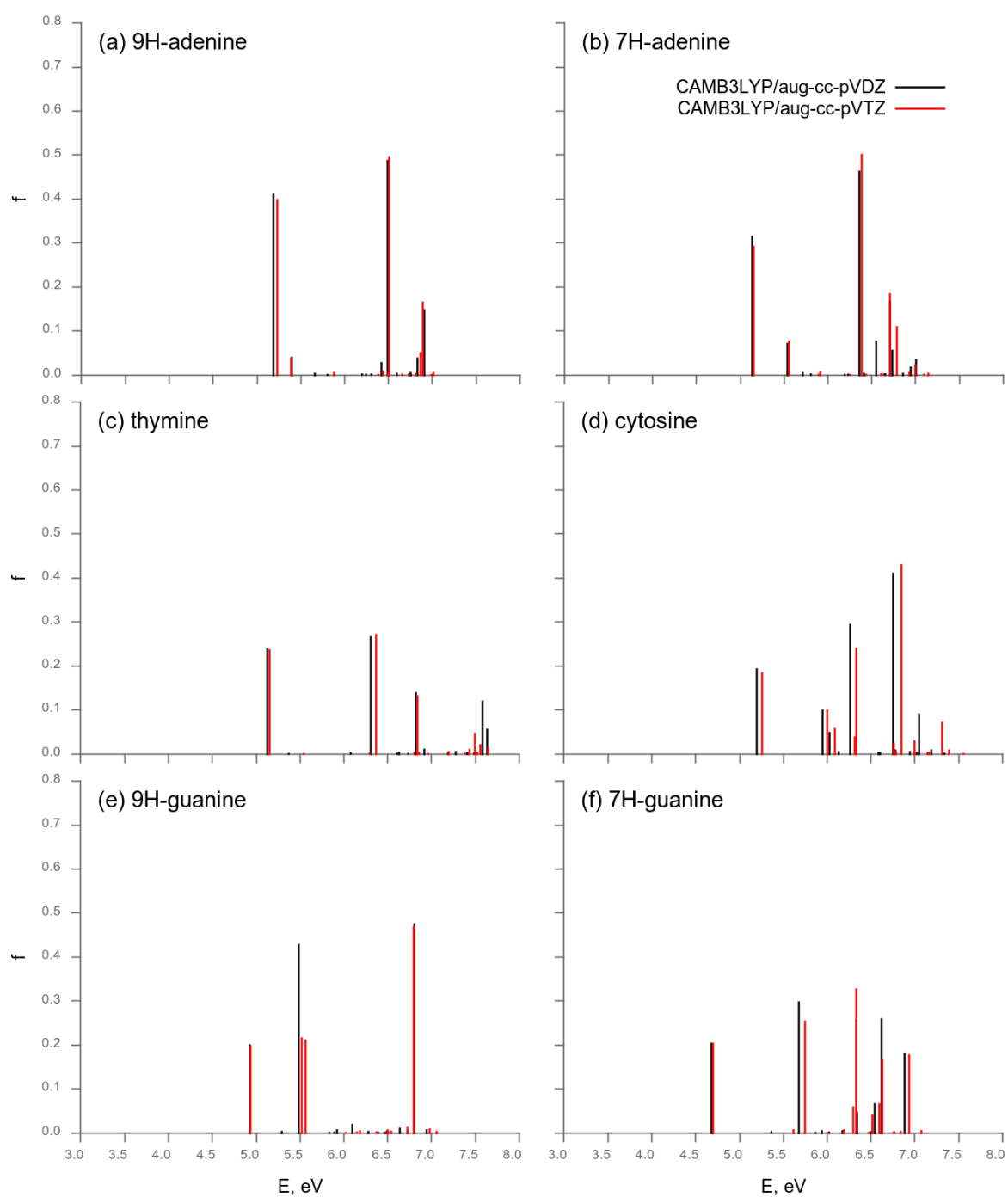
Figure 4.14: Simulated stick spectra for the six DNA nucleobases tautomers derived from CAM-B3LYP calculation: comparison between results obtained by using the aug-cc-pVDZ (black) and aug-cc-pVTZ (red) basis sets.

energies decrease with increasing the basis set size. Yet, we find that the vertical excitation energy to the lower bright state are only slightly affected by enlarging the basis set.

In general, the spectra of the four nucleobases are composed of two clearly visible bands, separated by a low intensity region. In the case of adenine and thymine, each of these bands is due to a single bright $\pi\pi^*$ transition. For guanine, four $\pi\pi^*$ states contribute to the lowest photoabsorption band, i.e., the excitations into the lowest two $\pi\pi^*$ states arise (the L_a and L_b states of each tautomer). This may be related to multiple decay pathways which can be identified in the molecule after UV absorption [57].

Regarding cytosine, there has been a debate in previous studies as to how many bright excited states give significant contributions to the photoabsorption spectrum. On the basis of the linear vibronic coupling method and on the equations-of-motion coupled cluster with single and double excitations (EOM-CCSD) level of electronic structure theory, Tajti *et al.* [108] have performed spectral simulations for cytosine in the gas phase. They have interpreted the resulting photoabsorption spectrum up to around 60000 cm^{-1} (7.4 eV) as arising mainly from transitions to only two $\pi\pi^*$-type states. Subsequently, Barbatti and coworkers [57] have demonstrated that a third $\pi\pi^*$-type state must be taken into account in order to explain the appearance of the gas-phase spectrum. The present results for microsolvated cytosine in a bulk solvent indicate that in aqueous solution the number of excited electronic states which significantly contribute to the photoabsorption spectrum is even higher. This is due to a mixing of $\pi\pi^*$ and $n\pi^*$ states. This is further supported by the the EDDMs of the low-lying excited electronic states of microsolvated cytosine calculated at the M06-2X/aug-cc-pVDZ level at the ground-state equilibrium geometry, which are shown in Fig. 4.5. The S_2 and S_3 states are both nominally $n\pi^*$ in character, but also involve a substantial redistribution of the π-type electron density. These $n\pi^*$ states have a sizable admixture of $\pi\pi^*$ character which is reflected by their moderately large oscillator strengths (0.098 and 0.049, respectively, for S_2 and S_3). The contribution of these $n\pi^*$ states to the photoabsorption spectrum is mainly significant in the interband region around 5.5 eV in the simulated spectrum. This feature may trigger different deactivation pathways right

after the photoabsorption [57].

Cytosine has the largest shift between the experimental and calculated spectra for both the functionals M06-2X and CAM-B3LYP. The peak in the simulated spectra is in the valley of the experimental spectrum, see Figs. 4.9-4.11. The effect of the explicit inclusion of the water molecules forming the hydration shell seems to play a quite important role in particular for cytosine. To study this in more detail, we have simulated the photoabsorption spectra of cytosine with the polarizable continuum model but without explicitly including the water molecules of the hydration shell, at the CAM-B3LYP/aug-cc-pVDZ and M06-2X/aug-cc-pVDZ levels of theory. The results for the photoabsorption spectra are shown in Fig. 4.15. The general form of these spectra in the presence of a bulk solvent only is similar to that when explicit water molecules are additionally included, but, importantly, the intensity of the first absorption band is significantly underestimated with respect to the experiment. Hence, this indicates that at least for cytosine, the inclusion of explicit solvent molecules is mandatory in order to reproduce the experimentally-observed spectrum. A total of four excited states with vertical excitation energies below 7 eV have significant oscillator strengths (larger than 0.1).
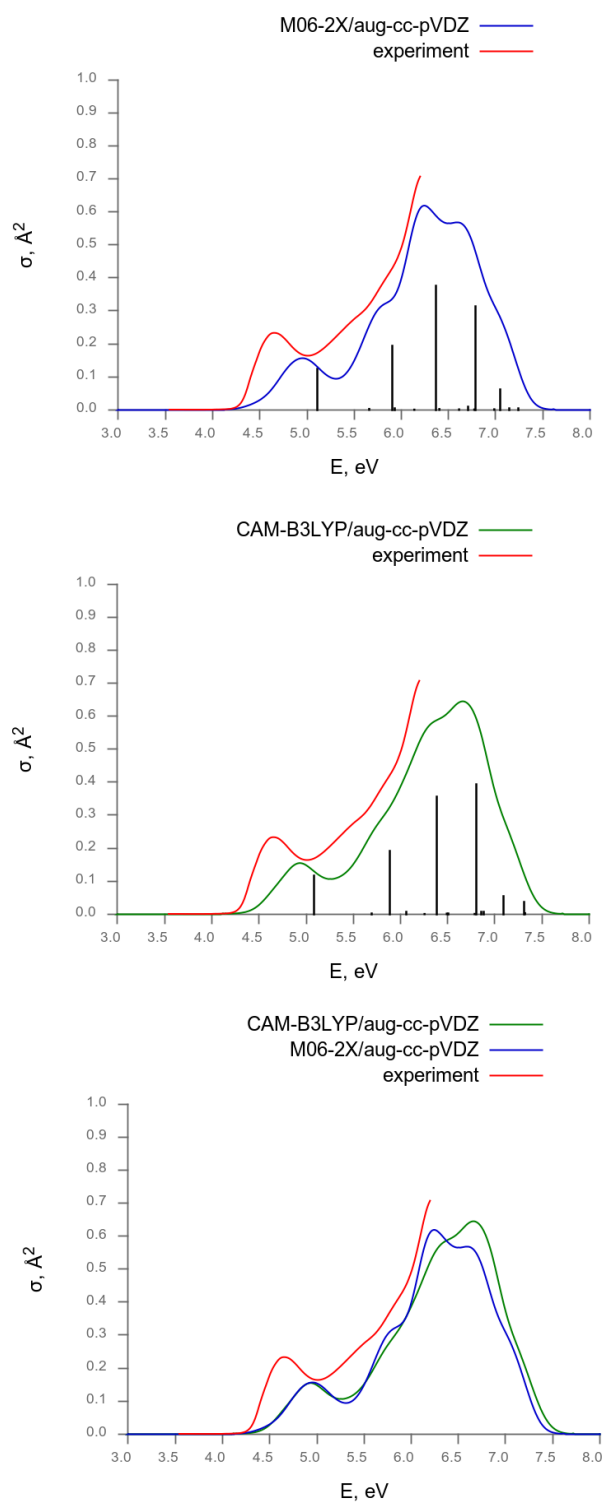
Figure 4.15: Spectrum of cytosine simulated on the level of M062X/aug-cc-pVDZ and CAM-B3LYP/aug-cc-pVDZ without an explicit hydration shell, but only bulk solvent taken into account within the polarizable continuous medium (PCM) method (experimental data by courtesy of Alessandra Picchiotti, Max Planck Institute for the Structure and Dynamics of Matter Hamburg). The vertical bars indicate the associated stick spectrum .
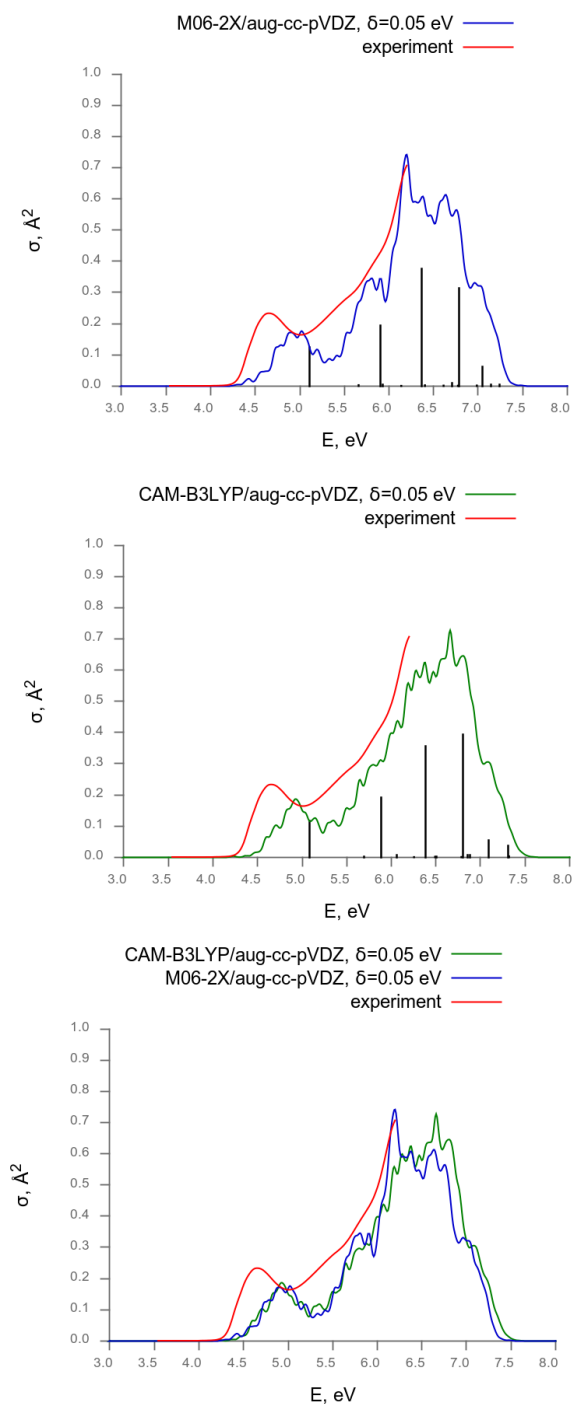
Dependence on line-shape parameter

Figure 4.16: Simulated spectra for cytosine on the level of M062X/aug-cc-pVDZ and CAM-B3LYP/aug-cc-pVDZ by including bulk solvent within the PCM method and neglecting explicit microsolvation, changing the δ parameter from 0.2 eV to 0.05 eV (experimental data by courtesy of Alessandra Picchiotti, Max Planck Institute for the Structure and Dynamics of Matter Hamburg).

In the spectral simulations reported in this work, the value of the line-shape parameter δ, which appears in Eq. (3.15) and which controls the width of the line-shape function, was set to the relatively large value of 0.2 eV. The reason for this choice is the aim to obtain smooth simulated spectra to facilitate the comparison with the experiment. With the goal of understanding the role of the line-shape parameter, we have investigated the effect of using a smaller value of δ by recalculating the PCM-only spectra of cytosine without an explicit hydration shell, by setting δ=0.05 eV. The resulting absorption spectra are shown in Fig. 4.16. We find that the spectra obtained with the smaller value of δ have a rough and less smooth shape due to statistical noise in the calculations, but the overall shapes of the absorption bands are essentially the same as with δ=0.2 eV. Hence, this justifies the use of the larger value of δ=0.2 eV to obtain a smooth spectrum which is in fair agreement with the experimental data.

4.3 Conclusions

The photoabsorption spectra of the four canonical DNA nucleobases explicitly coupled to a hydration shell of water molecules and embedded in bulk aqueous solution have been simulated using the semiclassical nuclear ensemble method in combination with the time-dependent density functional theory and two choices of the exchange-correlation functional (the M06-2X and CAM-B3LYP functionals). A major difference to existing approaches is that we have explicitly included a finite number of water molecules in the simulations which form a hydration shell. We find that the hydration shell of the microsolvated nucleobases plays an important role. In general, both functionals reproduce the general form of the experimentally observed photoabsorption spectra, while at the same time giving rise to a systematic energy shift in the calculated positions of absorption peaks. Importantly, we confirm that the M06-2X and CAM-B3LYP functionals do not give rise to spurious intermolecular charge transfer excited states when the explicitly solvated nucleobase molecules are considered. Therefore, these functionals are well suited for the simulation of the photoabsorption spectra, when hydration shells are included explicitly.

Hydrogen bonding with explicit solvent molecules destabilizes the $n\pi^*$-type excited states of all four nucleobases relative to the low-lying $\pi\pi^*$-type excited states. This destabilization will persist following photoexcitation into the low-lying bright $\pi\pi^*$-type states for as long as the system remains near the Franck-Condon geometry, and all hydrogen bonds with the solvating water molecules are intact. During this period of time, the $n\pi^*$-type states will therefore be too high in energy to be populated to a significant extent. It follows that a rearrangement of the solvating water molecules is a prerequisite for population transfer into the $n\pi^*$-type states. Precisely this sequence of events was recently predicted to take place in the relaxation dynamics of microsolvated 7H-adenine [93]: in this system, the populated state initially had a pure $\pi\pi^*$ character, and gradually acquired a mixed $\pi\pi^*$- and $n\pi^*$-type character concurrently with a rearrangement of the solvation shell. The latter process occurred on a timescale of 100-200 fs. Extrapolating to the other nucleobase molecules in aqueous solution, we therefore expect that hydrogen bonding with the solvent will generally delay population transfer into the $n\pi^*$-type at least until some 100-200 fs following the initial photoexcitation.

Moreover, the additional inclusion of vibrational broadening seems essential for a reliable comparison of simulated photoabsorption spectra with experimental data, as the peaks in the vibrationally-broadened spectra are consistently red-shifted with respect to the vertical excitation energies calculated at the ground-state equilibrium geometries. Further spectroscopic studies in terms of ultrafast 2D spectroscopy is necessary to confirm this picture. Yet, the present study can serve as a basis for future simulations of experimental 2D spectra.

92

Chapter 5

2D electronic spectroscopy of adenine

Adenine is a prominent example of the decay behavior of DNA nucleobases, exhibiting ultrafast radiationsless decay and low emission quantum yields, which has been extensively investigated, but sofar no definite agreement concerning the relaxation mechanism after excitation has been reached. Recently, the photophysics of nucleobases was experimentally investigated by means of transient absorption (pump-probe) and 2D spectroscopies [109] at the Max Planck Institute for the Structure and Dynamics of Matter (Hamburg) in the Coherent Control and Multidimensional Spectroscopy group. As an example, Fig. 5.1 presents experimental pump-probe spectra and 2D spectrum at T=225 fs for adenine in water.

They found that, in all nucleobases, deactivation of the induced population occurs via a "dark" state which is presumably the so-called $n\pi^*$ state, populated from the excited state $\pi\pi^*$ via conical intersection (CI) between them. Further decay of the population of the $n\pi^*$ state occurs via the second CI which connects the $n\pi^*$ and ground states. From the experiments the authors derived a spectroscopic model, shown on Fig. 5.2, which convincingly explains their observation [109].

In the following we focus our consideration on the dominant 9H-isomer of adenine. In the first part we present the modeling results of the 2D electronic spectroscopy, based on phenomenological model (a) (Fig. 5.2) and obtained
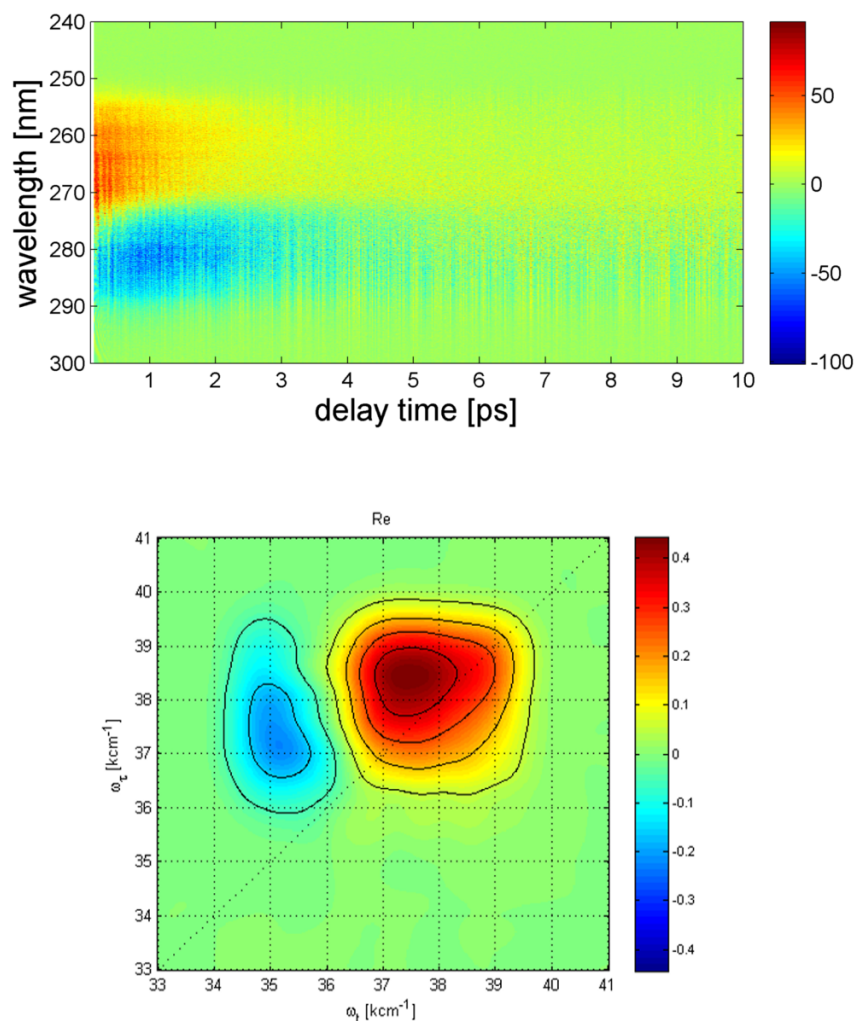
Figure 5.1: Experimental transient absorption (top) and 2D spectra of 9H-adenine for waiting time T=225 fs (bottom) [109] (experimental data by courtesy of Alessandra Picchiotti, Max Planck Institute for the Structure and Dynamics of Matter Hamburg).

by applying the TNL method, which has been introduced in Section 3.3.
In the second part of this Chapter, we will use the exact hierarchy equation of motion (HEOM) approach to compare calculated 2D electronic spectra
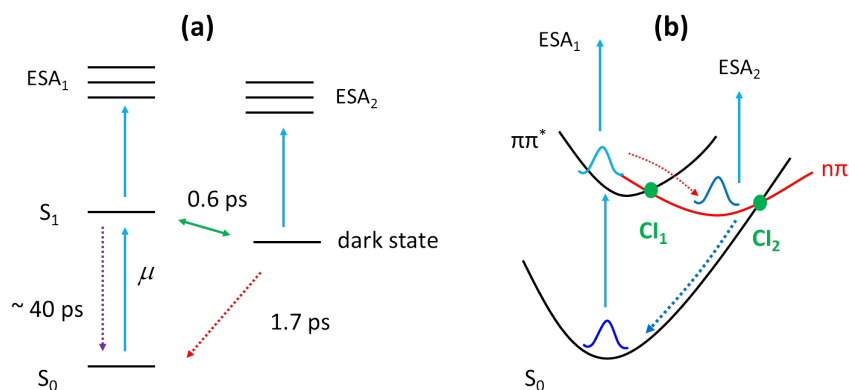
Figure 5.2: Spectroscopic model derived from the experiments: phenomeno-logical (a) and quantum-chemical (b)

with those obtained from the approximate TNL method and with the experimental one. However, the HEOM approach is exact only for a specifically chosen spectral density of bath states which restricts the modeling to a high temperature limit. For this modeling we will use the quantum-mechanical spectroscopic model (b) (Fig. 5.2) which explicitly accounts for two CIs and also includes a basic vibrational structure for the involved excited states.

5.1 Time Nonlocal Method

5.1.1 Theoretical modeling

Although several excited states play a role in the dynamics of photoexcited adenine, and many decay paths are proposed for this molecule, see Sec. 1.2, we focus here on a minimal kinetic model derived from experimental results which is schematically shown in Fig. 5.3 (see also panel (a) in Fig. 5.2) in which the first CI is formally accounted for by introducing a coupling parameter V between "bright" and "dark" states.
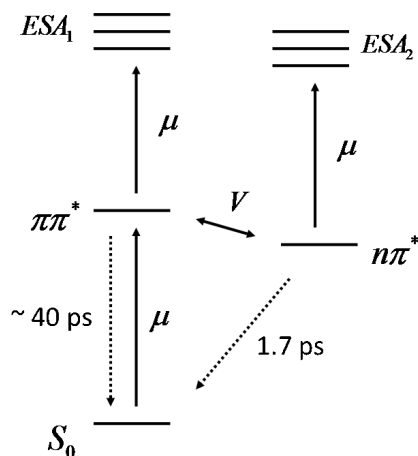
Figure 5.3: Phenomenological model for the UV deactivation of 9H-adenine

After the excitation of the molecule from the ground state S_0 to the S_1 $\pi\pi^*$ excited state, the deactivation of population to the ground state occurs directly (weak channel, approximately 40 ps decay) and via a dark $n\pi^*$ state (main channel, approximately 700 fs decay). Two higher excited states ESA_1 and ESA_2 contribute to the measured signals due to absorption from the populated $\pi\pi^*$ and $n\pi^*$, respectively. μ indicates the transition dipole moments associated with the excitations to the bright state involved in this theoretical model and to highly-excited states.

Transient absorption spectroscopy of adenine reveals three decay times: the shortest is due to the flow of population from the excited to the "dark" state. The associated decay time is $\sim 0.6 - 0.7$ ps. Depopulation of the dark state occurs via a CI with the ground state S_0 within a decay time of $\sim 1.5 - 1.8$ ps. The third channel is the direct population decay to the ground state from the excited S_1 state with a decay time of ~ 40 ps. In

the present modeling these last two decay channels will be accounted for phenomenologically (see below).

The formalized Hamiltonian belonging to the energy level scheme of Fig. 5.3 is

$$H_s = \begin{pmatrix} g & 0 & 0 & 0 & 0 \\ 0 & \epsilon_{\pi\pi^*} & V & 0 & 0 \\ 0 & V & \epsilon_{n\pi^*} & 0 & 0 \\ 0 & 0 & 0 & \epsilon_{ESA_{\pi\pi^*}} & 0 \\ 0 & 0 & 0 & 0 & \epsilon_{ESA_{n\pi^*}} \end{pmatrix} \tag{5.1}$$

where $\epsilon_{\pi\pi^*} = 37600$ cm^{-1} and $\epsilon_{n\pi^*} = 37150$ cm^{-1} are the energies of the S_1 $\pi\pi^*$ and the dark $n\pi^*$ states, $V = 50$ cm^{-1} is the coupling energy between the two states, $\epsilon_{ESA_{\pi\pi^*}} = 72600$ cm^{-1} and $\epsilon_{ESA_{n\pi^*}} 71650$ cm^{-1} are the energies of the two excited state absorption states.

In Subsection 3.3.2 we reviewed the theory of the TNL method. According to this approach, the Liouville equation describing the evolution of the total system, formed by the system and the bath, is first projected following the procedure of Nakajima–Zwanzig [67] and then decomposed into a set of coupled equations for ρ_s, $\rho_k^r(t)$, $\rho_k^l(t)$ which are local in time but still treat both memory and initial correlations correctly (see Ref. [69])

$$\dot{\rho}_s(t) = \mathcal{L}_s^{eff}(t)\rho_s(t) + \lambda \times \left(\sum_{k=1}^{n_r} \alpha_k^r \mathcal{L}^- \rho_k^r(t) + \sum_{k=1}^{n_l} \alpha_k^l \mathcal{L}^- \rho_k^l(t) \right), \tag{5.2}$$

$$\dot{\rho}_k^r(t) = (\mathcal{L}_s(t) + \gamma_k^r)\rho_k^r(t) + \lambda \mathcal{L}^- \rho_s(t) \quad k = 1, n_r, \tag{5.3}$$

$$\dot{\rho}_k^l(t) = (\mathcal{L}_s(t) + \gamma_k^l)\rho_k^l(t) + \lambda \mathcal{L}^+ \rho_s(t) \quad k = 1, n_l. \tag{5.4}$$

This approach can be applied to reproduce the linear and the 2D electronic spectra of our simplified model for 9H-adenine. The decays of the bright and dark states to the ground state S_0 are not explicitly included in the TNL model, but their contributions are modeled using a Lindblad equation:

$$\dot{\rho}(t) = -i[H, \rho(t)] + \sum_{k=1}^{M} \gamma_k \left(L_k \rho(t) L_k^\dagger - \frac{1}{2} L_k^\dagger L_k \rho(t) - \frac{1}{2} \rho(t) L_k^\dagger L_k \right) \tag{5.5}$$

5.1.2   Results

The calculated linear absorption spectrum of 9H-adenine is shown in Fig. 5.4. Overlapped in the same plot the experimental absorption and the laser spectra are shown for comparison.

The spectrum seems to be very narrow as compared to the experimental one, and this is due to the fact that in the current investigation we're more focused on fitting the transient absorption spectra. The model is subject to improvement, in order to get a satisfactory agreement with experimental linear absorption spectra. The 2D spectra, calculated for different waiting
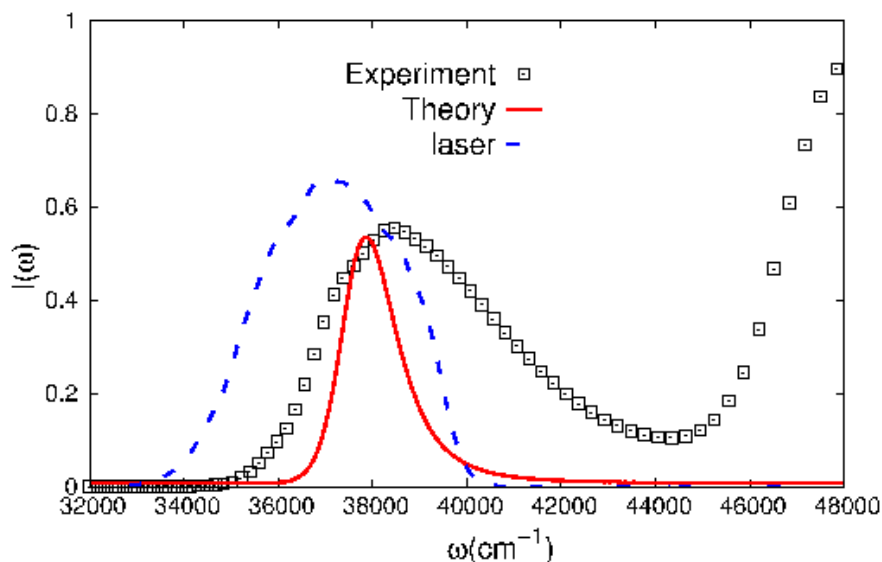
Figure 5.4: Theoretical and experimental absorption spectrum of 9H-adenine, overlapped is the laser spectrum (blue dotted line) (experimental data by courtesy of Alessandra Picchiotti, Max Planck Institute for the Structure and Dynamics of Matter Hamburg).

times, are shown in Fig. 5.5. For calculation of this spectrum we used an infinitely-short laser pulse (impulsive limit in excitation).

Direct comparison with Fig. 5.1 shows good agreement between the magnitudes and positions of positive and negative peaks in the simulated and experimental spectra. This is a first confirmation of the reliability of the spectroscopic model proposed in Ref. [109].
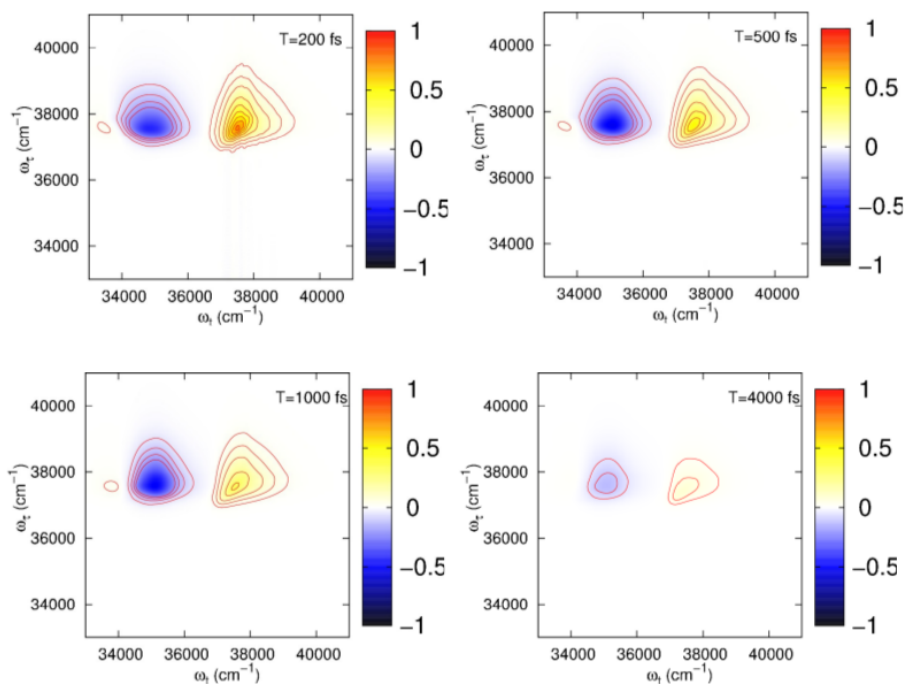
Figure 5.5: Simulated 2D spectra of 9H-adenine shown at four values of the waiting time T.

Transient Absorption

Transient absorption spectroscopy is perhaps the most widely used third-order nonlinear experiment. It can be applied to follow many types of time-dependent relaxation processes and chemical dynamics, and is most commonly used to follow population relaxation, chemical kinetics, dynamics of wavepacket created by excitation at different electronic potential surfaces, and quantum beats.

Two pulses separated by a delay τ are crossed in a sample: a pump pulse and a time-delayed probe pulse. The pump pulse E_{pu} creates a non-equilibrium state, and the time-dependent changes in the sample are characterized by the probe-pulse E_{pr} through the pump-induced intensity change in the transmitted probe, ΔT. The described interaction mechanism between the pulses and sample is depicted in Fig. 5.6.
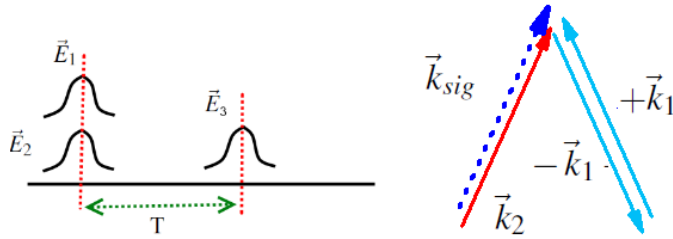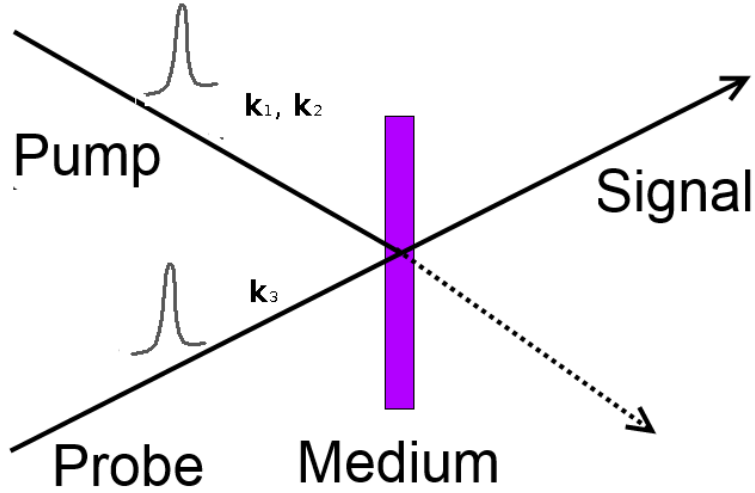
Figure 5.6: Pump probe setup (picture taken from: Tomakoff Group, Nonlinear and Two dimensional Spectroscopy Notes).

Calculation of the pump-probe (PP) spectra of 9H-adenine was performed according to the method introduced in Ref. [110], briefly reviewed in the following.

The system's response to the applied fields

$$\mathcal{E}_a(t) = \lambda_a E_a(t - \tau_a) \exp i(\mathbf{k}_a \mathbf{r} - \omega_a t) \qquad (5.6)$$

where λ_a, $\mathbf{k}_a$, ω_a and τ_a denote amplitude, wavevector, frequency and temporal position of the pulses, is determined by the total complex nonlinear

polarization

$$P(\mathbf{r}, t) = \text{Tr}[\mu\rho(\mathbf{r}, t)] \tag{5.7}$$

which contains contributions corresponding to all possible values of the wave vector $\mathbf{k} = l_1\mathbf{k}_1 + l_2\mathbf{k}_2$, with l_a being arbitrary integers. The pump probe polarization $P_{PP}(t)$ corresponds to the phase-matching condition $l_1 = 0$, $l_2 = 1$. $P_{PP}(t)$ can be retrieved from the total polarization $P(t)$ by the formula

$$P_{PP}(t) = \frac{1}{2\pi} \int_0^{2\pi} d\varphi_2 \exp\left[-i\varphi_2\right]P(\varphi_2; t), \tag{5.8}$$

where $P(\varphi_2; t)$ is computed for specific values of the phase angles ($\mathbf{k}_1\mathbf{r} = 0$ and $\mathbf{k}_2\mathbf{r} = \varphi_2$). Once $P_{PP}(t)$ has been determined, the transient absorption integral PP signal is obtained according to

$$S_{PP}(t) = Im \int_{-\infty}^{\infty} dt \mathcal{E}_2(t)(P_{PP}(t) - P_{PP}^{off}(t)), \tag{5.9}$$

where $P_{PP}^{off}(t)$ is the polarization induced solely by the probe pulse, and $T = \tau_2 - \tau_1$ is the time delay between the pump and probe pulses.

Pump probe spectra have been simulated for 9H-adenine by applying the already introduced TNL model.
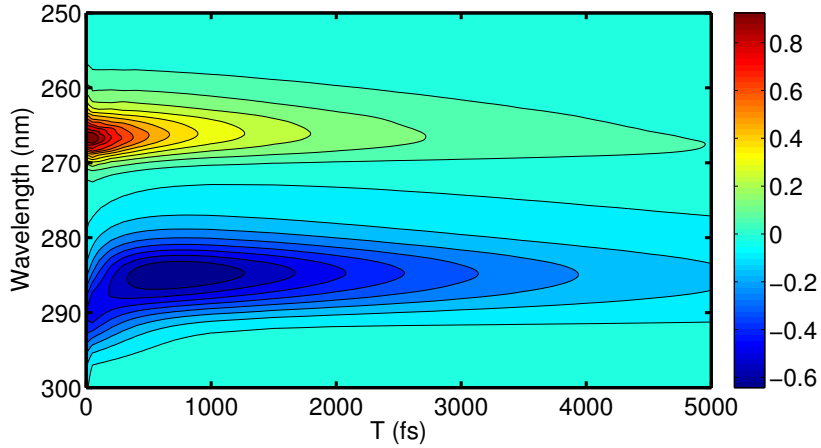

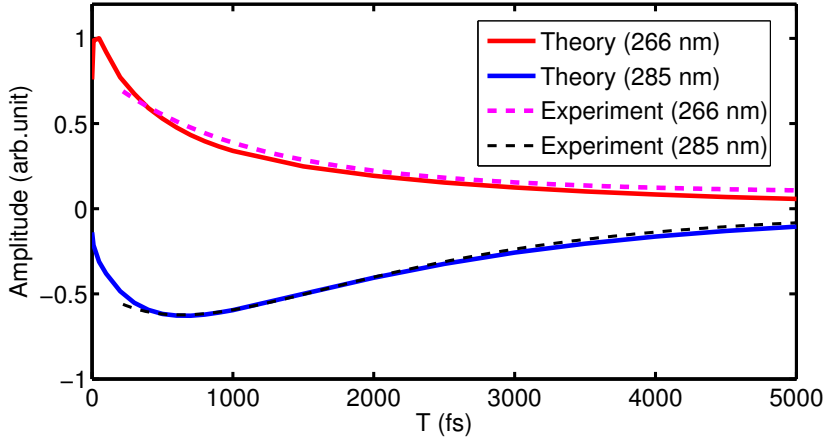Figure 5.7: Simulated pump-probe spectrum of 9H-adenine

Figure 5.8: Pump probe amplitude of 9H-adenine (experimental data by courtesy of Alessandra Picchiotti, Max Planck Institute for the Structure and Dynamics of Matter Hamburg).

In Fig. 5.7 we show numerically simulated pump-probe spectrum, while in Fig. 5.8 the experimental and calculated PP traces are overlaid, showing good agreement between each other. The red and blue lines are the PP amplitude profiles of the red and the blue peak in the calculated spectra, respectively. The increasing trend in the PP-amplitude of the blue peaks, which reflects a decay of $\pi\pi^*$ state and population growth of $n\pi^*$ state monitored via ESA, is reproduced very well.

From the relatively good agreement between the experimental and numerical results, we can conclude that the phenomenological model shown in Fig. 5.2 (a) supports the experimental observation and validates our theoretical model. Moreover, concerning the results already achieved for adenine and presented in Sec. 1.2, we can conclude that our results of numerical simulation of the PP kinetics supports two of the three decay pathways found in experiments [109], i.e. the $^1L_a\pi\pi^* \rightarrow n\pi^* \rightarrow S_0$ and the $^1L_a\pi\pi^* \rightarrow S_0$ paths.

5.2   Hierarchy Equations of Motion

The 2D and pump-probe spectra of adenine in aqueous solution have been also simulated by applying the second method, the Hierarchy equations of motion, which was already briefly introduced in Section 3.3.3. This is a more accurate and precise method and also allows us to take into consideration both CIs explicitly. The signatures of conical intersections have been detected, and the results obtained from these simulations will be presented in this section.

Many molecules of interest in spectroscopy exhibit conical intersections [111]-[118]. Here, we focus in particular on a conical intersection between the electronic excited state and the ground state, in addition to possible conical intersections between the excited states. Such conical intersections have been suggested to be present in the nucleobase 9H-adenine (see Section 1.2 and the References listed therein), where they are responsible for ultrafast deactivation of the excited state. Due to fast dynamics, a rich waiting time dependence of the two-dimensional spectrum is expected for these systems [119]-[121]. Of particular interest in this study are the conical intersections between excited and the ground states.

Nonadiabatic coupling between the excited and ground states was also considered for a one-dimensional model by Tanimura [79]. In the one-dimensional model used, a coupling between diabatic states leads to avoided crossing of the adiabatic surfaces. To go one step further and obtain a conical intersection of these surfaces, one needs to introduce at least two vibrational modes [122].

Although several excited states play a role in the wavepacket dynamics of photoexcited adenine [123], we focus here on a minimal model that corresponds to the kinetic model derived from the experimental results and depicted in Fig. 5.2 (b).

5.2.1   Theoretical modeling

A minimal model for a conical intersection is the linear vibronic coupling model [124, 119]. In this work, we will generalize this model to include three potential energy surfaces with two CIs: the ground state, a bright
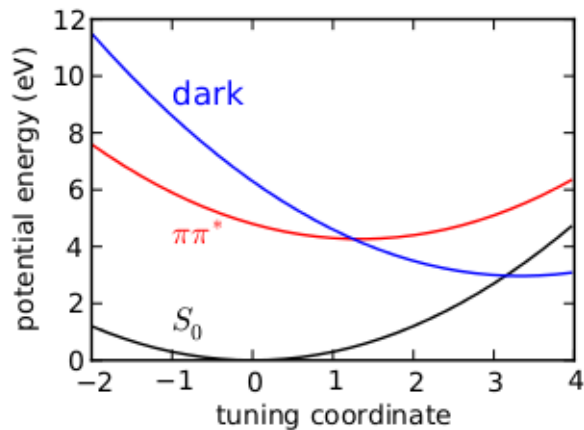
Figure 5.9: Diabatic potential energy surfaces along the tuning coordinate Q_2.

$\pi\pi^*$ state and a dark state, see Fig. 5.9. In addition, as in the previous modeling, we include the ESA channels for both the bright and the dark state (not shown). This model differs from the previous one considered in the framework of TNL by inclusion of a vibronic structure composed by two vibrational states, which are thought to play an important role in the dynamics of the excited states. The present model sketched in Fig. 5.9 includes both conical intersections CI_1 and CI_2; however, the direct decay channel from the excited to the ground state is not accounted for(due to a very long decay time as compared to the fast deactivation pathways). It should be noted that, in this model, numerical calculations are limited by the shapes of potential surfaces: all of them are parabolic (harmonic potentials) and have the same curvatures.

In this model, three coordinates are involved: the tuning coordinate, along which the coupling between diabatic states changes, and two coupling coordinates, one for each considered conical intersection. This is a generalization of the treatment introduced in Chapter 3 (where just one coordinate was describing both the two CIs), ensuring a more accurate description of the model.

The potential energy surfaces along the tuning coordinate are harmonic,

and the dependence of the diabatic coupling on the coupling coordinate is linear. This coupling coordinate is not explicitly shown in Fig. 5.9. Ideally, it would be perpendicular to the plane on which the tuning-dependent potential surfaces are lying. In the present model the tuning and coupling coordinates have separate and uncorrelated vibrational modes.

Three parabolas represent the three harmonic potentials corresponding to the ground state S_0, the bright $\pi\pi^*$ and the dark state $n\pi^*$.

The Hamiltonian is given as the sum of a Hamiltonian for the two potential energy surfaces and a Hamiltonian for their coupling to the harmonic oscillator bath. The first part of the Hamiltonian for three modes is given by

$$
\begin{aligned}
H_P &= \epsilon_e|e\rangle\langle e| + \epsilon_d|d\rangle\langle d| \\
&+ M_2\Omega_2^2 Q_2 d_e D_2|e\rangle\langle e| + M_2\Omega_2^2 Q_2 d_d D_2|d\rangle\langle d| \\
&+ M_1\Omega_1^2 Q_1 D_1(d_{V1}|d\rangle\langle e| + \text{h.c.}) \\
&+ M_{1'}\Omega_{1'}^2 Q_{1'} D_{1'}(d_{V1'}|g\rangle\langle d| + \text{h.c.}),
\end{aligned}
\tag{5.10}
$$

where ϵ_e and ϵ_d are the vertical transition energies of the $\pi\pi^*$ state $|e\rangle$ and dark state $|d\rangle$, M_j, D_j and Ω_j are masses, length scales and frequencies of the modes with coordinates Q_j, and d_i are the dimensionless displacements. The potentials for the tuning coordinate Q_2 and the coupling coordinates Q_1 and $Q_{1'}$ are harmonic.

In order to describe damping, we couple the system Hamiltonian to a bath consisting of infinitely many harmonic oscillators. The interaction of the coupling and tuning modes with the bath is given by the Hamiltonian:

$$
\begin{aligned}
H_{SB} &= \sum_\alpha \{ \frac{p_\alpha^2}{2m_\alpha} + \frac{1}{2}m_\alpha\omega_\alpha^2(x_\alpha - \frac{g_{1\alpha}}{m_\alpha\omega_\alpha^2}Q_1)^2 \\
&+ \frac{1}{2}m_\alpha\omega_\alpha^2(x_\alpha - \frac{g_{1'\alpha}}{m_\alpha\omega_\alpha^2}Q_{1'})^2 \\
&+ \frac{1}{2}m_\alpha\omega_\alpha^2(x_\alpha - \frac{g_{2\alpha}}{m_\alpha\omega_\alpha^2}Q_2)^2 \},
\end{aligned}
\tag{5.11}
$$

where m_α, ω_α, x_α and p_α are the masses, frequencies, coordinates and momenta of the infinitely many harmonic bath oscillators, and $g_{i\alpha}$ are their coupling strengths to the system.

Because of the assumed linear coupling to a harmonic bath, all information about the bath and the system bath coupling is encoded in the spectral densities. The spectral densities are defined as

$$J_i(\omega) = \sum_\alpha \frac{g_{i\alpha}^2}{2m_\alpha \omega_\alpha} \delta(\omega - \omega_\alpha), \tag{5.12}$$

and are chosen to be Ohmic,

$$J(\omega) = M_i \gamma_i \omega \exp{-\omega/\Lambda}, \tag{5.13}$$

where we will take the cut-off Λ larger than all other frequencies in the system, so that it can be set to infinity. The parameters γ_i measure the strength of the damping.

Through a canonical transformation the Hamiltonian is rewritten as [78]

$$
\begin{aligned}
H \;=\;& \epsilon_e |e\rangle\langle e| + \epsilon_d |d\rangle\langle d| \\
& - (d_d |d\rangle\langle d| + d_e |e\rangle\langle e|) \sum_\alpha g'_{2\alpha} x'_\alpha \\
& - (d_{V1} |d\rangle\langle e| + \text{h.c.}) \sum_\alpha g'_{1\alpha} x'_\alpha \\
& - (d_{V1'} |g\rangle\langle d| + \text{h.c.}) \sum_\alpha g'_{1'\alpha} x'_\alpha
\end{aligned}
\tag{5.14}
$$

The transformed spectral density, defined for the couplings to the transformed bath $g'_{i\alpha}$ is of the Brownian oscillator form, with reorganization energies $\lambda_i = M_i D_i^2 \Omega_i^2 / 2\pi\hbar$. In the overdamped limit, which allows the simplest calculation and agrees with experimental results, we approximate the spectral density by the Debye form

$$J_{i\text{OD}}(\omega) = 2\lambda_i \omega_{c,i} \frac{\omega}{\omega^2 + \omega_{c,i}^2}, \tag{5.15}$$

where $\omega_{c,i}$ is the cut-off frequency.

A hierarchy of equations of motion can be derived by generalizing the treatment in Refs. [77] and [79] to three coordinates and overdamped baths. In our calculations, we use the form of the hierarchy proposed in Ref. [125]. Linear spectra, pump-probe spectra and two-dimensional optical spectra can be calculated with the standard perturbative method. In order to include induced absorption in the calculation of two-dimensional spectra, we add two

levels with energies ϵ_{f1} and ϵ_{f2}, which can be excited optically from the $\pi\pi^*$ and dark states, respectively. We do not include dynamics for these states in the model. Therefore, they are simply characterized by their excitation energies ϵ_{f1} and ϵ_{f2} and transition dipoles μ_{ESA1} and μ_{ESA2}.

5.2.2 Results

In the calculation we used the following set of parameters which allows satisfactory agreement between the modeled and experimental data: $\epsilon_e = 4.75$ eV, $\epsilon_d = 6.3$ eV, $d_e^2\lambda_2 = 16$ meV, $d_d^2\lambda_2 = 100$ meV, $d_{V1}^2\lambda_1 = 9.6$ meV, $d_{V1'}^2\lambda_{1'} = 4.32$ meV, $\omega_{c,1} = \omega_{c,1'} = 0.5$ eV, $\omega_{c,2} = 0.15$ eV and $\epsilon_{f1} = 8.8$ eV, $\epsilon_{f2} = 10.3$ eV, $\mu_{\text{ESA1}} = 0.7$, $\mu_{\pi\pi^*}$, $\mu_{\text{ESA2}} = 2.0$, $\mu_{\pi\pi^*}$ and $\beta = 0.5/$ eV.

In the numerical simulations of 2D and PP spectra horizontal displacements d_e and d_d play a significant role through their product with the reorganization energy λ_2, which gives the strength of the coupling to the bath of the tuning coordinate. The response function formalism with delta (infinitely short) laser pulses has been used for the current calculations.
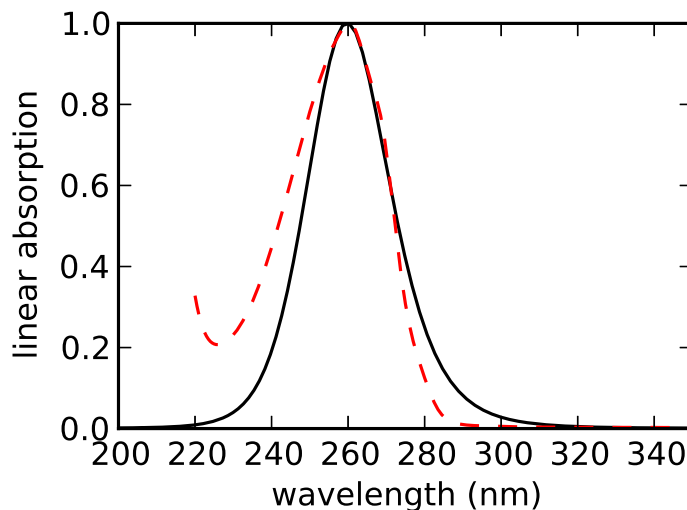

Figure 5.10: (solid) Calculated and (dashed) experimental linear spectrum (experimental data by courtesy of Alessandra Picchiotti, Max Planck Institute for the Structure and Dynamics of Matter Hamburg).

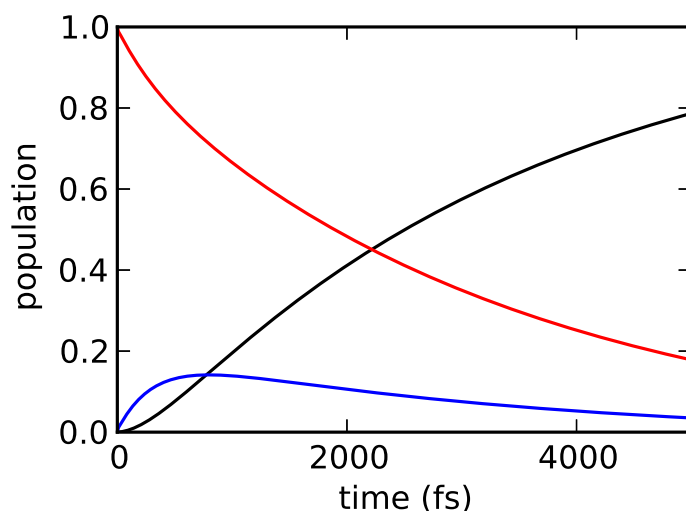In Fig. 5.10 the calculated and the experimentally obtained linear ab-

Figure 5.11: Dynamics of a system with two conical intersections. Plotted are the populations of the diabatic states. Color coding is as in the potential energy surfaces in figure 5.9.

sorption spectra are overlaid: by comparing with Fig. 5.4 we can see a much better performance of the HEOM method with respect to the TNL approach, at least for simulation of the linear absorption spectra.

The population kinetics of the diabatic states is plotted in Fig. 5.11, where the color coding corresponds to the coloring of potential energy surfaces in Fig. 5.9. The pump-probe spectra as a function of waiting time is depicted in Fig. 5.12 and shows qualitative agreement with the experimental PP-spectra, see top panel in Fig. 5.1. The positive peak (plotted in the red and yellow colors) is related to the processes of bleaching and stimulated emission, the negative peak (plotted in the light-blue color) is the signal representative of the mechanism of induced absorption. It visualizes the population of dark state via the excited-state absorption.

Figure 5.13 shows the calculated pump-probe slices through the pump-probe spectrum at fixed frequency as a function of waiting time. The main features of the experimental data, namely a gradual decrease of the positive peak and an increase of the amplitude of the negative peak on a time scale of 100s of femtoseconds, followed by a decrease on a picosecond time scale,
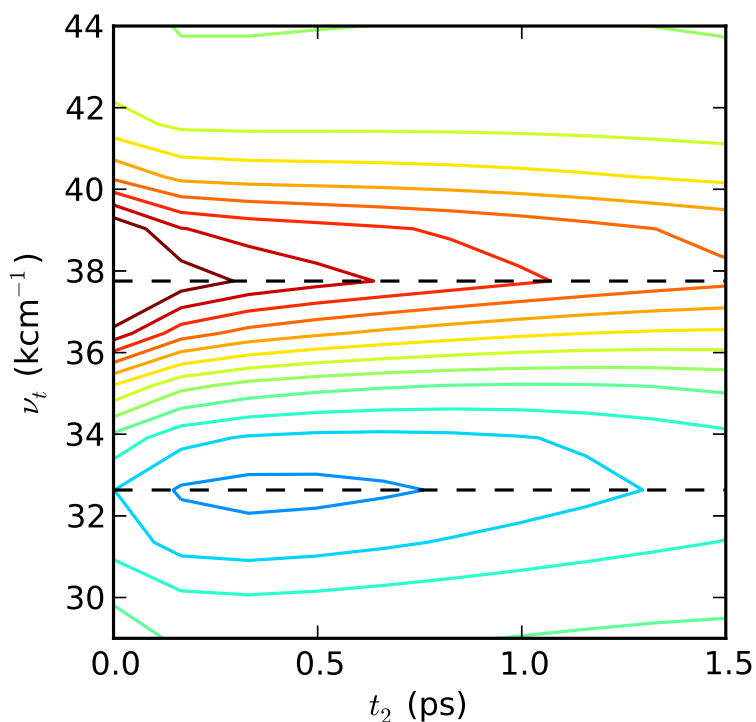
Figure 5.12: Calculated pump probe spectrum as a function of waiting time.

are well reproduced.

In Fig. 5.14 calculated two-dimensional optical spectra are shown for various waiting times: size and relative position of the two lobes with opposite signs reproduces well the experimental observations (Fig. 5.1). The observed spectral shift of ≈ 2000 cm^{-1} in the calculated 2D spectra to higher energies is most likely due to some drawbacks of spectroscopic model used for calculations (harmonic shapes of the PESs with equal curvatures) as well as due to setting of parameters for calculations (transition energies). The decrease in intensity of the peaks is a result of the dynamics through conical intersections.

The main limitation of our model is the equal curvatures of all electronic states, which should differ from each other in a more exact treatment of the problem. The second limitation is the Condon approximation (constant transition dipole moments) used in the calculations. A more realistic model
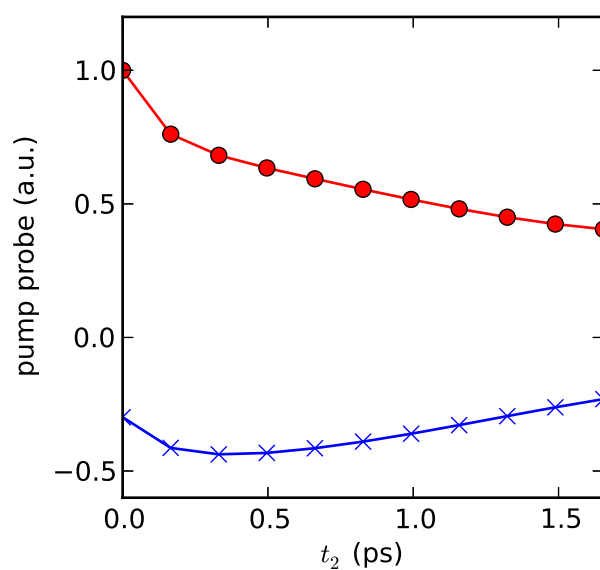
Figure 5.13: Slices through the pump-probe signal for (red) the positive and (blue) the negative peak as a function of waiting time. Slices were taken at the points indicated by the dashed line in Figure 5.12.

should account for dependency of transition dipole moments on the nuclear coordinates.

Future work will be devoted to solving these issues and going beyond the approximations used in this preliminary, but quite promising study.
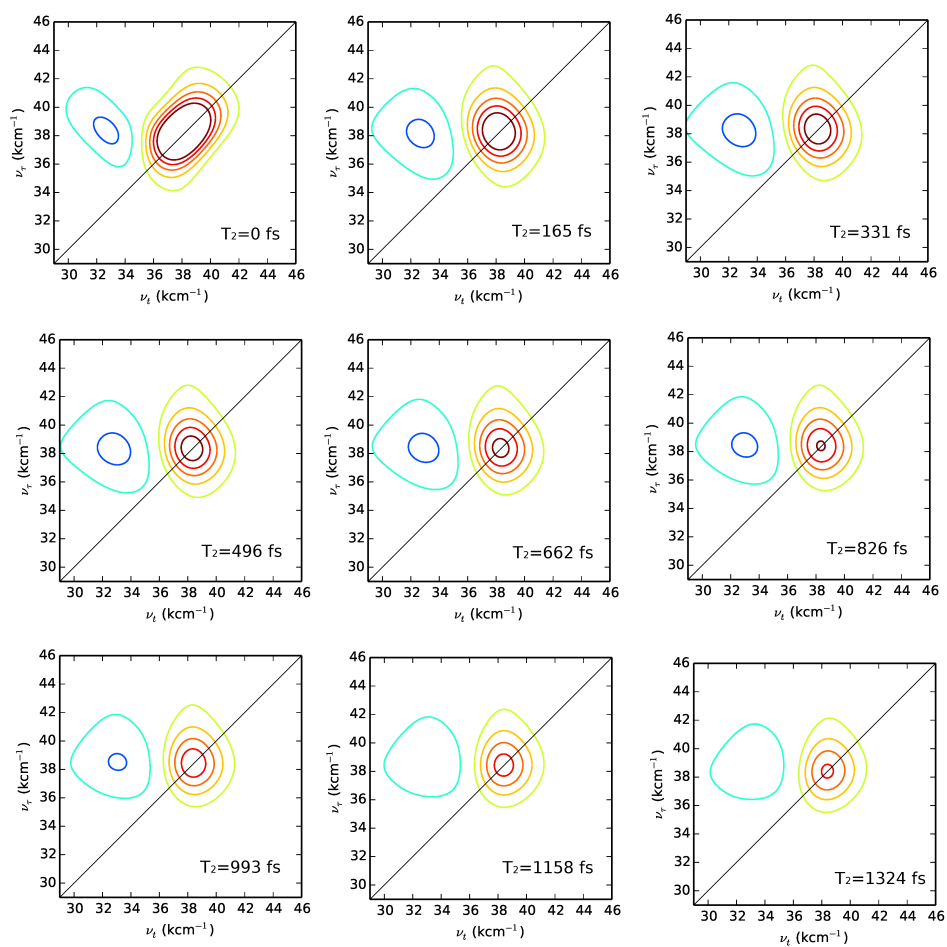
Figure 5.14: Calculated two-dimensional optical spectra for various waiting times.

112

Chapter 6

Conclusions

The present work was devoted to the study of linear and two-dimensional electronic spectroscopy of DNA nucleobases. Introduction of the theoretical background, explanation of the used computational methods and description of main results are provided.

UV photochemistry of nucleic acids is a subject of big interest, as UV electronic excitations trigger a sequence of events which may lead to UV-induced damage of DNA, with all its profound and vast biological consequences (e.g. mutagenic and carcinogic effects). This has a big impact in understanding of exact circumstances for the beginning of life on Earth, since much of the prebiotic chemistry probably occurred under intense UV irradiation.

On the other side, investigating the fundamental processes underlying UV photochemistry of DNA constituents can have extremely important medical applications, for what concerns the damaging processes following the UV irradiation, which is one of the main cause of skin cancer [126].

To date, not so much is known about the dynamics of the electronic states of these DNA macromolecules.

In this work, we intend to provide for the first time a tractable low-dimensional model of the excited state dynamics of DNA nucleobases in presence of external fluctuations induced by the solvent. In order to do so, we follow the so-called reductionist approach and start our analysis from the single nucleobases and their UV photophysics, studied in terms of linear

and 2DES spectroscopy.

After UV photoexcitation, all four DNA nucleobases return to the ground state by means of internal conversion processes at the scale of a few picoseconds, a fact that has been often related to the intrinsic photostability of these bases. The electronic excited states involved in such decay processes have been intensively investigated in the last decades, but no common picture for the relaxation of DNA nucleobases have been reached yet.

Understanding and simulating linear absorption spectra of DNA constituents is a first necessary step in this direction, and this is the motivation for the first part of the present study, where the UV absorption spectra of the four DNA nucleobases in aqueous solution have been modeled. The calculation has been performed by using a combination of time-dependent density functional theory and the semiclassical nuclear ensemble method [56]. The water molecules forming the microsolvation shell are explicitly included and the entire complex is placed in a bulk water solvent represented as a continuous polarizable dielectric medium (PCM). The simulated spectra are compared to experimentally measured absorption spectra. Apart from a systematic shift of 0.3 eV of the absorption peaks, the calculated photoabsorption spectra reproduce the measured ones with good accuracy. The effect of the solvation shell seems significant: the lone electron pairs in the hydrogen bonding with the solvating water molecules systematically increases the energies of vertical excitation into the $n\pi^*$-type states. As a consequence, the energies of vertical excitation into the $n\pi^*$-type states are higher by a few tenths of an electronvolt for the microsolvated bases than the energies for the excitation into the lowest $\pi\pi^*$-states. This is in contrast to the case of isolated nucleobases, where the energies of the lowest $n\pi^*$- and $\pi\pi^*$-type states are comparable.

The additional inclusion of vibrational broadening, implicit in the use of the semiclassical ensemble method, seems essential for a reliable comparison of simulated photoabsorption spectra with experimental data, as the peaks in the vibrationally-broadened spectra are consistently red-shifted with respect to the vertical excitation energies calculated at the ground-state equilibrium geometries.

One of the goals of this project is also to determine optical properties of DNA nucleobases in terms of the third-order response function, which yields a direct connection of the theoretical modelings to experimental results of 4-wave-mixing time-resolved optical spectroscopies, in particular to photon-echo-based 2D-UV and transient absorption spectroscopies. The developed theoretical picture was obtained in close collaboration with the experimentalists at the Max Planck Institute for the Structure and Dynamics of Matter (MPSD), who provided the reference experimental data and a spectroscopic model derived from the analysis of experimental observations. The investigated system for this study was the 9H- isomer of adenine, the most studied DNA nucleobase in the past. A minimal kinetic model was derived from the experimental results: excitation to a bright $\pi\pi^*$ state is followed by fast population transfer to a dark $n\pi^*$ state via a conical intersection. The deactivation of the $n\pi^*$ state population is due to a second conical intersection connecting the dark and the ground state.

The non-Markovian quantum dynamics of such system has been simulated by means of two methods: Time Nonlocal (TNL) [69], and Hierarchy Equations of Motion (HEOM) [77, 79] approach. 2DES and pump probe spectra have been simulated and compared with the available experimental data, leading in both cases to good agreement between the experiment and theory.

For the HEOM approach, the linear vibronic coupling model [124] has been used, while in the TNL treatment, no vibronic structure of the excited states was accounted for. Therefore, the HEOM approach leads to more accurate results, even though a good agreement for the pump-probe spectra at short delay times was not yet reached. However, the theoretical modelings presented here fully supports the spectroscopic model derived from experiments and the proposed route for deactivation of population in DNA nucleobases via two conical intersections [109].

Several issues still limit the performance of both TNL and HEOM approaches, for instance, the use of the Condon approximation and the high temperature limit. Further spectroscopic studies in terms of ultrafast 2D spectroscopy are necessary to confirm the results of the present study, which will serve as a basis for future simulations and experimental investigations.

The natural continuation of the research described in the present work is the extension of the model from single nucleobases to nucleotides (and nucleosides) polymers. Simulation of linear absorption, circular dichroism and 2DES spectra for dimers, and even longer chains of nucleobases will be the next steps of the research, with the goal of reproducing the experimental data, available for chains of 2, 4 and 10 DNA monomers.

The modeling of such systems clearly would imply taking into account the exciton couplings between the DNA monomers and charge transfer due to the interaction of more monomers within a single (or double) DNA strand, already studied and introduced in Chapter 1.

The present work is the first milestone towards the development of a working exciton model for single-stranded, and furthermore double-stranded DNA, so that we can gain a full understanding of the forthcoming 2D spectra.

A suitable system for a promising application of the semiclassical ensamble method is the cyclobutane thymine dimer, the major DNA lesion induced in human skin by sunlight, whose recognition and repair are intensively studied for the implication on human health [127]. Linear absorption and circular dichroism spectroscopies of such molecule are possible topics for future research.

Bibliography

[1] C. E. Crespo-Hernandez, B. Cohen, P.M. Hare, B. Kohler *Chem. Rev.*, 2004, **104**, 1977-2009.

[2] C.T. Middleton, K. de la Harpe, C. Su, Y.K. Law; C. E. Crespo-Hernandez, B. Kohler *Annu. Rev. Phys. Chem.*, 2009, **60**, 217-239.

[3] K. Kleinermanns, D. Nachtigallova, M.S. de Vries *Int. Rev. Phys. Chem.*, 2013, **32**, 308-342.

[4] W. C. Chung, Z. Lan, Y. Ohtsuki, N. Shimakura, W. Domcke, Y. Fujimura *Phys. Chem. Chem. Phys.*, 2007,**9**, 2075-2084.

[5] S. Matsika *J. Phys. Chem. A*, 2005, **109**, 7538-7545.

[6] M. Barbatti, A. J. Aquino, J. J. Szymczak, D. Nachtigallova, P. Hobza, H. Lischka *PNAS*, 2010, **107**, 21453-21458.

[7] C. E. Crespo-Hernandez, B. Kohler *J. Phys. Chem. B*, 2004, **108**, 11182–11188.

[8] F. Santoro, R. Improta, P. Segado, A. Lami *Photochem. Photobiol. Sci.*, 2013, **12(8)**, 1527-1543.

[9] M. Barbatti et al. *Phys. Chem. Chem. Phys.*, 2010, **12**, 4959-4967.

[10] A. Nenov, J. Segarra-Marti, A. Giussani, I. Conti, I. Rivalta, E. Dumont, V. K. Jaiswal, S. F. Altavilla, S. Mukamel, M. Garavelli *Faraday Discuss.*, 2015, **177**, 345-362.

[11] S. Mai, M. Richter, P. Marquetand, L. Gonzalez *Top. Curr. Chem.*, 2015, **355**, 99-154.

[12] S. Ulrich, T. Schultz, M. Z. Zgierski, A. Stolow *Phys. Chem. Chem. Phys.*, 2004, **6**, 2796-2801.

[13] S. Ullrich, T. Schultz, M.Z. Zgierski, A. Stolow *J. Am. Chem. Soc.*, 2004, **126**, 2262–2263.

[14] L. Serrano-Andres, M. Merchan, A. C. Borin *Proc. Natl. Acad. Sci. U.S.A.*, 2006, **103 (23)**, 8691-8696.

[15] E. Fabiano, W. Thiel *J. Phys. Chem. A*, 2008, **112(30)**, 6859-6863.

[16] J. R. Platt *Journal of Chemical Physics*, 1949, **17**, 484-495.

[17] A. F. Fucaloro, L. S. Forster, *J. A. Chem. Soc.*, 1971, **93**, 6443-6448.

[18] H. Kang, K. Lee, B. Jung, Y. Ko, S. K. Kim *J. Am. Chem. Soc.*, 2002, **124**, 12958-12959.

[19] H. Kang, B. Jung, S. K. Kim *J. Chem. Phys.*, 2003, **118**, 6717–6719.

[20] C. Canuel, M. Mons, F. Piuzzi, B. Tardivel, I. Dimicoli, M. Elhanine *J. Chem. Phys.*, 2005, **122**, 074316-1 - 074316-6.

[21] M. Barbatti, H. Lischka *J. Am. Chem. Soc.*, 2008, **130(21)**, 6831–6839.

[22] Y. Lei, S. Yuan, Y. Dou, Y. Wang, Z. Wen *J. Phys. Chem. A*, 2008, **112(37)**, 8497–8504.

[23] A. L. Sobolewski, W. Domcke *Eur. J. Phys. D*, 2002, **20**, 369-374.

[24] S. Perun, A. L. Sobolewski, W. Domcke *Chem. Phys.*, **313**, 107–112.

[25] H. R. Mahler, B. Kline and B. D. Mehrotra *J. Mol. Biol.*, 1964, **9**, 801-811.

[26] T. Takaya, C. Su, K. de La Harpe, C. E. Crespo-Hernandez, B. Kohler *Proc. Natl. Acad. Sci. USA*, 2008, **105**, 10285–10290.

[27] F. Plasser, A.J.A. Aquino, H. Lischka, D. Nachtigallova *Top. Curr. Chem.*, 2015, **356**, 1–38.

[28] A.J.W.G. Visser, O.J. Rolinski *BASIC PHOTOPHYSICS* Photobiological Science Online (photobiology.info).

[29] J. Von Neumann, E. P. Wigner *Z. Physik*, 1929, **30**, 465-467.

[30] F. Hund *Z. Physik*, 1927, **40**, 742-764.

[31] S.M.G. Faeder, D.M. Jonas *Journal of Physical Chemistry A*, 1999, **103(49)**, 10489–10505.

[32] J.D. Hybl, A.A. Ferro, D.M. Jonas *Journal of Chemical Physics*, 2001, **115(14)**, 6606–6622.

[33] M. Khalil, N. Demirdoven, A. Tokmakoff *Physical Review Letters*, 2003, **90**, 047401/1-047401/4.

[34] Shaul Mukamel. *Principles of Nonlinear Optical Spectroscopy*, Oxford University Press, 1995.

[35] W. Zhuang, T. Hayashi, and S. Mukamel *Angewandte Chemie-international Edition*, 2009, **48(21)**, 3750–3781.

[36] M. H. Cho. *Chemical Reviews*, 2008, **108(4)**, 1331–1418.

[37] J. Allen Myers *Two-Dimensional Electronic Spectroscopy of the Photosystem II D1D2-cyt.b559 Reaction Center*, University of Michigan, 2010.

[38] K. Lazonder, M. S. Pshenichnikov, D. A. Wiersma *Optics Letters*, 2006, **31(22)**, 3354–3356.

[39] J. P. Ogilvie *Advances In Atomic, Molecular, and Optical Physics*, 2009, **57**, 249–321.

[40] P. Pyykko, J. F. Stanton *Chem. Rev.* 2012, **112**, 1-3.

[41] W. Thiel *Angew. Chem. Int. Ed.*, 2011, **50**, 9216–9217.

[42] D. I. Lyakh, M. Musial, V. F. Lotrich, R. J. Bartlett *Chem. Rev.*, 2011, **112**,182-243.

[43] D. Cremer, J. A. Pople *J. A. Chem. Soc.*, 1975, **97**, 1354–1358.

[44] W. Thiel *New methods in computational quantum mechanics, Advances in chemical physics.*, 1996, **93**, 703-757.

[45] W. Thiel *WIREs Comput Mol Sci*, 2014, **4**, 145-157.

[46] A. J. Cohen, P. Mori-Sanchez, W. Yang *Chem Rev*, 2012, **112**, 289–320.

[47] F. Jensen, *Introduction to Computational Chemistry*, 2nd edition, John Willey and Sons Ltd.: New York, 2007.

[48] K. Burke *J. Chem. Phys.*, 2012, **136**, 150901-1 - 150901-9

[49] L. H. Thomas *Proc. Cambridge. Phil. Soc.* **23**, 542-548.

[50] P. Hohenberg, W. Kohn *Phys. Rev.* 1964, **136**, B864-B871.

[51] W. Kohn, J. Sham *Phys.Rev.*, 1965, **140**, A1133-A1138.

[52] Runge, E.; Gross, E. K. U. *Phys. Rev. Lett.* 52, 997–1000, 1984.

[53] K. Burke, E. K. U. Gross *A guided tour of time-dependent density functional theory in Density functional: Theory and applications*, Springer, Berlin, 1998.

[54] R. van Leeuwen *Phys. Rev. Lett.*, 1999, **82**, 3863–3866.

[55] F. Plasser, R. Crespo-Otero, M. Pederzoli, J. Pittner, H. Lischka, M. Barbatti *J. Chem. Theory Comput.*, 2014, **10**, 1395-1405.

[56] R. Crespo-Otero, M. Barbatti *Theor. Chem. Acc.*, 2012, **131(6)**, 1-14.

[57] M. Barbatti, A. J. A. Aquino, H. Lischka *Phys. Chem. Chem. Phys.*, 2010, **12 (19)**, 4959-4967.

[58] V. May, O. Kühn *Charge and Energy Transfer Dynamics in Molecular Systems, 3rd, Revised and Enlarged Edition*, Wiley, 2011.

[59] M. Barbatti, G. Granucci, M. Persico, M. Ruckenbauer, M. Vazdar, M. Eckert-Maksic, H. Lischka *J. Photochem. Photobio. A*, 2007, **190**, 228-240.

[60] M. Barbatti, M. Ruckenbauer, F. Plasser, J. Pittner, G. Granucci, M, Persico, H. Lischka *WIREs: Comp. Mol. Sci.*, 2014, **4**, 26-33.

[61] Gaussian 09, Revision E.02, M. J. Frisch, G. W. Trucks, H. B. Schlegel, G. E. Scuseria, M. A. Robb, J. R. Cheeseman, G. Scalmani, V. Barone, B. Mennucci, G. A. Petersson, H. Nakatsuji, M. Caricato, X. Li, H. P. Hratchian, A. F. Izmaylov, J. Bloino, G. Zheng, J. L. Sonnenberg, M. Hada, M. Ehara, K. Toyota, R. Fukuda, J. Hasegawa, M. Ishida, T. Nakajima, Y. Honda, O. Kitao, H. Nakai, T. Vreven, J. A. Montgomery, Jr., J. E. Peralta, F. Ogliaro, M. Bearpark, J. J. Heyd, E. Brothers, K. N. Kudin, V. N. Staroverov, R. Kobayashi, J. Normand, K. Raghavachari, A. Rendell, J. C. Burant, S. S. Iyengar, J. Tomasi, M. Cossi, N. Rega, J. M. Millam, M. Klene, J. E. Knox, J. B. Cross, V. Bakken, C. Adamo, J. Jaramillo, R. Gomperts, R. E. Stratmann, O. Yazyev, A. J. Austin, R. Cammi, C. Pomelli, J. W. Ochterski, R. L. Martin, K. Morokuma, V. G. Zakrzewski, G. A. Voth, P. Salvador, J. J. Dannenberg, S. Dapprich, A. D. Daniels, Ö. Farkas, J. B. Foresman, J. V. Ortiz, J. Cioslowski, and D. J. Fox, Gaussian, Inc., Wallingford CT, 2009.

[62] A.J.A. Aquino, D. Nachtigallova, P. Hobza, D. G. Truhlar, G.C. Hattig, H. Lischka *J. Comput. Chem.*, 2011, **32(7)**, 1217–1227.

[63] Y. Zaho, D. G. Truhlar *Theo. Chem. Account*, 2007, **120(1)**, 215–241.

[64] David S. Weiss, J. Robin Cowdery and Ralph H. Young *Electron Transfer in Chemistry*, Wiley, 2008.

[65] H-J. Briegel and B-G. Englert, *Phys. Rev. A*, 1993, **47**, 3311-3329.

[66] U. Kleinekathöfer *The Journal of Chemical Physics*, 2004, **121**, 2505-2514.

[67] R. Zwanzig *Lectures in Theoretical Physics*, 1961, Boulder, Colorado **3.30**, Interscience, New York.

[68] F. Haake, *Springer Tracts Mod. Phys.*, 1973, **66**, 98-168.

[69] C. Meier, D. j. Tannor, *The Journal of Chemical Physics*, 1999, **111**, 3365-3376.

[70] M. F. Gelin, D. Egorova, W. Domcke *J. Chem. Phys.*, 2005, **123**, 164112-1 - 164112-11.

[71] Y. Tanimura, R. Kubo *J. Phys. Soc. Jpn.*, 1989, **58**, 1850-1859.

[72] C. Kreisbeck, T. Kramer *J. Phys. Chem. Lett.*, 2012, **3(19)**, 2828–2833.

[73] A. G. Dijkstra, Y. Tanimura *New J. Phys.*, 2012, **14 (7)**, 073027-1 - 073027-11.

[74] M. Tanaka, Y. Tanimura *J. Phys. Soc. Jpn.*, 2009, **78**, 073802/1–073802/4.

[75] Y. Cheng, W. Hou, Y. Wang, Z. Li, J. Wei, and Y. Yan *New J. Phys.*, 2015, **17**, 033009-1 - 033009-11.

[76] J. S. Jin, X. Zheng, and Y. J. Yan, *J. Chem. Phys.*, 2008, **128**, 234703-1 - 234703-15.

[77] M. Tanaka and Y. Tanimura *J. Chem. Phys.*, 2010, **132**, 214502-1 - 214502-11.

[78] A. Garg, J. N. Onuchic, and V. Ambegaokar *J. Chem. Phys.*, 1985, **83**, 4491-4503.

[79] Y. Tanimura *J. Chem. Phys.*, 2012, **137**, 22A550-1 - 22A550-9.

[80] M. Pola, M. Kochman, A. Picchiotti, V. Prokhorenko, R. J. D. Miller, M. Thorwart *"Linear photoabsorption spectra and vertical excitation energies of microsolvated DNA nucleobases in aqueous solution"*, submitted to JCP.

[81] E. R. Bittner, *J. Chem. Phys.*, 2006, **125**, 094909-1 - 094909-12.

[82] R. P. Rastogi, Richa, A. Kumar, M. B. Tyagi and R. P. Sinha, *Journal of Nucleic Acids*, 2010, Article ID 592980.

[83] B. Marchetti, T. N. V. Karsili, M. N. R. Ashfold and W. Domcke *Phys. Chem. Chem. Phys.*, 2016, Advance Article, doi: 10.1039/C6CP00165C.

[84] A. C. Rios and Y. Tor *Astrobiology*, 2012, **12,** 884-891.

[85] A. C. Rios and Y. Tor *Isr. J. Chem.*, 2013, **53**, 469-483.

[86] Improta R., Barone V. *Top Curr. Chem.*, 2015, **57**, 355-329.

[87] A. W. Lange, M. A. Rohrdanz and J. M. Herbert *J. Phys. Chem. B*, 2008, **112**, 6304-6308.

[88] Lan T., Lu Y., Fabiano E., Thiel W. *Chem. Phys. Chem.*, 2011, Volume 12, Issue 10, 1989–1998.

[89] B. Heggen, Z. Lan, W. Thiel *Phys. Chem. Chem. Phys*, 2012, **14**, 8137-8146.

[90] D. Tuna, A. L. Sobolewski, W. Domcke *J. Phys. Chem. A*, 2014, **118**, 22.

[91] F. Plasser, H. Lischka *Photochem. Photobiol. Sci.*, 2013, **12**, 1440-1452.

[92] T. Lu, Z. Lan, W. Thiel *Top Curr. Chem.*, 2015, **356**, 89-122.

[93] M. Barbatti *J. Am. Chem. Soc.*, 2014, **136(29)**, 10246–10249.

[94] M. Barbatti, H. Lischka *Phys. Chem. Chem. Phys.*, 2015, **53(6-7)17(23)**, 15452-15459.

[95] S. Chaiwongwattana, M. Sapunar, A. Ponzi, P. Decleva, N Doslic *J. Phys. Chem. A.*, 2015, **119(43)**, 10637–10644.

[96] R. Szabla, J. Campos, J. E. Sponer, R. W. Gora, J. D. Sutherland *Chem. Sci.*, 2015, **6**, 2035-2043.

[97] R. Improta, F. Santoro, L. Blancafort, *Chem. Rev.*, 2016, **116,** 3540 - 3593.

[98] Y. Zhao and D. G. Truhlar, *Theor. Chem. Account*, 2008, **120**, 215-241.

[99] F. Plasser, R. Crespo-Otero, M. Pederzoli, J. Pittner, H. Lischka and M. Barbatti, *J. Chem. Theory Comput.*, 2014, **10**, 1395-1405.

[100] D. M. York, M. Karplus *J. Phys. Chem. A*, 1999, **103**, 11060-11079.

[101] G. Scalmani, M. J. Frisch *J. Chem. Phys.*, 2010, **132**, 114110-1 - 114110-15.

[102] B. Cohen, P. M. Hare, B. Kohler *J. Am. Chem. Soc.*, 2003, **125**, 13594-13601.

[103] L. J. Yu, R. Pang, S. Tao, H. T. Yang,D. Y. Wu, Z. Q. Tian *J. Phys. Chem. A*, 2013, **117**, 4286-4296.

[104] L. Serrano-Andres, M. Merchan, A. C. Borin *JACS*, 2008, **130**, 2473-2484.

[105] L. Serrano-Andres, M. Merchan, A. C. Borin *Chem. Eur. J.*, 2006, **12**, 6559-6571.

[106] P. G. Szalay, T. Watson, A. Perera, V. L. Lotrich, R. J. Bartlett *J. Phys. Chem. A*, 2012, **116**, 6702-6710.

[107] P. G. Szalay, T. Watson, A. Perera, V. Lotrich, G. Fogarasi, and R. J. Bartlett, *J. Phys. Chem. A*, 2012, **116**, 8851-8860.

[108] A. Tajti, G. Fogarasi, P.G. Szalay *Chem. Phys. Chem.*, 2009, **10**, 1603-1606.

[109] V. I. Prokhorenko, A. Picchiotti, and R.J. D. Miller *New insight into photophysics of DNA nucleobases*, 2016, submitted to UP2016.

[110] M. F. Gelin, D. Egorova, W. Domcke *J. Phys. Chem. Lett.*, 2010, **2**, 114–119.

[111] D. Polli, P. Alto'e, O. Weingart, K. M. Spilane, C. Manzoni, D. Brida, G. Tomasello, G. Orlandi, P. Kukura, R. A. Mathies, et al. *Nature*, 2010, **467**, 440–443.

[112] G. A. Worth, L. S. Cederbaum *Annu. Rev. Phys. Chem.*, 2004, **55**, 127-158.

[113] M. J. Bearpark, F. Bernardi, S. Clifford, M. Olivucci, M. A. Robb, B. R. Smith, V. T. *J. Am. Chem. Soc.*, 1996, **118**, 169-175.

[114] L. Joubert-Doriol, I. G. Ryabinkin, A. F. Izmaylov *J. Chem. Phys.* , 2013, **139**, 234103-1 - 234103-10.

[115] K. Dorfman, K. Bennett, M. Kowalewski, and S. Mukamel *Phys. Rev. Lett.*, 2015, **115**, 193003-1 - 193003-6.

[116] M. Kowalewski and S. Mukamel, *J. Chem. Phys.*, 2015, **143**, 044117-1 - 044117-9.

[117] R. Szabla, D. Tuna, R. W. Gora, J. Sponer, A. L. Sobolewski, and W. Domcke *J. Phys. Chem. Lett.*, 2013, **4**, 2785-2788.

[118] K. Saita, M. G. Nix, and D. V. Shalashilin *Phys. Chem. Chem. Phys.*, 2013, **15**, 16227-16235.

[119] J. Krmar, M. F. Gelin, D. Egorova, and W. Domcke *J. Phys. B: At. Mol. Opt. Phys.*, 2014, **47**, 124019-1 - 124019-9.

[120] A. Nenov, A. Giussani, J. Segarra-Marti, V. K. Jaiswal, I. Rivalta, G. Cerullo, S. Mukamel, and M. Garavelli, *J. Chem. Phys.*, 2015, **142**, 212443-1 - 212443-17.

[121] A. Nenov, J. Segarra-Marti, A. Giussani, I. Conti, I. Rivalta, E. Dumont, V. K. Jaiswal, S. Altavilla, and S. G. M. Mukamel, *Faraday Disc.* , 2015, **177**, 345-362.

[122] W. Domcke, D. R. Yarkony, and H. Koppel, *Conical Intersections: Theory, Computation and Experiment* World Scientific, 2011.

[123] M. I. Hassan, W. C. Chung, N. Shimakura, S. Koseki, H. Kono, and Y. Fujimura *Phys. Chem. Chem. Phys.*, 2010, **12**, 5317-5328.

[124] L. Seidner, W. Domcke *Chem. Phys.*, 1994, **186**, 27-40.

[125] A. Ishizaki and G. R. Fleming *Proc. Natl. Acad. Sci. USA* 2009, **106**, 17255.

[126] U. Leiter, C. Garbe *Advances in experimental medicine and biology*, Springer, New York, 2008, **624**, 89–103.

[127] J. T. Reardon, A. Sancar *Genes Dev*, 2003, **17(20)**, 2539–2551.

Acknowledgements

I would like to aknowledge my supervisor, Prof. Dr. Michael Thorwart, and my cosupervisor, Dr. Valentyn I. Prokhorenko, for their guidance during my Phd studies.
Special thanks to Dr. Michal Kochman and Dr. Arend Dijkstra for their constant help and support. The scientific collaboration with them was incredibly instructive and played a fundamental role in the realization of this project.

Erklärung

Die hier vorgelegte Dissertation habe ich eigenständig und ohne unerlaubte Hilfe angefertigt. Die Dissertation wurde in der vorgelegten oder in ähnlicher Form noch bei keiner anderen Institution eingereicht. Ich habe bisher keine erfolglosen Promotionversuche unternommen.

_____

Martina Pola

Hamburg, den 14.07.2016